2021

Unraveling the Interaction Between Beige Adipocytes and the Sympathetic Nervous System

Jingyi Chi

UNRAVELING THE INTERACTION BETWEEN BEIGE ADIPOCYTES AND THE SYMPATHETIC NERVOUS SYSTEM

A Thesis Presented to the Faculty of
The Rockefeller University
in Partial Fulfillment of the Requirements for
the degree of Doctor of Philosophy

by
Jingyi Chi
June 2021

UNRAVELING THE INTERACTION BETWEEN BEIGE ADIPOCYTES AND THE SYMPATHETIC NERVOUS SYSTEM

Jingyi Chi, Ph.D.
The Rockefeller University 2021

Obesity affects more than one in three adults in the United States and is a significant risk factor for a constellation of chronic diseases. The crucial role of adipose tissue in energy balance has driven great interest in investigating this tissue as a target for treatment of obesity and its sequelae. While white adipocytes store excess energy, thermogenic brown and beige adipocytes convert lipids and glucose into heat, thereby increasing energy expenditure. Unlike classical brown adipocytes which are thermogenic under basal conditions, inducible brown adipocytes, commonly known as beige adipocytes, reside in white adipose depots and need to be activated by external stimuli such as the sympathetic nervous system to drive thermogenesis. Recent studies have shown that active beige adipocytes can increase energy expenditure and are associated with anti-obesity and anti-diabetes effects in mice and humans. However, the origin of beige adipocytes and how they interact with other adipose cell types remains unclear, creating critical hurdles to manipulating these cells for therapeutic ends.

To seek a comprehensive understanding of beige adipocyte formation, we developed a novel technique that enables whole-tissue immunostaining, clearing, and imaging in adipose tissue. Using this new method, we profiled various murine white adipose depots and observed pronounced depot to depot variability in tissue organization. Analysis of cold-induced beige adipocyte formation in whole adipose depots uncovered prominent regional variation in beige adipocyte distribution in subcutaneous fat. Through morphological characterization of the sympathetic nerve projections in subcutaneous fat, we found a dense network of sympathetic parenchymal neurites localizing to the same region where beige adipocytes readily arise.

To understand how the dense sympathetic network is established, we used an adipocyte-specific *Prdm16* knockout mouse model to ablate beige adipocyte function and demonstrated that the density of sympathetic parenchymal innervation depends on the presence of functional beige adipocytes. These results suggest that communication between beige adipocytes and the sympathetic neurites is important for the establishment of sympathetic innervation. To address whether the regulation by beige adipocytes occurs during early tissue morphogenesis, we applied whole-tissue imaging to examine the development of sympathetic innervation in subcutaneous fat. We found that parenchymal neurites actively grow between postnatal day 6 (P6) and P28, overlapping with early postnatal beige adipogenesis. Constitutive deletion of *Prdm16* in adipocytes led to a significant reduction in early postnatal beige adipocytes and sympathetic density within this window. Using an inducible, adipocyte-specific *Prdm16* knockout model, we ablated the function of early postnatal beige adipocytes and found strongly impaired sympathetic growth. These data suggest that sympathetic growth in subcutaneous fat depend on a PRDM16-mediated mechanism. However, deleting *Prdm16* in adult animals, did not affect sympathetic structure. Together, these findings highlight that beige adipocyte-sympathetic neurite communication is crucial to establish sympathetic structure during the early postnatal period, but may be dispensable for its maintenance in mature animals. These studies unravel the complex

interaction between beige adipocytes and the sympathetic nervous system, providing a framework for further investigation of the molecular mechanisms underlying this interaction.

Lastly, investigation of the early postnatal beige adipocytes allowed us to appreciate an unprecedented link between early postnatal and adult beige adipocytes. By fate mapping beige adipocytes through development, we found that the majority of cold-induced beige adipocytes in adult subcutaneous fat arise from existing mature adipocytes that were once early postnatal beige adipocytes. These studies provide fundamental insights into beige adipocyte formation and will guide future investigation of the origin and fate of beige adipocytes.

For the benefit of humanity

ACKNOWLEDGMENTS

First and foremost, thank you to Dr. Paul Cohen for being an incredible mentor. I was extremely fortunate to be among the first lab members to join the lab and to witness the growth of the Cohen lab from the very beginning. Thank you for entrusting me with the tissue clearing project and encouraging me to explore my interests and follow "wherever nature leads us". Paul's expertise in both basic research and medicine has cultivated my appreciation for both basic and translational research. Thank you for training me to be a scientist with passion, vision, and responsibility. My PhD has been quite an adventure for me. Thank you for your kind encouragement along the way. Thank you for creating a lab environment where everyone cares for each other and the lab. Thank you for your great taste in food. I truly enjoyed our wonderful lab barbeques and holiday dinners. I am extremely grateful for Paul's extraordinary mentorship. I look forward to seeing exciting work unfold in the lab in the near future.

Thank you to Drs. Jeffery Friedman and Sanford Simon for serving on my faculty advisory committee. Your insightful questions and feedback have shaped my scientific thinking. During our FAC meetings over the years, I was encouraged to think outside the box while rigorously testing every step. I am grateful for having your guidance. Thank you to Dr. Peter Tontonoz for serving as my external examiner. Your expertise in adipose biology provided invaluable input for my thesis.

I would like to give special thanks to Dr. Zhuhao Wu, who showed me the magic behind tissue clearing, for being a wonderful collaborator and mentor. Your expertise in axon guidance has also been invaluable. Our collaboration was truly instrumental to my project.

I would next like to thank all members of the Cohen lab. Thank you all for your help and guidance on experiments, insightful brainstorming during lab meetings, and incredible fun you brought into my life. Thank you to Lily Nguyen, our lab's founding member and my first bay mate, for helping me with my initial experiments and cheering for my journey through PhD. Thank you to Sarah Ackerman, my fellow Potterhead, for her impressive Harry Potter trivia knowledge and mouse injection skills. Thank you to Sean O'Connor, for bringing me into Star Wars. Thank you to Olivia Maguire and Kaja Plucinska, for being our lab's social chair and insisting we should also have fun outside science. Thank you to Aarthi Maganti, for being a good friend from the beginning. Thank you to Francois Marchildon, our in-house exercise expert, for your constant reminder that 150 min of exercise per week is good for health. Thank you to Chan Hee Choi for patiently teaching me the beauty of impeccable protein work. Thank you to Tobias Becher, for educating me about the importance of human brown fat. Your amazing work on human brown fat is what motivates my everyday experiments. Thank you to Sarah Szwed, for being the kindest person I have ever met. I cannot wait to see where you take the sympathetic nerves next. Thank you to Rico Lin, for being the perfect partner for many of the experiments and for sharing my passion for unraveling complex cell-cell interactions and beige adipocyte origin. Thank you to William Barr, Audrey Crane, and Saba Tegegne, for your help with my experiments. It was a great pleasure working with you. Thank you to Xiaojing Huang and Mascha Koenen, our newest members in the lab, for your insightful feedback during my lab meetings and thesis preparation. I look forward to seeing exciting work from you.

The Resource Centers at The Rockefeller University have provided crucial help for my experiments. In particular, I spent endless hours in the Bio-imaging Resource Center. Thank you to Alison North, Christina Pyrgaki, Tao Tong, Katarzyna Cialowicz, Carlos Rico, Kaye Thomas, and Pablo Ariel for your patient training and kind help. Thank you for bringing me into the microscopic world that is full of wonder. Thank you to Connie Zhao, Bin Zhang, and Hong Duan from the Genomics Resource Center for their help and guidance in designing and running our bulk and single-cell RNA sequencing experiments. Thank you to Thomas Carroll, Ji-Dung Luo, and Wei Wang from the Bioinformatics Resource Center for working with us to analyze our monstrous single-cell RNA sequencing data. Thank you to Svetlana Mazel and all members of the Flow Cytometry Resource Center for their crucial help for our sorting experiments. Thank you to all members from the Comparative Bioscience Center for caring for our animals.

I feel extremely grateful for completing my PhD in the David Rockefeller Graduate Program in Bioscience at The Rockefeller University. Thank you to members of the Dean's office, including Sidney Strickland, Emily Harms, Kristen Cullen, Cristian Rosario, Marta Delgado, Andrea Morris, and Stephanie Fernandez who have ensured that all students are well cared for and we can freely explore the best science possible. I am also grateful for all other members at Rockefeller for creating a welcoming community.

I thank all my family and friends who have been supporting me throughout my PhD. My dad has been an exceptional role model. My mom's curiosity and passion has kindled my journey in science. Thank you to my parents for your unconditional love and support. Thank you to my extended family for always thinking of me and bringing me joy. Thank you to Hongda and Julie, my early mentors and great friends, for your guidance and encouragement. Thank you to Timmy and Josh for visiting me in NYC over the years. Lastly, I would like to give special thanks to Xiphias Ge Zhu, my comrade in science and partner in life, who has always kept me accompany during the ups and downs throughout my PhD. Thank you for sharing my enthusiasm in science and life. Thank you for believing in me and keeping me honest with myself. I am excited to see how our future unfolds in Boston.

TABLE OF CONTENTS

LIST OF FIGURES

LIST OF TABLES

LIST OF ABBREVIATIONS

2D	Two dimension
3D	Three dimension
APC	Adipocyte progenitor cell
BAT	Brown adipose tissue
c*Prdm16*^{KO} (or cKO)	Constitutive *Prdm16* knockout
DBE	Di-benzyl ether
DCM	Dichloromethane
Dox	Doxycycline
eWAT	Epididymal white adipose tissue
GFP	Green fluorescent protein
iBAT	Interscapular brown adipose tissue
i*Prdm16*^{KO} (or iKO)	Inducible *Prdm16* knockout
iWAT	Inguinal subcutaneous white adipose tissue
LN	Lymph node
LYVE1	Lymphatic vessel endothelial hyaluronan receptor 1
MIP	Maximum intensity projection
PRDM16	PR domain containing 16
RT	Room temperature
TH	Tyrosine hydroxylase
TRE	Tet response element
UCP1	Uncoupling protein 1
WAT	White adipose tissue

CHAPTER 1. INTRODUCTION

1.1 Obesity as a global health problem

There has been a progressive increase in the global rate of obesity over the past two decades. Obesity now affects over 40% of adults in the United States and over 600 million adults worldwide (CDC, 2020a; Collaborators, 2017). Obesity is characterized by excessive accumulation of body fat, which is the result of a chronic imbalance between energy intake and expenditure (Hill James O. et al., 2012). Excess adiposity contributes to a constellation of chronic diseases, including type 2 diabetes, hypertension, cardiovascular disease, and many types of cancer (Kopelman, 2000). Obesity-related medical care costs the United States health care system nearly $150 billion each year (CDC, 2020b). Addressing this public health emergency will require therapeutic approaches based on a deeper understanding of the tissues and pathways involved in energy homeostasis.

1.2 White, brown and beige adipocytes

Until recently, the role of adipose tissue in the development of obesity and its consequences was considered to be a passive one. Fat cells or adipocytes were thought to be little more than storage cells for lipids. We now know, however, that adipose tissue is a complex organ that plays a central role in mammalian energy homeostasis and thermoregulation, enabling adaptation to challenges such as limited or excess nutrients and cold temperatures (Rosen and Spiegelman, 2014). The crucial role of adipose tissue in energy balance has driven great interest in investigating this tissue as a target for the treatment of obesity.

Mammals have two well-characterized types of adipose tissue (**Figure 1.1**). White adipose tissue (WAT), composed mainly of white adipocytes with one large lipid droplet (unilocular morphology), stores excess energy in the form of triacylglycerol, which can then be mobilized when food is scarce (**Figure 1.1, white adipocytes**). Brown adipose tissue (BAT), by contrast, consists of brown adipocytes that contain several small lipid droplets and a high number of mitochondria (multilocular morphology). BAT dissipates energy as heat and therefore contributes to body temperature maintenance (**Figure 1.1, brown adipocytes**). This thermogenic function of BAT largely relies on a thermogenic adipocyte-specific program that uncouples the proton gradient generated by the electron transport chain from ATP synthesis, via the action of mitochondrial uncoupling protein 1 (UCP1). This thermogenic adipocyte specific program enables these cells to convert chemical energy into heat (Rosen and Spiegelman, 2014).

Besides classical brown adipocytes, which reside in brown fat depots, mammals also have inducible brown adipocytes, known as brite or beige adipocytes, which emerge in clusters within white fat depots. Similar to classical brown adipocytes, beige adipocytes are defined by their multilocular morphology, high mitochondrial content, and thermogenic capacity. However, these cells come from a distinct developmental lineage than brown adipocytes. Moreover, unlike classical brown adipocytes that are thermogenic under basal conditions, beige adipocytes express UCP1 and other thermogenic genes only in response to external stimuli such as cold, β-adrenergic agonists, thiazolidinediones, and certain hormones (**Figure 1.1, beige adipocytes**) (Rosen and Spiegelman, 2014; Wang and Seale, 2016).

White adipocytes

Brown adipocytes

Beige adipocytes
or
Inducible brown adipocytes

Location	White fat depots	Brown fat depots	White fat depots
Cellular morphology	Unilocular Low number of mitochondria	Multilocular High number of mitochondria	Multilocular High number of mitochondria
Function	Energy storage and mobilization	Thermogenesis	Thermogenesis upon induction

Figure 1.1 White, brown, and beige adipocytes.
A summary of location, morphology, and function of the three types of adipocytes in mammals.

1.3 Physiological importance of thermogenic adipocytes

Thermogenic brown and beige adipocytes in humans and mice are associated with metabolic benefits. Human brown fat is abundant in infants to help maintain body temperature. Until recently, brown fat was thought to disappear after infancy (Gilsanz et al., 2013). A decade ago, a series of seminal studies described the presence of metabolically active thermogenic fat in adult humans through positron-emission tomography (PET) imaging (Cypess et al., 2009; van Marken Lichtenbelt et al., 2009; Virtanen et al., 2009). Activation of human brown fat has been shown to be associated with increased energy expenditure, as well as improved glucose homeostasis, insulin sensitivity, and cardiometabolic health (Becher et al., 2021; Lee et al., 2014; Yoneshiro et al., 2011). Moreover, the activity of human brown fat is highly inducible by cold (Orava et al., 2011; Yoneshiro et al., 2011). These findings have driven great interest in developing approaches to enhance human brown fat function to combat obesity and associated metabolic diseases.

Interestingly, gene expression analyses of adult human brown fat identified a molecular signature that resembles murine beige adipocytes (Jespersen et al., 2013; Sharp et al., 2012; Shinoda et al., 2015). Indeed, genetic studies in mice have shown that activation of beige adipocytes provides potent metabolic benefits (Seale et al., 2011), while ablation of beige adipocyte function made mice more susceptible to obesity and associated metabolic problems (Cohen et al., 2014). A better understanding of mouse beige adipocytes could provide guidance to the development of more effective and targeted approaches to enhance human brown fat function.

1.4 Transcriptional control of beige adipocytes by PRDM16

Advances have been made in understanding the transcriptional control of mouse beige adipocytes. Beige adipocyte determination and function depend on a transcriptional coregulatory protein PRDM16 (PR domain containing 16). Transgenic mice overexpressing PRDM16 in all fat cells exhibited strong beige adipocyte biogenesis in their white fat depots, particularly in the inguinal

subcutaneous white fat (iWAT) (Seale et al., 2011). On the other hand, adipocyte-specific deletion of PRDM16 ablated beige adipocyte formation in iWAT following cold or β-adrenergic stimulation (Cohen et al., 2014).

PRDM16 acts bifunctionally to promote expression of thermogenic adipocyte-selective genes and suppress white adipocyte-selective genes in the same cell through protein-protein interactions (Chi and Cohen, 2016). For example, C/EBPβ, PPARγ, and PGC1α, which are important transcription regulators for adipocyte differentiation and mitochondrial biogenesis, have been shown to be associated with PRDM16 to promote the thermogenic adipocyte-selective gene program (**Figure 1.2 A**) (Seale et al., 2007, 2008). Moreover, PRDM16 facilitates the recruitment of MED1/Mediator complex to the enhancer regions of certain thermogenic genes, resulting in a bridge between the enhancer and the promoter region, which then facilitates the assembly of the pre-initiation complex and promoting gene expression (**Figure 1.2 A**) (Harms et al., 2015; Iida et al., 2015). On the other hand, PRDM16 suppresses muscle- and white adipocyte-selective gene expression through recruiting repressive transcriptional complexes, such as EHMT1 and CtBP1/2 (**Figure 1.2 B-C**) (Kajimura et al., 2008; Ohno et al., 2013).

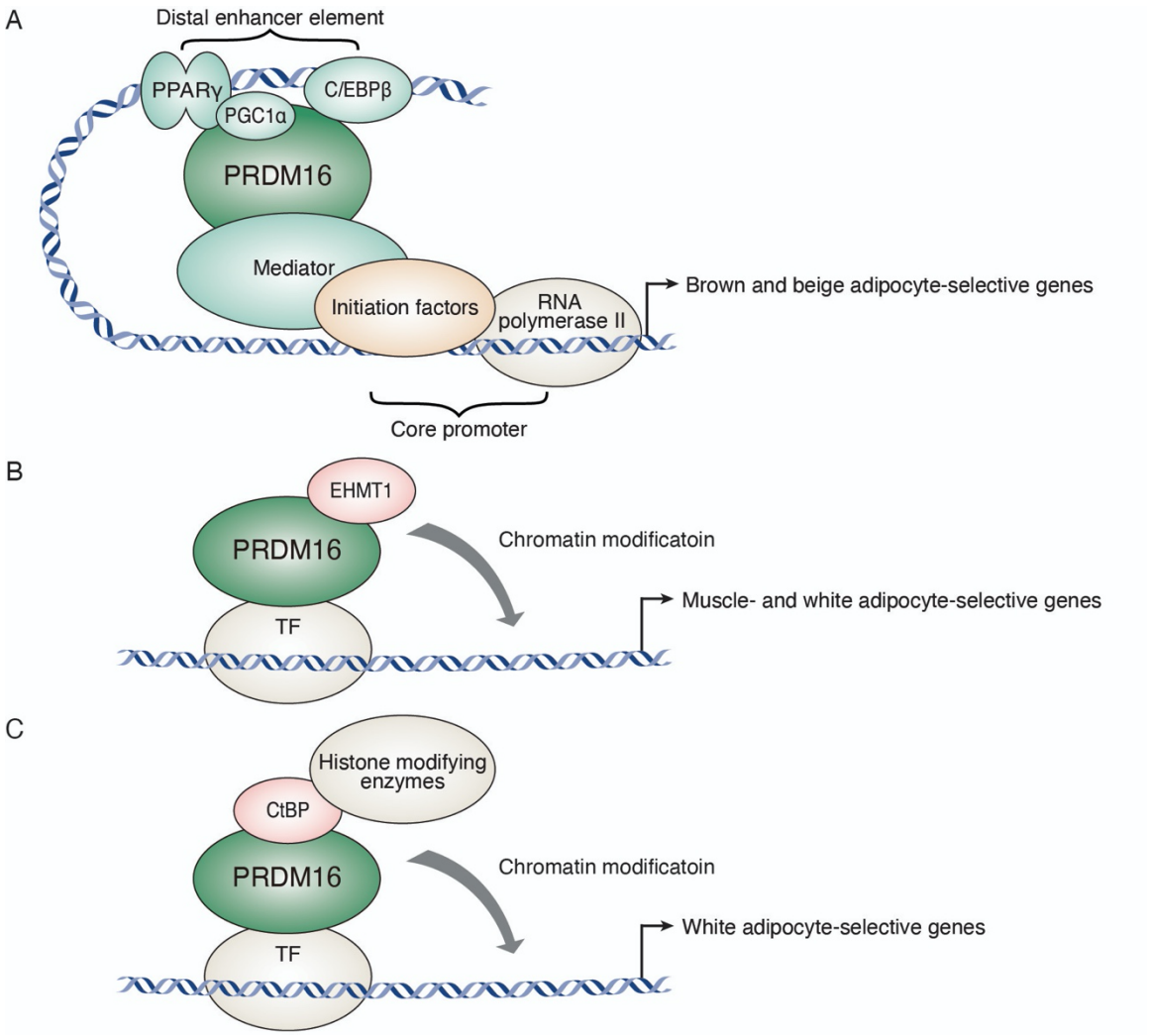

Figure 1.2 Mechanism of action of PRDM16 in thermogenic adipocytes.
(**A**) PRDM16 interacts with C/EBPβ, PPARγ, PGC1α, and MED1 to drive thermogenic adipocyte-selective gene expression. (**B-C**) PRDM16 interacts with (**B**) EHMT1 and (**C**) CtBP to repress muscle- and white adipocyte-selective genes.

1.5 Origin of beige adipocytes

The origin of thermogenic beige adipocytes that emerge in white fat depots following external stimulation has been highly debated. Beige adipocytes have been reported to arise from 1) conversion of existing mature white adipocytes and 2) *de novo* differentiation of adipocyte progenitor cells (**Figure 1.3**). Assisted by electron microscopy, studies reported that cold-induced beige adipocytes contain mitochondria that present an intermediate morphology in between classic brown and white adipocyte mitochondria, and therefore proposed that beige adipocytes arise from direct conversion of white adipocytes (Barbatelli et al., 2010). On the other hand, beige adipocytes have also been found to derive from progenitor cells with a unique molecular profile (Berry et al., 2016; Long et al., 2014; Wang et al., 2013; Wu et al., 2012), suggesting beige adipocytes are a distinct cell type from brown and white adipocytes.

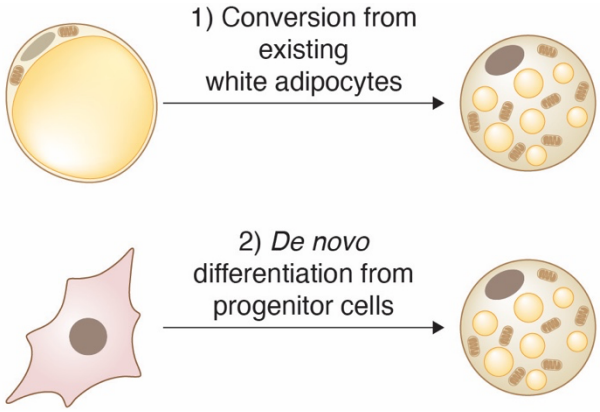

Figure 1.3 Schematic illustration of the possible origins of beige adipocytes.

To address the possible origins of beige adipocyte formation, fate mapping studies using inducible *Adipoq*-promoter-based reporter systems were widely employed. *Adipoq* (also known as adiponectin) is selectively and highly expressed in all mature adipocytes, including brown, beige, and white adipocytes (Scherer et al., 1995). Several studies performed labeling of all existing mature adipocytes with a reporter prior to cold stimulation and then analyzed the contribution of existing mature white adipocytes and newly differentiated adipocytes to beige adipocyte formation (Lee et al., 2015; Shao et al., 2019; Wang et al., 2013). Interestingly, while one study reported that all cold-induced UCP1+ beige adipocytes came from previously labeled mature white adipocytes (Lee et al., 2015), another study observed a significant proportion of UCP1+ beige adipocytes arising from newly born adipocytes (Wang et al., 2013). A more recent study reported that both sources significantly contribute to cold-induced beige adipocytes but the percentage from each source shifts based on the ambient temperature (Shao et al., 2019). Nevertheless, the conundrum remains as to why a unique cell type with distinct progenitor cells could also arise from phenotypic conversion of white adipocytes. Further investigation of the origin and fate of beige adipocytes is required to address this knowledge gap.

1.6 Sympathetic activation of beige adipocytes

Cold activation of thermogenic adipocytes has been shown to be mediated by the sympathetic nervous system. The sympathetic nervous system consists of two populations of neurons that are synaptically connected to relay efferent signals from the central nervous system to target tissues. The preganglionic neurons, whose cell bodies lie in the thoracic and upper lumbar segments of the spinal cord, extend axons to paravertebral (in the sympathetic chains) or prevertebral sympathetic ganglia. Within the sympathetic ganglia, axons that arise from the preganglionic neurons typically form chemical synapses with dendrites or cell bodies of the postganglionic neurons to control their activity. Finally, the postganglionic neurons send axons to innervate target organs to regulate tissue function (Karemaker, 2017).

Upon cold stimulation, the postganglionic sympathetic axons in fat release norepinephrine, which acts through β-adrenergic receptors on adipocytes to drive thermogenesis and lipolysis (Wang and Seale, 2016). Denervation of postganglionic sympathetic projections to iWAT greatly reduced beige adipocyte formation following cold exposure (Jiang et al., 2017a; Zhu et al., 2016).

Moreover, mice with genetic ablation of all three β-adrenergic receptors exhibited a similar defect in cold-induced beige adipocyte recruitment (Bachman et al., 2002; Barbatelli et al., 2010; Ye et al., 2013). On the other hand, the pharmacologic β3-adrenergic agonist, CL316,243, can potently induce the emergence of beige adipocytes in iWAT (Barbatelli et al., 2010; Cohen et al., 2014; Collins et al., 1997). These independent lines of evidence have demonstrated a crucial role of the sympathetic nervous system in cold-induced beige adipocyte formation.

Despite the unequivocal physiological importance, little is known about how the sympathetic neurites are organized in iWAT and how they interact with adipocytes *in vivo* to induce beige adipocyte formation. Although the existence of sympathetic neurites in adipose tissue has been recognized for decades, structural interactions between sympathetic nerves and adipocytes remain unclear. Traditionally, visualization of adipose sympathetic nerves relied heavily on immunostaining of paraffin-embedded tissue sections with antibodies targeting tyrosine hydroxylase (TH), the rate limiting enzyme of catecholamine synthesis and a common marker of sympathetic noradrenergic nerves (Molinoff and Axelrod, 1971). Examination of thin tissue sections confirmed the existence of TH-positive nerve fibers in close proximity to adipocytes (Murano et al., 2009). However, tissue sections are often imaged by high-magnification two-dimensional (2D) microscopy. Because 2D imaging can only capture cross-sectional views of the tissue, parenchymal nerve fibers are usually truncated in 2D images and appear as "puncta" or "small fragments", instead of continuous nerve fibers, preventing adequate quantification of nerve density and close examination of nerve-adipocyte interactions. Furthermore, imaging with high magnification only allows visualization of small fields of the tissue, which may not be representative of the whole tissue.

1.7 Challenges in studying cell-cell interactions in adipose tissue

In addition to adipocytes and sympathetic innervation, adipose tissue contains adipocyte progenitors, stromal cells, immune cells, and blood vessels, which have been shown to play important roles in regulating adipose tissue function (Rosen and Spiegelman, 2014). For example, several immune cell populations, such as type 2 innate lymphoid cells and eosinophils, as well as cells from the vasculature have been implicated in beige adipocyte recruitment (Brestoff et al., 2014; Qiu et al., 2014; Sun et al., 2012). We have only a rudimentary understanding of how these cell types are organized at the tissue level and how they interact with adipocytes or other cell types to promote the formation of beige adipocytes. Our current knowledge of adipose tissue organization and cell-cell interactions is largely limited by the imaging approaches applicable to adipose tissue. While other tissue systems can resort to imaging thick sections or whole-mount samples to capture the intricacies of cell-cell interactions in three dimensions (3D), the high lipid content in adipose tissue creates challenges in obtaining high-quality thick sections and produces significant light scatter that prevents high-resolution imaging into deep tissue. Hence, there is great need for an imaging approach that can provide 3D visualization of an entire adipose depot while still achieving cellular resolution.

1.8 Summary of undertaken studies

Most of our understanding of beige adipocytes and their interactions with other adipose tissue components comes from molecular studies and 2D histology. While these studies have provided

an abundance of knowledge, how beige adipocytes arise and how different cell types in adipose tissue interact *in vivo* to coordinately regulate beige adipocyte formation remain largely unclear. To seek a comprehensive understanding of these questions, we developed a novel technique that enables whole-tissue immunostaining, clearing, and imaging in adipose tissue. Assisted by whole-tissue 3D images, we explore cold-induced beige adipocyte formation in various white fat depots. Through morphological characterization of the sympathetic network in various genetic mouse models, we investigate complex interactions between beige adipocytes and the sympathetic nervous system. By tracking beige adipocytes across time and in whole tissue, we explore the origin of beige adipocytes with a holistic view. These studies unravel the complex interaction between beige adipocytes and the sympathetic nervous system and provide fundamental insights into beige adipocyte biogenesis.

CHAPTER 2. Characterizing adipose tissue structures by whole-tissue imaging.

2.1 Introduction

Until recently, adipose tissue was conceived of as an amorphous collection of fat cells. Over the past few decades, however, our understanding has grown more sophisticated, with fat now recognized to be a complex organ containing different types of adipocytes, as well as adipocyte precursors, immune cells, fibroblasts, the vasculature, and nerve projections. Interactions among these adipose-resident cells have pronounced effects on adipose tissue and organismal physiology and pathophysiology (Rosen and Spiegelman, 2014). Although emerging studies have unraveled important molecular mechanisms underlying certain interactions, a more comprehensive understanding requires reliable structural profiling of the entire tissue in three dimensions.

Our current knowledge of adipose tissue morphology is largely based on histological analysis of thin sections (5 μm) with relatively high magnification imaging (more than 10X) (Barbatelli et al., 2010; Wang et al., 2013). However, this approach has several significant limitations. First, intricate filamentous structures such as sympathetic nerves and the vasculature, which are known to play important roles in adipose function, are difficult to evaluate through thin sections (Bartness et al., 2014; Morrison et al., 2014; Shimizu et al., 2014; Xue et al., 2009). Second, due to its seemingly amorphous shape and the lack of representative structural units to focus on, it is difficult to appreciate adipose tissue structures based only on section staining. Third, adipose tissue has very high lipid content, creating challenges in obtaining consistent serial sections that are suitable for 3D anatomical reconstruction, a conventional method used to study whole brain morphology for example (Abe et al., 2017). Given these factors, there is a great need for a whole-mount approach that can provide 3D visualization of an entire adipose depot while still achieving cellular resolution.

3D volumetric imaging of an entire organ is challenging due to the obscuring effects of light scatter. A major source of light scatter in biological tissues comes from lipid-aqueous interfaces. Although efforts to eliminate scatter by removing lipids have been ongoing for over a century, there have been a large number of recent innovations (Richardson and Lichtman, 2015). One such newly developed tissue-clearing method is immunolabeling-enabled 3D imaging of solvent-cleared organs (iDISCO/iDISCO+) (Renier et al., 2014, 2016). However, adipose tissue presents a particular challenge given its high level of lipids, and therefore, additional modifications to the iDISCO/iDISCO+ protocol are required to fully extract lipids while protecting the tissue from collapsing. The modified protocol we have developed, now called Adipo-Clear, employs methanol/dichloromethane-based delipidation of adipose tissue to achieve optimal transparency suitable for high-resolution volumetric imaging (Chi et al., 2018b, 2018a).

2.2 Developing a whole-adipose immunostaining and clearing technique: Adipo-Clear

We developed an adipose tissue clearing technique that allows whole-tissue imaging to obtain an integrated view of the relationship between distinct cell types in adipose tissue in the basal state and following physiological challenges (**Figure 2.1 A**). We adapted the iDISCO/iDISCO+ method, which was developed for clearing tissues such as the brain (Renier et al., 2014, 2016). Adipose tissue stores a significant amount of lipid that produces severe light scattering, preventing the acquisition of sharp images from deep tissue by fluorescence microscopy. The existing

iDISCO/iDISCO+ protocol required modifications of the delipidation step to fully clear the substantial lipid, while maintaining tissue integrity (**Figure 2.1 B-C**). Delipidated fat pads were used for whole mount immunolabeling, followed by optical clearing. This clearing approach, which we refer to as Adipo-Clear, can be coupled with light sheet fluorescence microscopy to simultaneously image up to three different molecular markers in a whole tissue (See **Chapter 5.1 and 5.2** for detailed methods).

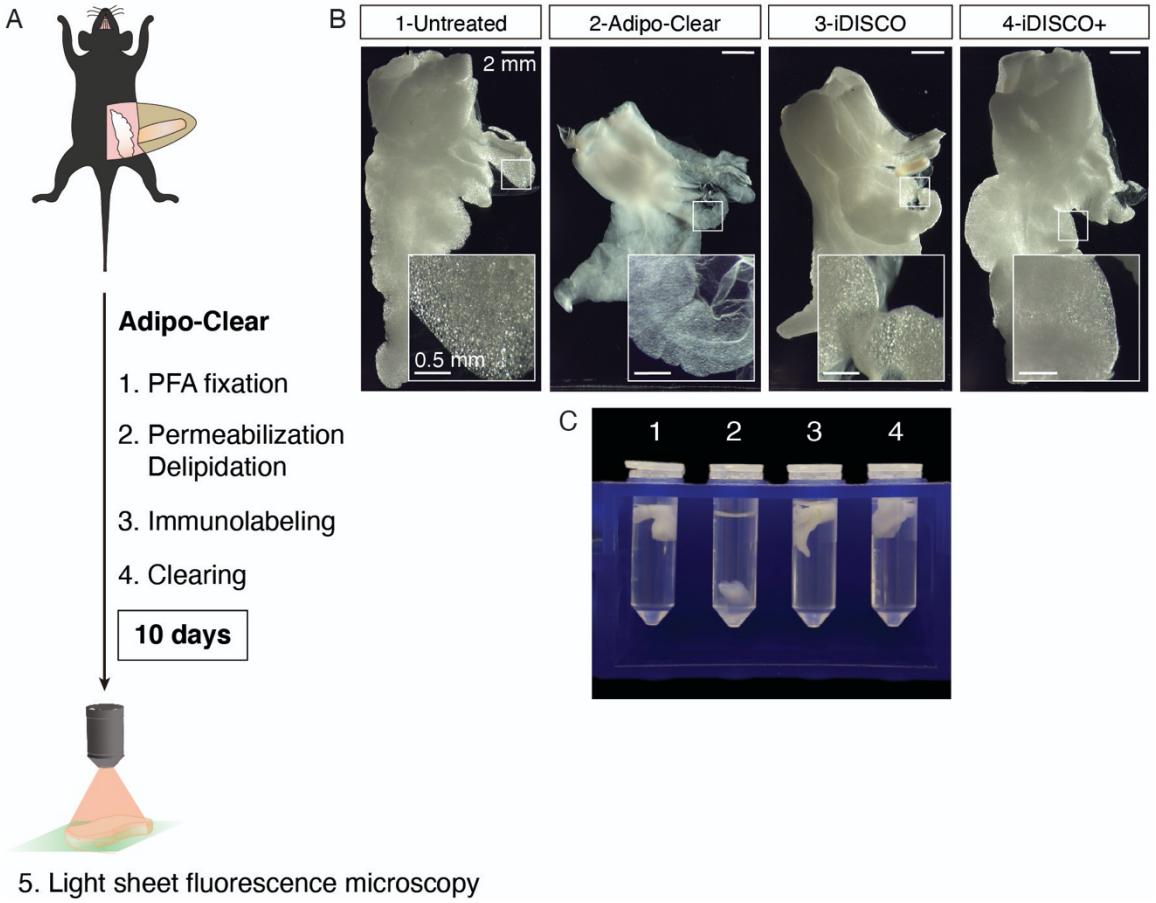

Figure 2.1 Adipo-Clear method optimization.
(**A**) Overview of the Adipo-Clear method. (**B**) Representative images of epididymal white fat (eWAT) to illustrate lipid levels. (1) Untreated, (2) delipidated with Adipo-Clear, (3) delipidated with iDISCO, and (4) delipidated with iDISCO+. Adipocytes containing lipid glitter under camera. Insets show higher-magnification images of the boxed regions within each sample. (**C**) The same samples as in **B** immersed in PBS. Samples containing high levels of lipid float in PBS. Scale bars are indicated.

Additionally, we found that the autofluorescence signal in the 488 (green) channel from cleared adipose samples delineates fat cell contour and overall tissue architecture. Autofluorescence images compare favorably with staining of perilipin, a protein associated with the surface of lipid droplets, in outlining fat cells (**Figure 2.2 A-C**). When compared to H&E-stained paraffin-embedded sections (**Figure 2.2 D**), tissues processed with Adipo-Clear demonstrated similar fat cell morphology, indicating minimal tissue distortion. In the following studies, we employed the autofluorescence signal to visualize individual adipocytes and tissue architecture.

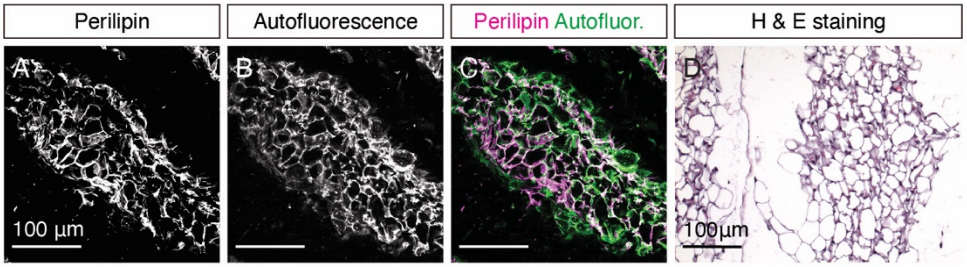

Figure 2.2 Tissue autofluorescence signal outlines individual fat cell contours.
(**A-C**) Confocal images of perilipin and tissue autofluorescence of a representative lobule from WT iWAT. (**A**) Perilipin. (**B**) Autofluorescence. (**C**) Perilipin (magenta) and autofluorescence (green) overlay. (**D**) Representative image from hematoxylin and eosin (H&E) stained section of iWAT. Scale bars are indicated.

2.3 Analysis of tissue architecture of murine white fat with whole-tissue imaging

It was once believed that all white adipose depots were equivalent, with phenotypic differences due to the anatomical locations of fat depots. More recent studies, however, have identified distinct developmental and molecular characteristics of subcutaneous and visceral adipose tissues (Gesta et al., 2006). Tissue autofluorescence images obtained from inguinal subcutaneous white fat (iWAT) and epididymal white fat (eWAT, male perigonadal visceral fat) processed by Adipo-Clear highlighted obvious differences in tissue architecture. iWAT was organized into discrete lobules (**Figure 2.3 A-A1**), suggesting a repetitive structural unit, whereas visceral fat had a relatively amorphous structure (**Figure 2.3 B-B1**). We have further explored how other tissue components such as nerve fibers are organized in such distinct tissue architecture. These findings could contribute to a better understanding of the phenotypic differences between subcutaneous and visceral fat.

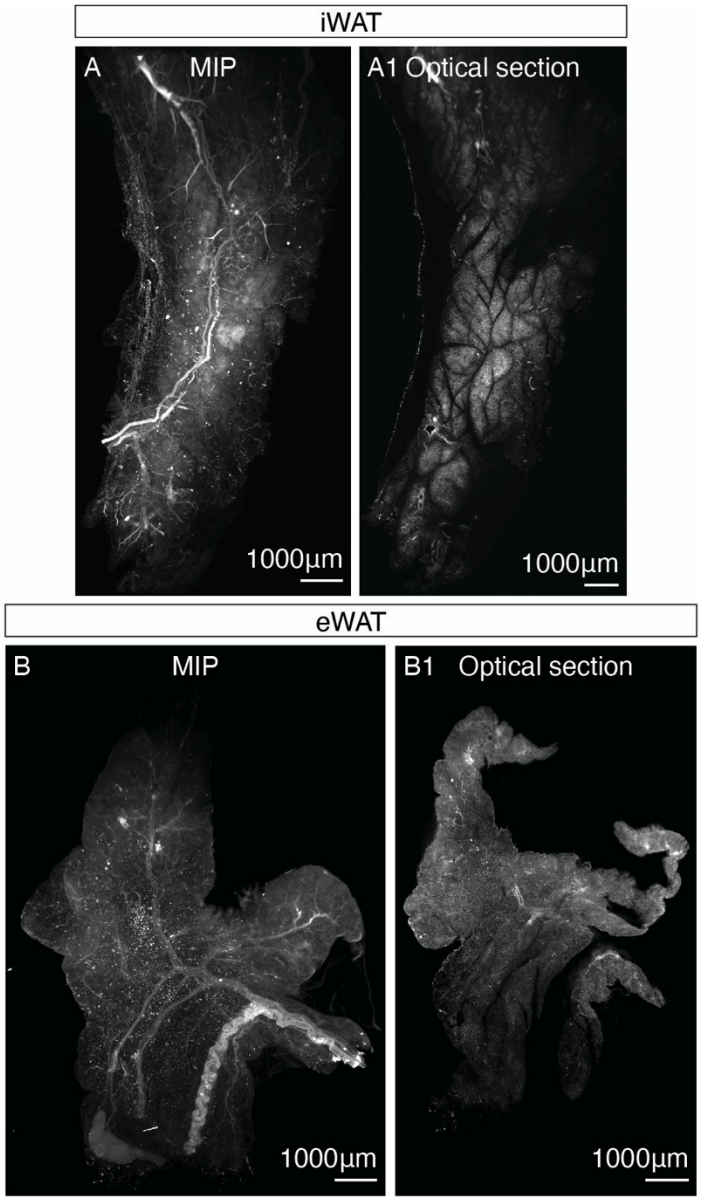

Figure 2.3 Tissue contours of white fat depots revealed by tissue autofluorescence signal. (**A-A1**) Tissue autofluorescence of the inguinal region of iWAT from an 8-week-old WT mouse: (**A**) Maximum intensity projection (MIP) of the entire z-stack and (**A1**) optical section through the middle of the tissue. (**B-B1**) Tissue autofluorescence of eWAT from an 8-week-old WT mouse: (**B**) MIP of the entire z-stack and (**B1**) optical section through the middle of the tissue.

2.4 Characterizing beige adipocyte biogenesis in murine white fat with whole tissue imaging

2.4.1 Beige adipocyte distribution in iWAT

We next applied Adipo-Clear to study beige fat biogenesis, a process marked by dynamic tissue remodeling, with the most notable change being the induction of uncoupling protein 1 (UCP1). UCP1 uncouples the mitochondrial proton gradient from ATP synthesis and is a well-accepted marker for visualizing thermogenic adipocytes. Here, we focused on active beige adipocytes that express high levels of UCP1. Relative to room temperature (RT), exposure of animals to 8°C resulted in a dramatic increase in *Ucp1* mRNA levels in iWAT (> 20-fold after 48 hours, > 50-fold after 1 week) (**Figure 2.4 A**). These increases in mRNA were mirrored by qualitatively similar increases in UCP1 protein content (**Figure 2.4 B-C**). mRNA levels of other marker genes, which have previously been described as enriched in thermogenic adipocytes (Seale et al., 2007), were also increased with cold exposure as short as following six hours of stimulation, with the most dramatic differences noted after at least 48 hours (**Figure 2.4 A**).

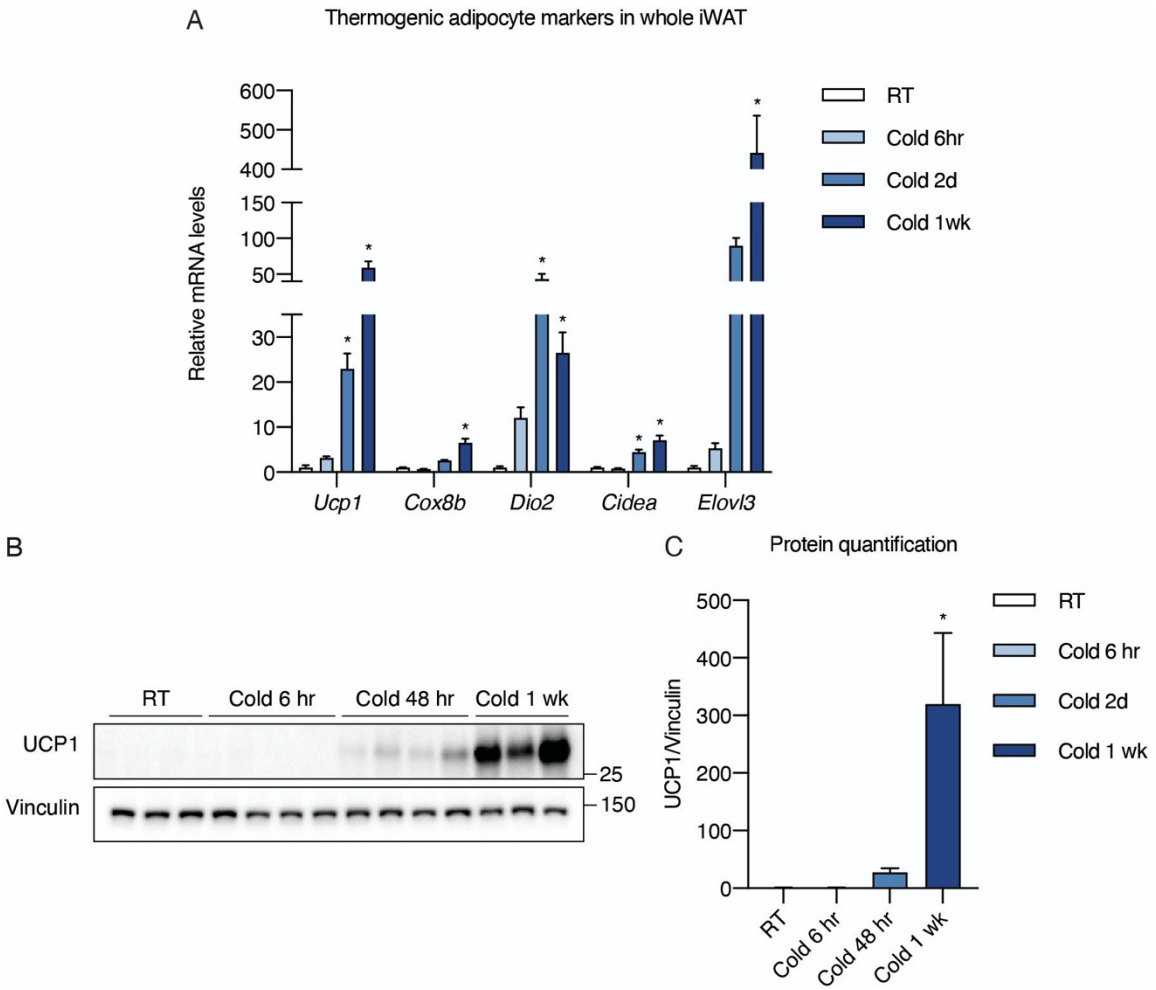

Figure 2.4 Molecular analysis of whole iWAT from cold exposed animals.
(**A**) qPCR analysis of thermogenic adipocyte markers from whole iWAT of WT C57BL6/J mice at RT, and following 6 hours, 48 hours, and 1 week at 8°C. Cold exposure was done with male 8-week-old mice, n=5. (**B**) Western blot of UCP1 and vinculin (loading control) from iWAT of the same animals as in **A**, n=3-4. Molecular weights are indicated as kDa. (**C**) Quantification of UCP1 with normalization to vinculin. (**A and C**) Data are normalized to RT group, presented as mean + SEM, and analyzed by one-way ANOVA followed by Bonferroni's multiple comparisons test. * denotes $p<0.05$ vs. RT group.

The gene expression and immunoblot analyses were performed on whole fat pads, but with 3D imaging of the entire subcutaneous fat pad using Adipo-Clear, we noticed prominent regional differences in beige fat induction. Our method first provides an overview of whole tissue architecture using low magnification images acquired with a light sheet fluorescence microscope. In addition, features of individual cells can be captured when specific regions are analyzed under high magnification. Cross sections taken from these 3D images, referred to as optical sections, provide better resolution at the single-cell level. Assisted by tissue autofluorescence, we can precisely locate any molecule of interest within the entire cleared tissue.

Using the lymph node (LN) as a landmark, we first divided the iWAT depot into two regions, hereafter referred to as the inguinal and dorsolumbar regions (**Figure 2.5 A-C**). 3D images of these two portions of the iWAT demonstrated that UCP1+ cells were predominantly in the inguinal region at RT (**Figure 2.5 D1-D2 and E1-E2**). This difference was more prominent when shown in optical sections with both low- and high-magnifications taken from the coronal midsection of the 3D images (**Figure 2.5 D3-D4 and E3-E4**). UCP1+ cells were dramatically increased in the inguinal region after 48 hours of cold exposure (**Figure 2.5 G1-G4**), whereas the dorsolumbar region showed only sparse UCP1+ cells localized around the LN (**Figure 2.5 F1-F4**). After 1 week of cold exposure, UCP1 staining was present throughout the inguinal region (**Figure 2.5 I1-I4**), and only at this point did we detect a substantial increase in the dorsolumbar region (**Figure 2.5 H1-H4**), with most UCP1+ cells towards the medial portion of this region (hereafter referred to as the dorsomedial region) (**Figure 2.5 H3**). Notably, the lateral portion of the dorsolumbar region (hereafter referred to as the dorsolateral region) contained minimal UCP1+ cells even with chronic cold exposure (**Figure 2.5 H3**). Similar images obtained after six hours of cold exposure or housing at thermoneutrality (30°C) demonstrated only scarce UCP1+ cells in either region (data not shown). Taken together, beige adipocytes in the inguinal region appear to be readily activated by cold, while those in the dorsomedial region are recruited only following long term cold exposure. Interestingly, the dorsolateral region appears to be resistant to cold-induced beige adipocyte formation.

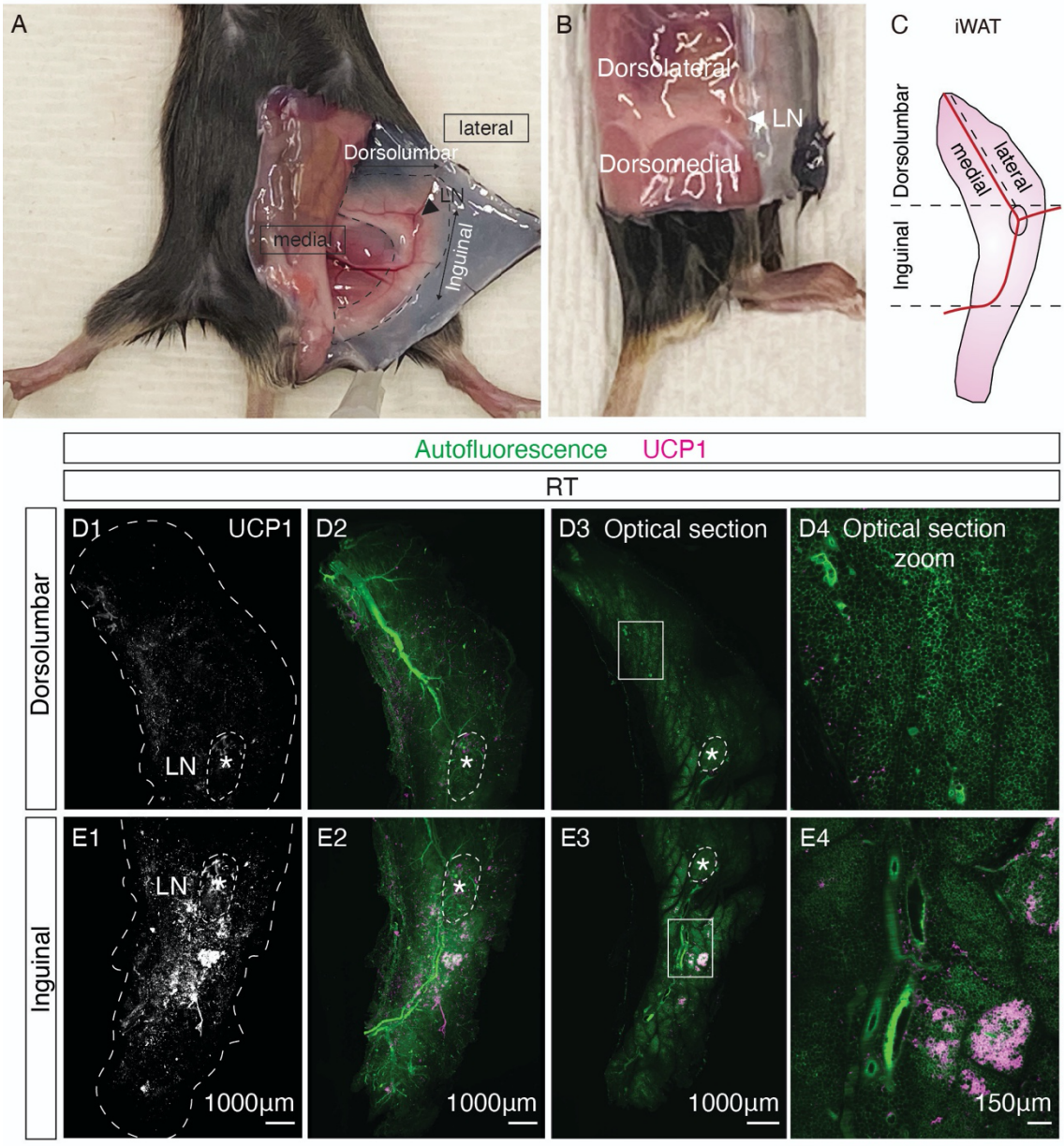
A
lateral
Dorsolumbar
LN
medial
Inguinal
B
Dorsolateral
LN
Dorsomedial
C
iWAT
Dorsolumbar
Inguinal
medial
lateral
Autofluorescence
UCP1
RT
Dorsolumbar
D1
UCP1
LN
D2
D3 Optical section
D4 Optical section zoom
Inguinal
E1
LN
E2
E3
E4
1000µm
1000µm
1000µm
150µm

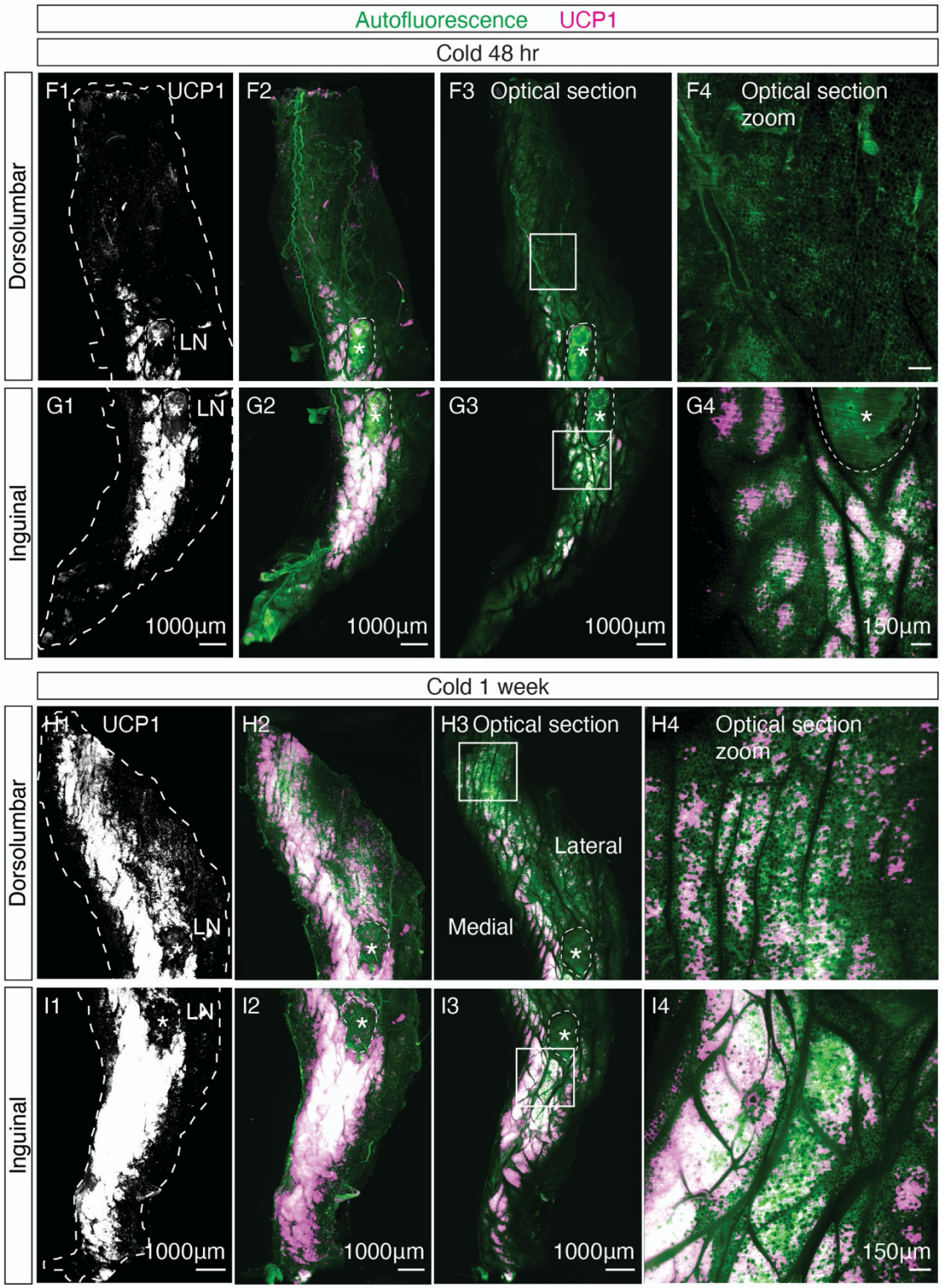
Autofluorescence UCP1
Cold 48 hr
Dorsolumbar
F1 UCP1
LN
F2
F3 Optical section
F4 Optical section zoom
Inguinal
G1
LN
1000µm
G2
1000µm
G3
1000µm
G4
150µm
Cold 1 week
Dorsolumbar
H1 UCP1
LN
H2
H3 Optical section
Lateral
Medial
H4 Optical section zoom
Inguinal
I1
LN
1000µm
I2
1000µm
I3
1000µm
I4
150µm

Figure 2.5 Characterization of beige adipocyte biogenesis in iWAT with whole tissue imaging.
(**A-B**) Anatomy of iWAT in a WT C57BL6/J male mouse. iWAT is outlined with a dashed contour. Lymph node (LN) is indicated by an arrowhead. Dorsolumbar and inguinal regions are indicated with two headed arrows. Medial and lateral directions are labeled. Using the inguinal lymph node as a landmark, the iWAT depot is divided into the inguinal and dorsolumbar regions. Using the main blood vessel that traverses the dorsolumbar region as a guide, this region is further divided into medial and lateral subregions, hereafter referred to as the dorsomedial and dorsolateral regions. (**C**) Schematic view of iWAT. Red lines represent main blood vessels. Dotted lines indicate boundaries of each region. (**D1-E4**) UCP1 immunostaining of whole iWAT from an 8-week-old WT C57BL6/J mouse housed at RT. (**D1-D4**) Images of the dorsolumbar region. (**E1-E4**) Images of the inguinal region. LNs are highlighted with dashed circles and indicated by asterisks. (**D1 and E1**) Maximum intensity projections (MIPs) of the entire z-stacks, stained with UCP1. Tissue contours are outlined based on tissue autofluorescence. (**D2 and E2**) MIPs of the entire z-stacks, presented as an overlay between UCP1 (magenta) and tissue autofluorescence (green). (**D3 and E3**) Optical sections (cross-section from the middle of the z-stack) from **D2** and **E2**, respectively. (**D4 and E4**) High-magnification images of boxed regions from **D3** and **E3**. (**F1-I4**) UCP1 staining of iWAT from 8-week-old WT C57BL6/J mice housed at 8°C for 48 hours (**F1-F4 and G1-G4**) and 1 week (**H1-H4 and I1-I4**). All panels are organized in the same order as the RT sample (**D1-D4 and E1-E4**). (**H3**) Medial and lateral orientations are indicated. Scale bars are indicated.

2.4.2 Beige adipocyte distribution in eWAT

Unlike subcutaneous fat, visceral fat is relatively resistant to beige fat biogenesis, although this assessment has been largely based on gene expression data and histologic studies of tissue sections. Although analysis of eWAT demonstrated increased mRNA levels of several markers of thermogenic beige fat after cold stimulation (**Figure 2.6 A**), the relative induction and absolute levels were substantially lower than in iWAT (*Ucp1* Ct values: iWAT RT 21.81 ± 2.06 vs. cold 1 week 15.047 ± 0.11; eWAT RT 32.34 ± 0.53 vs. cold 1 week 31.351 ± 0.71). Adipo-Clear 3D images and optical sections of eWAT at RT or following 1 week of cold exposure did not show any evidence of UCP1+ cells (**Figure 2.6 B-B2 and C-C2**), suggesting that at least with this stimulus there is no evident UCP1 induction in eWAT.

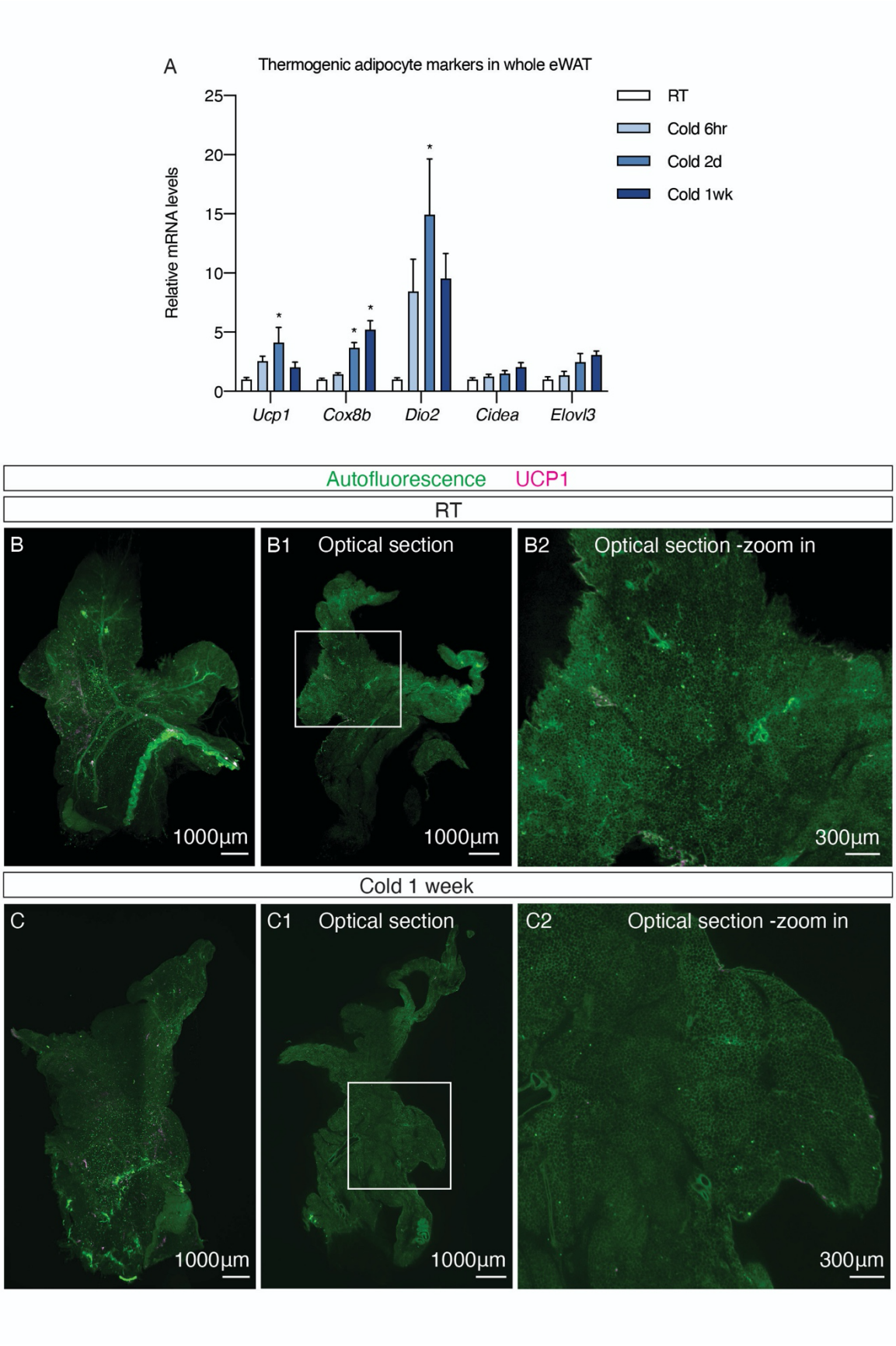
A
Thermogenic adipocyte markers in whole eWAT
Relative mRNA levels
25
20
15
10
5
0
RT
Cold 6hr
Cold 2d
Cold 1wk
*
Ucp1
Cox8b
Dio2
Cidea
Elovl3
Autofluorescence
UCP1
RT
B
1000µm
B1
Optical section
1000µm
B2
Optical section -zoom in
300µm
Cold 1 week
C
1000µm
C1
Optical section
1000µm
C2
Optical section -zoom in
300µm

Figure 2.6 Minimal cold-induced beige adipocyte biogenesis in eWAT.
(**A**) Normalized expression of thermogenic adipocyte-enriched genes in eWAT from WT 8-week-old male mice at RT, and following 6 hours, 48 hours, and 1 week at 8°C, n=5. Data are normalized to control RT group, presented as mean + SEM, and analyzed by one-way ANOVA followed by Bonferroni's multiple comparisons test. * denotes $p<0.05$ vs. RT group. (**B-B2**) UCP1 immunostaining of eWAT from an 8-week-old WT mouse housed at RT. (**B**) MIP of the entire z-stack presented as an overlay between the tissue autofluorescence (green) and UCP1 (magenta). (**B1**) A representative optical section from (**B**). (**B2**) High-magnification image of the boxed region in (**B1**). (**C-C2**) UCP1 immunostaining of eWAT from an 8-week-old WT mouse housed at 8°C for 1 week. All panels are shown in the same order as the RT sample (**B-B2**). Scale bars are as indicated in the images.

2.5 Molecular analysis of beige adipocyte regionality in iWAT

As whole tissue imaging of iWAT revealed striking regionality of beige adipocyte distribution, we further characterized the molecular signatures of distinct regions of the tissue using gene expression analysis. We dissected iWAT from animals housed at RT or exposed to 8°C, and prepared RNA from the inguinal (R1), dorsomedial (R2), and dorsolateral (R3) regions (**Figure 2.7**), the three regions that exhibited distinct patterns of beige adipocyte recruitment.

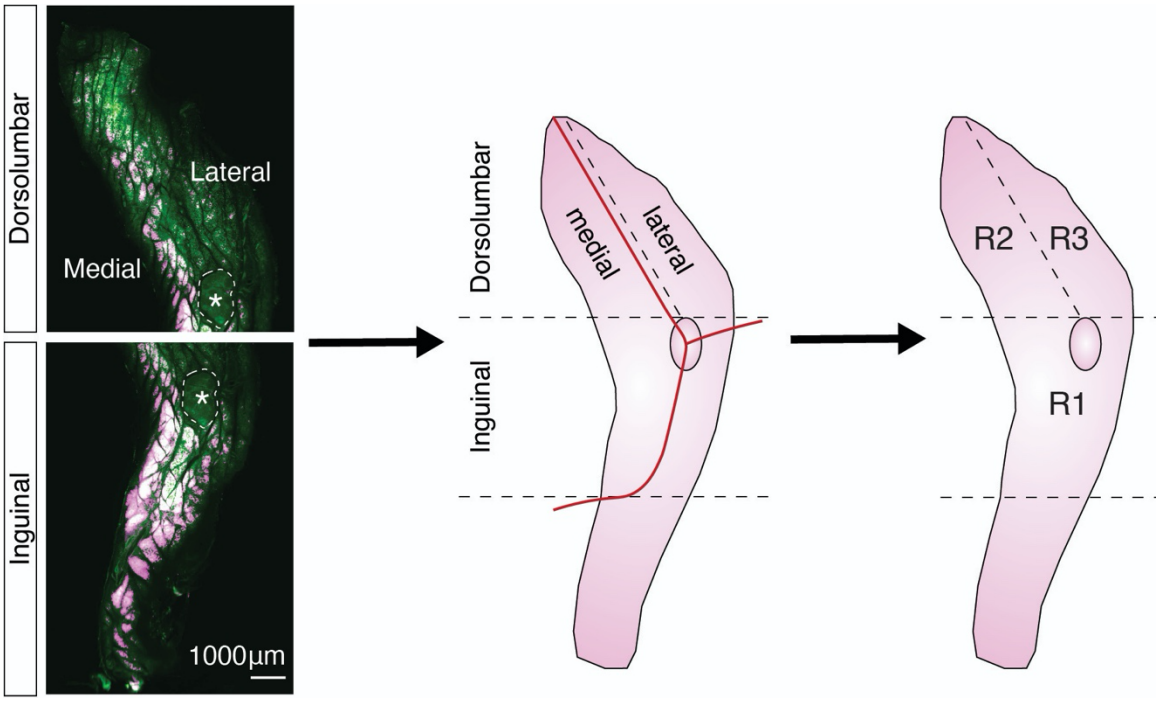

Figure 2.7 Illustration of the three regions in iWAT.
Schematic view of the three regions in iWAT. Inguinal – region 1 (R1), dorsomedial – region 2 (R2), dorsolateral – region 3 (R3).

Gene expression analysis demonstrated marked regional differences in thermogenic adipocyte-enriched genes following 48 hours and 1 week of cold exposure. (**Figure 2.8 A**). Specifically, the mRNA expression levels of these genes were highest in R1, intermediate in R2, and lowest in R3. Analyses of transcriptional components involved in beige adipocyte recruitment showed similar patterns. The mRNA levels of *Prdm16* exhibited more than 1.8-fold differences between R1 and R3 across all temperature conditions (**Figure 2.8 B**). In addition, *Ppargc1a*, which encodes for a known binding partner of PRDM16 (Seale et al., 2007), also showed a similar trend, with at least 3-fold increases in R1 relative to R3 following 48 hours and 1 week of cold stimulation (**Figure 2.8 B**). Notably, mRNA levels of factors that mark the differentiation and proper function of adipocytes (*Fabp4*, *Pparg*, and *Adipoq*) remained largely constant across the three regions, suggesting these regions harbor similarly differentiated adipocytes (**Figure 2.8 C**).

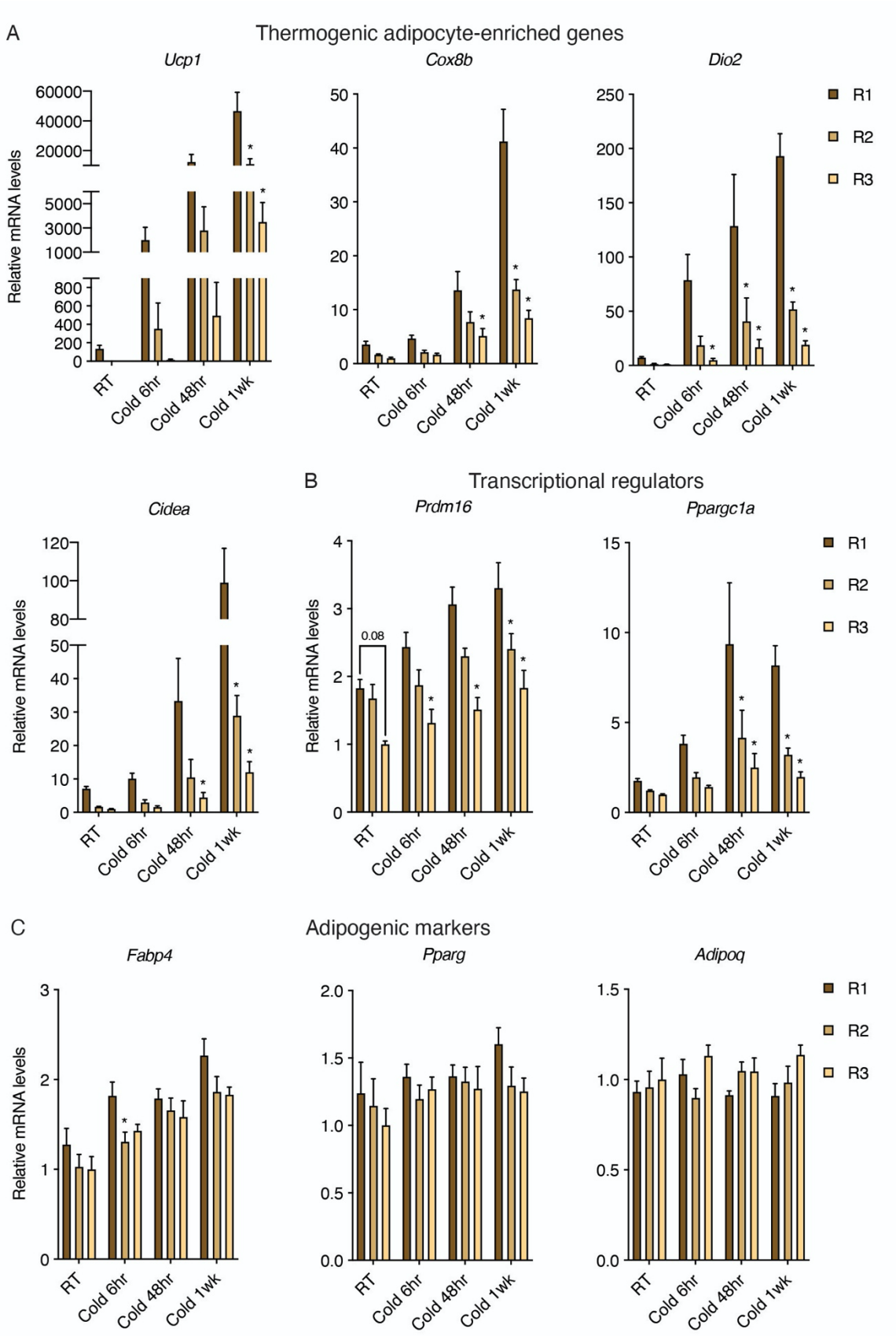
A
Thermogenic adipocyte-enriched genes
Ucp1
Cox8b
Dio2
Relative mRNA levels
R1
R2
R3
RT
Cold 6hr
Cold 48hr
Cold 1wk
B
Transcriptional regulators
Cidea
Prdm16
Ppargc1a
0.08
C
Adipogenic markers
Fabp4
Pparg
Adipoq

Figure 2.8 Gene expression analysis of iWAT regionality.
(**A-C**) WT C57BL6/J 9-week-old mice were housed at RT, and following 6 hours, 48 hours, and 1 week at 8°C. n=3-4. Inguinal (R1), dorsomedial (R2), and dorsolateral (R3) regions were dissected from iWAT following guidelines described in **Figure 2.7** and **Chapter 5.4**. qPCR analysis of (**A**) thermogenic adipocyte-enriched genes, (**B**) transcriptional regulators of beige adipocyte development and function, and (**C**) adipogenic markers was performed. Data are normalized to RT R3 group, presented as mean + SEM, and analyzed by two-way ANOVA followed by Bonferroni's multiple comparisons test. * denotes $p<0.05$ vs. R1 of that temperature group.

It was particularly interesting that *Prdm16* mRNA levels appeared different between R1 and R3 even under basal conditions (**Figure 2.8 B**, RT group). Since the role of *Prdm16* as the master transcriptional regulator of beige adipocyte development and function has been well established, it is possible that the regional difference in *Prdm16* expression levels reflects different propensities for beige fat recruitment in distinct regions. We further compared *Prdm16* mRNA and protein levels across multiple fat depots from animals housed at RT (**Figure 2.9 A**). Consistent with previous findings, *Prdm16* mRNA was most enriched in interscapular brown fat (iBAT) while barely expressed in eWAT (Cohen et al., 2014). Although iWAT was previously reported to express intermediate levels of *Prdm16* mRNA (Cohen et al., 2014), regional dissection revealed that R1 naturally expressed high levels of *Prdm16* comparable to iBAT (**Figure 2.9 A,** iWAT R1 vs. iBAT). On the other hand, while R3 exhibited the lowest levels of *Prdm16* mRNA among the three iWAT regions, it still showed significantly higher levels than eWAT (**Figure 2.9 A,** iWAT R3 vs. eWAT). Consistently, analysis of PRDM16 protein revealed the same pattern (**Figure 2.9 B**). Altogether, the key regulator of beige adipocyte phenotype, *Prdm16*, appears to be naturally enriched in the inguinal region of iWAT, suggesting that different iWAT regions (1) may harbor adipocytes with distinct intrinsic features (see **Chapter 4** for more discussion) and/or (2) could contain unique structures or cell types other than adipocytes that affect beige adipocyte recruitment.

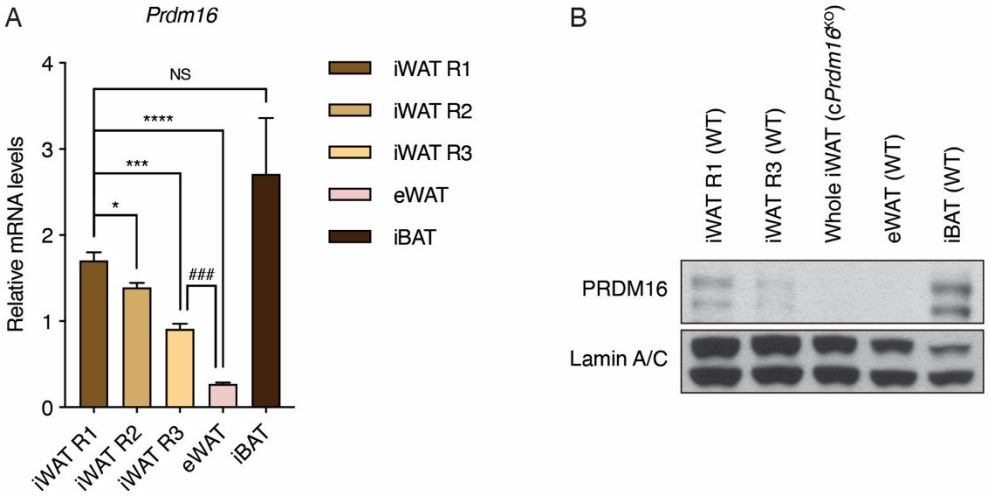

Figure 2.9 *Prdm16* mRNA and protein expression across various fat depots.
(**A**) Normalized *Prdm16* mRNA levels in iWAT R1, iWAT R2, iWAT R3, eWAT, and iBAT from WT C57BL6/J 6-week-old mice housed at RT. Data are normalized to eWAT, presented as mean + SEM, and analyzed by student's t test with (1) each group compared to iWAT R1 and (2) between iWAT R3 and eWAT * $p<0.05$, ***$p<0.001$, ****$p<0.0001$ vs. iWAT R1 group. ###$p<0.001$ iWAT R3 vs. eWAT. (**B**) Western blot of PRDM16 and lamin A/C (loading control) of various fat depots from WT and adipocyte-specific *Prdm16* knockout (c*Prdm16*^{KO}) 8-week-old mice housed at RT.

2.6 Characterizing the sympathetic network in murine white fat

2.6.1 Organization of the sympathetic nervous system in iWAT

To explore possible mechanisms underlying the propensity for beige fat biogenesis, we performed whole-tissue imaging of sympathetic nerve projections to adipose tissue. It has been well-established that the sympathetic nervous system plays a crucial role in cold-induced beige fat recruitment. It is possible that differential sympathetic drive may lead to beige adipocyte regionality. Maximum intensity projections of the entire iWAT showed dense staining of sympathetic fibers with tyrosine hydroxylase (TH), a maker for sympathetic fibers, which acts as the rate-limiting enzyme in the norepinephrine biosynthesis pathway (**Figure 2.10 A-A1**). Optical sections (**Figure 2.10 A2 and B-B1**) highlighted three distinct patterns of TH staining: (1) along blood vessels, (2) sympathetic nerve bundles, and (3) neurite projections into the adipose tissue parenchyma (parenchymal innervation) (labeled in **Figure 2.10 B-B1**). Although a prior study reported that adipose tissue macrophages can express TH and produce catecholamine (Nguyen et al., 2011), we did not observe any TH signal localized to CD68-labeled macrophages (**Figure 2.10 C-C1**).

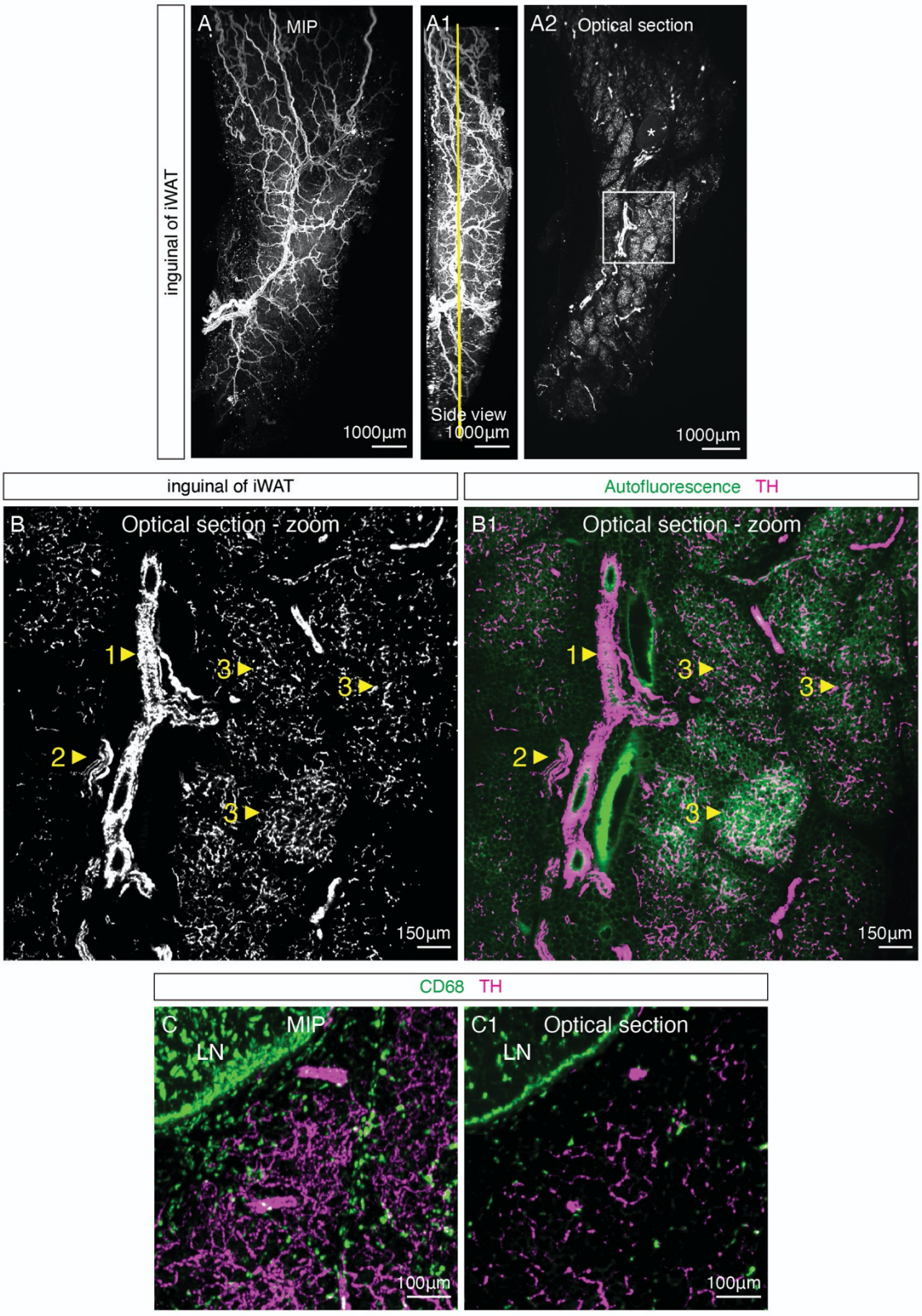
inguinal of iWAT
A
MIP
1000µm
A1
Side view
1000µm
A2
Optical section
1000µm
inguinal of iWAT
Autofluorescence TH
B
Optical section - zoom
1
2
3
3
3
3
150µm
B1
Optical section - zoom
1
2
3
3
3
150µm
CD68 TH
C
MIP
LN
100µm
C1
Optical section
LN
100µm

Figure 2.10 Visualizing the sympathetic nervous system in iWAT.
(**A-A2 and B-B1**) TH immunostaining of the inguinal region of iWAT from an 8-week-old WT C57BL6/J male mouse. (**A**) MIP of the entire z-stack in the xy plane. (**A1**) MIP of the entire stack in the yz plane, a 90° rotation from **A**. An optical section is highlighted in yellow to indicate depth into the tissue. (**A2**) Optical section at the indicated level in **A1**. (**B-B1**) High-magnification images of boxed region in **A2**. Arrowheads indicate distinct patterns of sympathetic innervation: (1) blood vessel innervation; (2) nerve bundle; (3) adipose parenchymal innervation. (**B**) TH. (**B1**) Tissue autofluorescence (green) and TH (magenta). (**C-C1**) CD68 (green) and TH (magenta) co-staining of iWAT from an 8-week-old WT C57BL6/J male mouse: (**C**) MIP and (**C1**) optical section. Scale bars are indicated.

As the parenchymal TH+ fibers, which project into lobules where adipocytes are located, are likely important for sympathetic control of adipocyte function, we further examined the parenchymal innervation structure with computational neurite tracing and confocal imaging. Assisted by tissue contours shown in the autofluorescence image, single lobules could be isolated computationally (**Figure 2.11 A1-A4**), which allowed us to analyze TH staining within a small structural unit in detail (**Figure 2.11 B1**). By computational tracing of the finer TH+ neurites within the isolated lobule (**Figure 2.11 B2**), we observed that the parenchymal neurites in the inguinal region of iWAT were organized in a dense network within each lobule (**Figure 2.11 B3-B4**).

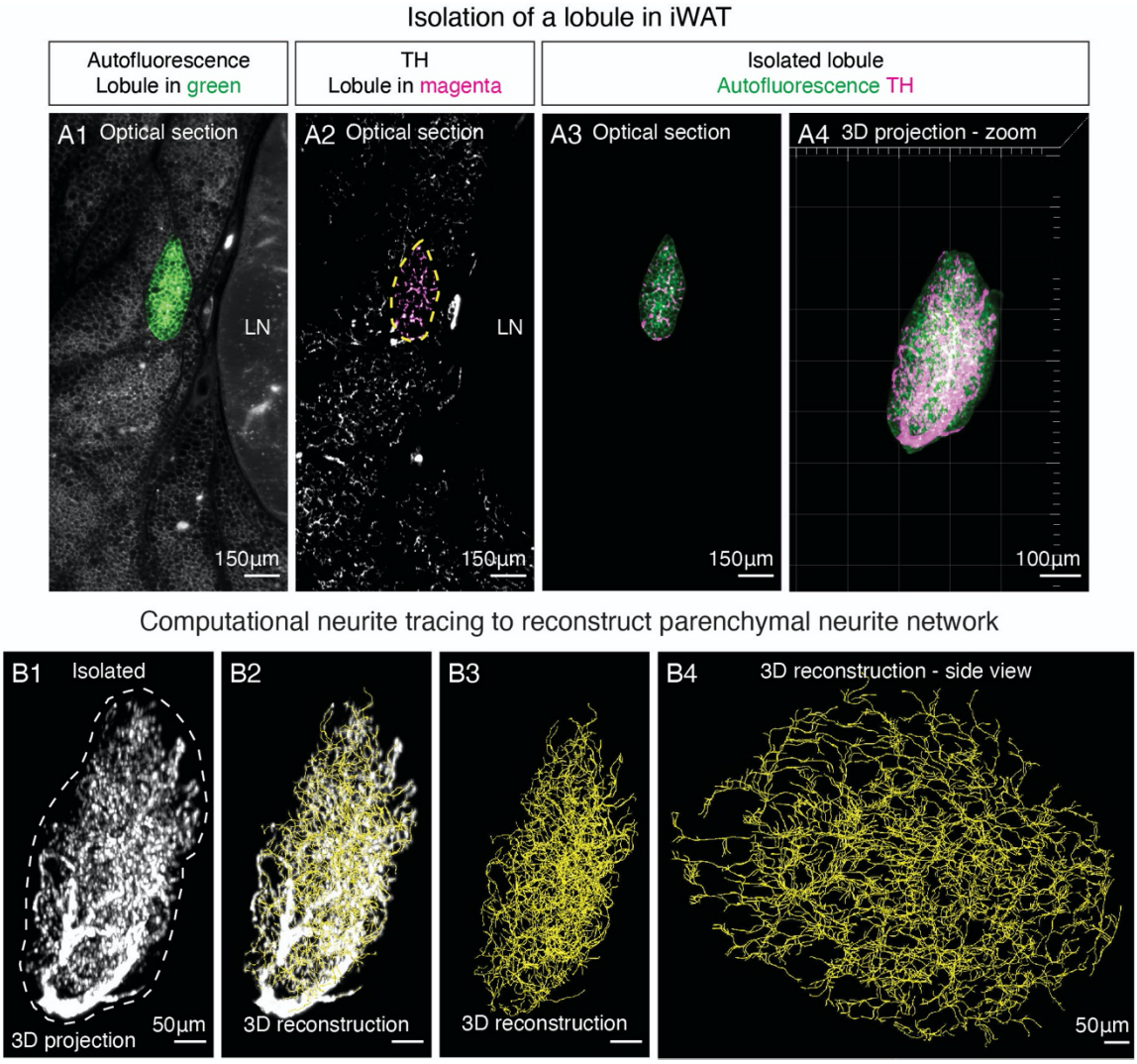

Figure 2.11 Reconstruction of parenchymal innervation in iWAT with neurite tracing. (**A1-A4**) Virtual isolation of a lobule in the same iWAT sample as shown in **Figure 2.10 A-B**, using the "Surface" tool with masking option in Imaris. (**A1**) Optical section showing tissue autofluorescence, with one isolated lobule highlighted in green. (**A2**) Optical section of the same plane as **A1** with TH labeling. Sympathetic fibers in the isolated lobule are highlighted in magenta. (**A3 and A4**) Optical section (**A3**) and 3D projection (**A4**) of an overlay of tissue autofluorescence (green) and TH (magenta) of the isolated lobule. (**B1-B4**) Reconstruction of parenchymal neurites in the isolated lobule in **A4**. (**B1**) 3D projection of TH labeling in the isolated lobule shown in **A4**. (**B2**) 3D reconstruction of the TH signal shown in **B1** using the "Filament" tool of Imaris. An overlay between TH signal and reconstructed fibers (yellow) is presented. (**B3 and B4**) Reconstructed sympathetic fibers within the lobule presented as (**B3**) top- and (**B4**) side-view projections. Lymph nodes are indicated as LN. Scale bars are as indicated in the images.

To visualize the parenchymal innervation with higher resolution, we next performed confocal microscopy on cleared tissue. Consistent with the light sheet images, we observed TH+ neurites surrounding adipocyte contours highlighted by tissue autofluorescence (**Figure 2.12 A-C**). As sympathetic projections in target organs may follow blood vessels, we analyzed the parenchymal innervation pattern in relation to capillaries labeled by CD31 (also known as PECAM), a marker for endothelial cells that line vasculature. We observed dense vascularization of adipocytes, with CD31+ capillaries surrounding almost all adipocytes (**Figure 2.12 B, D, and F**). While some neurites appeared close to blood vessels, some clearly localized to areas where the vasculature was absent (**Figure 2.12 E**, indicated by arrowheads), indicating that the sympathetic network and the vasculature are not completely associated.

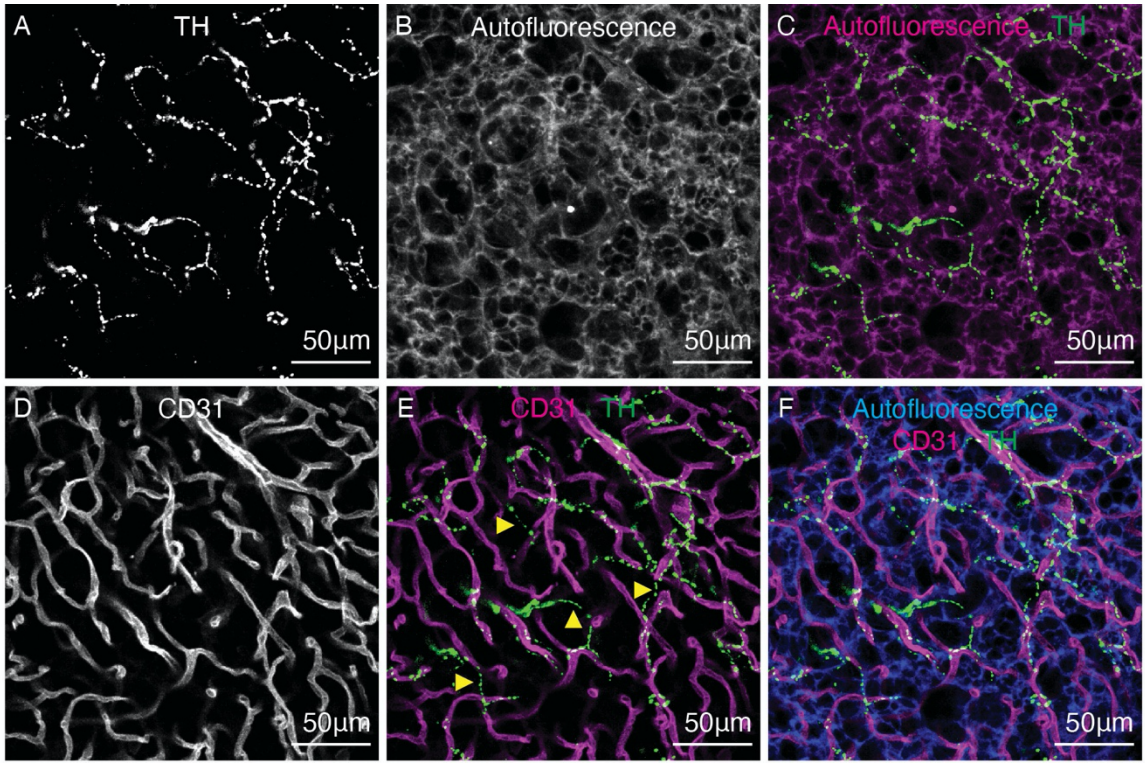

Figure 2.12 Visualization of sympathetic parenchymal innervation with confocal microscopy.

(**A-F**) TH and CD31 co-staining in an iWAT sample collected from an 8-week-old WT mouse housed at RT. (**A**) TH. Imaging was performed using a confocal microscope with a 20X objective. MIPs of 5 µm z-stacks from a representative lobule in the inguinal region are presented. (**B**) Autofluorescence. (**C**) Overlay of autofluorescence (magenta) and TH (green). (**D**) CD31. (**E**) Overlay of CD31 (magenta) and TH (green). Yellow arrowheads indicate TH+ filaments that do not follow capillaries. (**F**) Overlay of CD31 (magenta), TH (green), and autofluorescence (blue). Scale bars are indicated.

Of note, many neurite filaments resemble strings of beads in high-resolution images (**Figure 2.12 A**). We next performed computational neurite tracing in 3D images collected by confocal microscopy to delineate the organization of the parenchymal innervation network (**Figure 2.13 A-B**). Neurites that appeared as smooth filaments were pseudo-colored in green (**Figure 2.13 B-C**), while those that exhibited "beads-on-a-string" morphology were pseudo-colored in yellow (**Figure 2.13 B and D**). Interestingly, we found that the "beads-on-a-string" structures were only present at the neurite terminals (**Figure 2.13 C-D**). In fact, this terminal morphology is consistent with previous descriptions of varicosities, bulbous enlargements located along sympathetic postganglionic axons that release neurotransmitters into the target tissue (Burnstock, 2008). These morphological analyses indicate that the sympathetic communication with adipocytes in iWAT is likely through simultaneous release of norepinephrine from the varicosities over a large area of the tissue, rather than through defined neuroeffector junctions between axon terminals and individual fat cells.

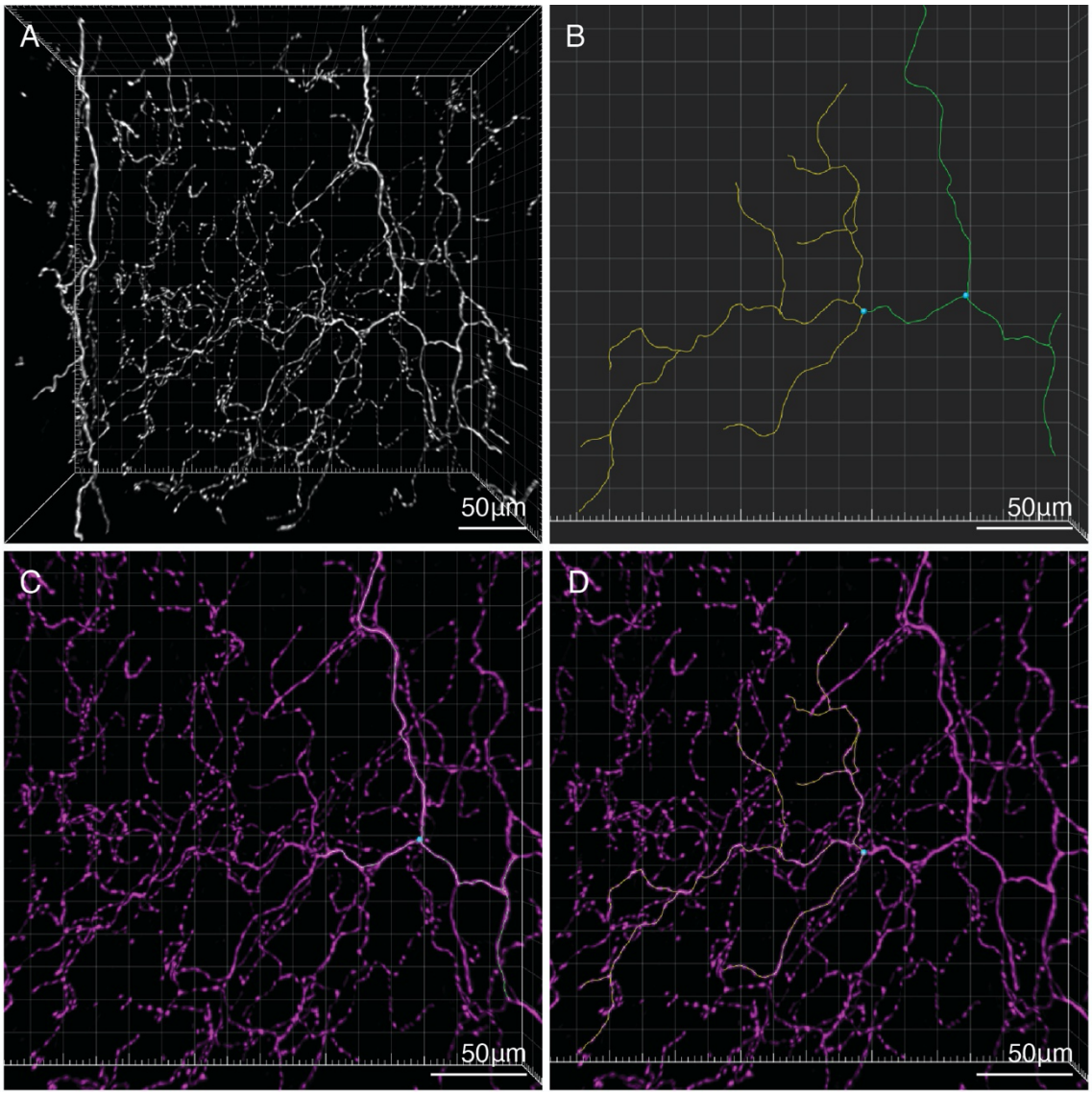

Figure 2.13 Sympathetic axon terminals in iWAT contain varicosities.
Computational neurite tracing was performed in a 3D image collected from the inguinal region of iWAT immunostained with TH. (**A**) 3D view of the neurite network with the TH channel. (**B**) Filaments generated by tracing the TH signal using the "Filament" tool in Imaris. Green filaments were constructed from neurites that resemble smooth fibers. Yellow filaments were generated from neurites that contain varicosities. (**C**) Overlay between the green filament in **B** and the TH signal. (**D**) Overlay between the yellow filament in **B** and the TH signal. Scale bars are indicated.

2.6.2 Regionality of sympathetic parenchymal innervation in iWAT

We next compared sympathetic structures in the inguinal and dorsolateral regions of iWAT to explore whether the sympathetic innervation patterns could explain the striking regional variation in beige adipocyte recruitment. We analyzed the sympathetic innervation pattern using the same sample as in **Figure 2.5 D1-E4**. Indeed, whole-sample optical sections showed variations in parenchymal neurite density across the tissue, with the inguinal region having denser TH signals than the dorsolateral region (**Figure 2.14 A-A3 vs. Figure 2.14 B-B3**). We then used a high magnification objective to sample detailed variations within these two regions of the tissue (numbered 1-3 in **Figure 2.14 A3**) and saw regional differences in parenchymal neurite density. Specifically, greater neurite density was seen in the two areas (2 and 3) sampled within the inguinal region, whereas much lower neurite density was observed in the dorsolateral region (1) (**Figure 2.14 C1-C3 vs. D1-D3 and E1-E3**).

In each specific sub-region, we randomly isolated small cubic volumes contained within lobules., which allowed us to unbiasedly sample parenchymal neurites within each region (see **Chapter 5.3** for details). We performed virtual reconstruction of TH staining to obtain total neurite length in individual cubic volumes. Parenchymal neurite density was calculated by normalizing total neurite length to the volume of each cube. This quantitative structural analysis of parenchymal innervation revealed more than 100% increases in neurite density in the two inguinal regions relative to the dorsolateral region (**Figure 2.14 F**). Moreover, assisted by both low and high magnification images, we observed that all UCP1+ adipocytes were located in regions with dense parenchymal neurites (**Figure 2.14 A4, B4, C4, D4, and E4**). Taken together, the inguinal region of iWAT exhibits denser parenchymal innervation (under basal condition) and higher propensity for beige adipocyte recruitment than the dorsolateral region, suggesting an association between these two structures.

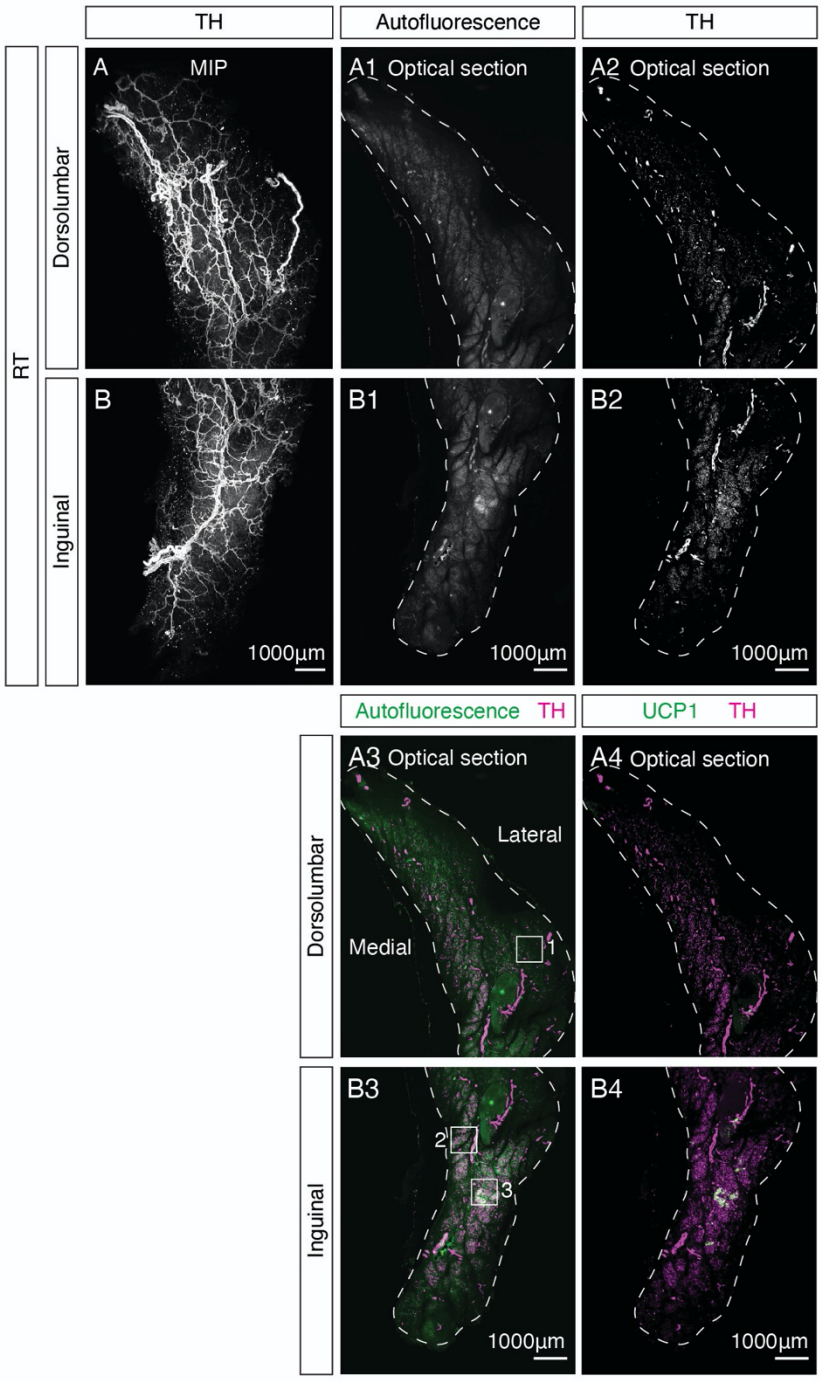
TH
Autofluorescence
TH
RT
Dorsolumbar
Inguinal
A
MIP
A1 Optical section
A2 Optical section
B
B1
B2
1000µm
Autofluorescence TH
UCP1 TH
A3 Optical section
A4 Optical section
Lateral
Medial
1
B3
B4
2
3

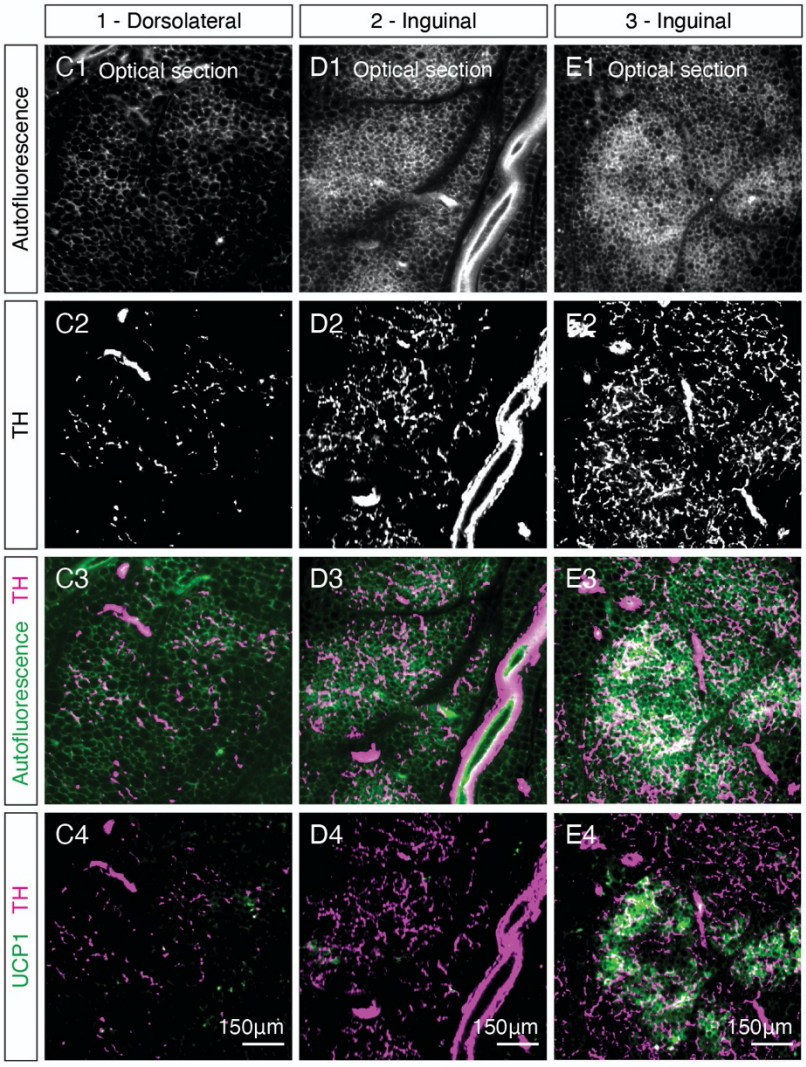
1 - Dorsolateral
2 - Inguinal
3 - Inguinal
Autofluorescence
TH
Autofluorescence TH
UCP1 TH
C1 Optical section
D1 Optical section
E1 Optical section
C2
D2
E2
C3
D3
E3
C4
D4
E4
150µm
150µm
150µm

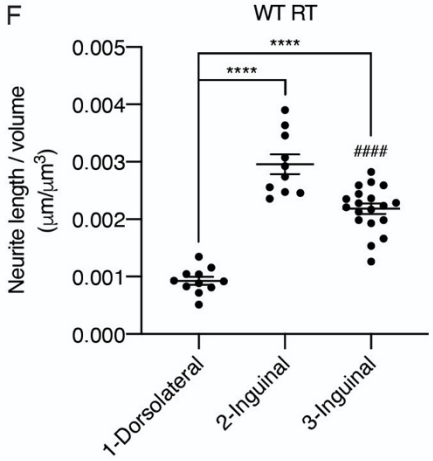
F
WT RT
****
****
####
Neurite length / volume
(µm/µm³)
0.005
0.004
0.003
0.002
0.001
0.000
1-Dorsolateral
2-Inguinal
3-Inguinal

Figure 2.14 Regional variation of sympathetic parenchymal neurite density in iWAT.
(**A-A4 and B-B4**) TH immunostaining of iWAT from an 8-week-old WT mouse housed at RT (same sample as **Figure 2.5 D1-E4**). (**A-A4**) Images of the dorsolumbar region. (**B-B4**) Images of the inguinal region. (**A and B**) MIPs of the entire z-stacks with TH labeling. Optical sections showing tissue autofluorescence (**A1 and B1**), TH labeling (**A2 and B2**), overlay of tissue autofluorescence (green) and TH (magenta) (**A3 and B3**), and overlay of UCP1 (green) and TH (magenta) (**A4 and B4**). (**C1-E4**) High-magnification optical sections of boxed sub-regions from (**A3 and B3**): (**C1-C4**) 1-dorsolateral, (**D1-D4**) 2-inguinal, and (**E1-E4**) 3-inguinal. (**C1-E1**) Tissue autofluorescence. (**C2-E2**) TH labeling. (**C3-E3**) Overlay of tissue autofluorescence (green) and TH (magenta). (**C4-E4**) Overlay of UCP1 (green) and TH (magenta). Scale bars are indicated. (**F**) Quantification of sympathetic parenchymal neurite density in the three sub-regions, with total neurite length normalized to regional volume. Individual data points are plotted with mean ± SEM and analyzed by two-way ANOVA followed by Bonferroni's multiple comparisons test. **** denotes $p<0.0001$ vs. 1-dorsolateral. #### denotes $p<0.0001$ 2-inguinal vs. 3-inguinal.

2.6.3 Organization of the sympathetic nervous system in eWAT

As tissue autofluorescence signal revealed a rather amorphous tissue architecture in eWAT (**Figure 2.3**), we wondered whether the sympathetic innervation is organized differently in this visceral fat depot compared to iWAT. Interestingly, eWAT showed a dramatically different pattern of sympathetic innervation (**Figure 2.15 A-A2**). Prominent main nerve fibers extended into various protrusions of the tissue. Finer neurites then branched from the main fibers to project into tissue parenchyma. Upon high magnification examination, we found that the main sympathetic fibers mostly ran along blood vessels (**Figure 2.15 B-B1,** indicated by arrowheads in **B1**). However, minimal TH+ neurites were found to densely innervate tissue parenchyma of eWAT (**Figure 2.15 B-B1**). The distinct organization of sympathetic innervation in iWAT and eWAT suggest that distinct mechanisms may underlie sympathetic control of adipocytes in various fat depots.

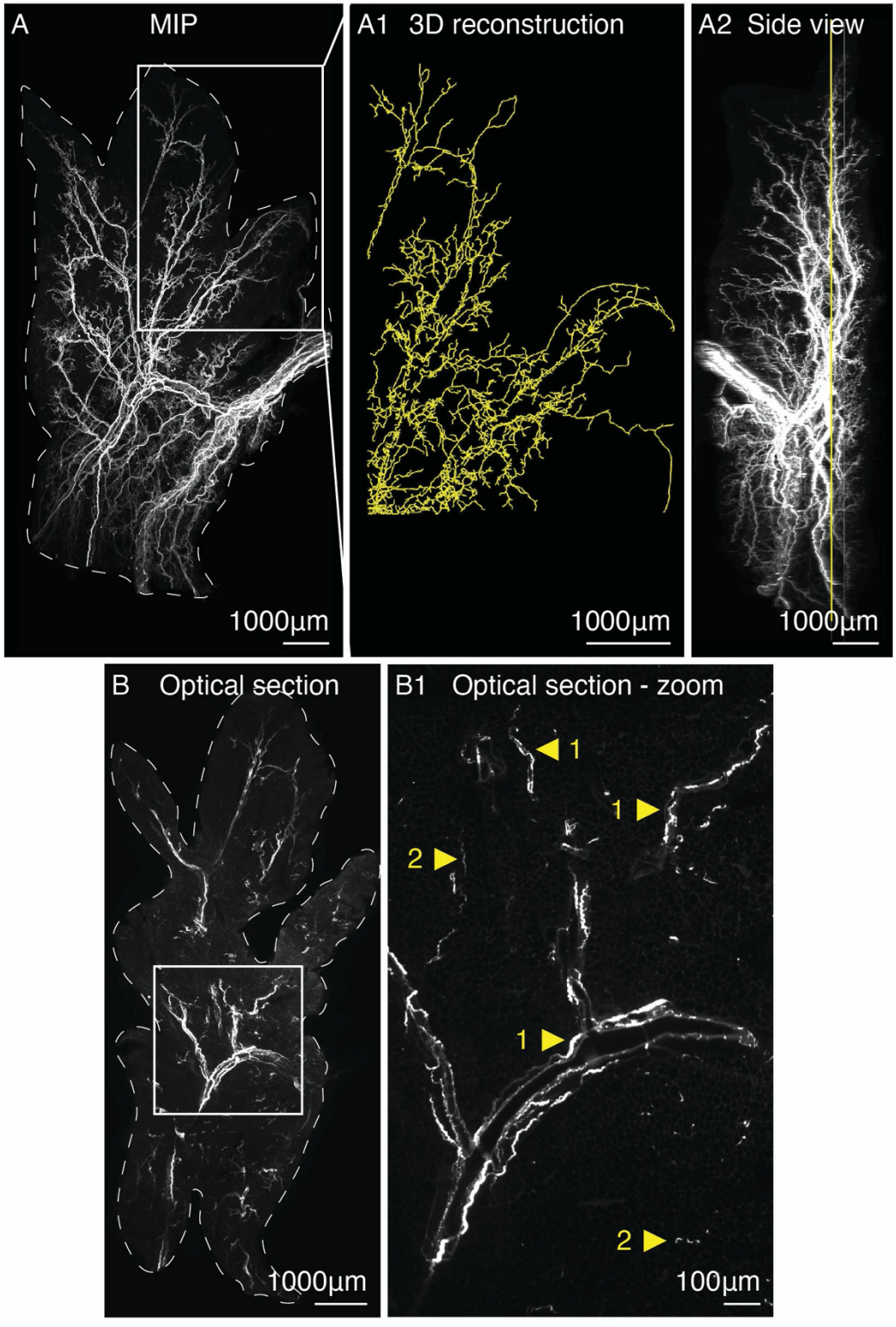
A
MIP
1000µm
A1 3D reconstruction
1000µm
A2 Side view
1000µm
B Optical section
1000µm
B1 Optical section - zoom
1
1
2
1
2
100µm

Figure 2.15 Visualizing the sympathetic nervous system in eWAT.
TH immunostaining of whole eWAT from an 8-week-old WT C57BL6/J male mouse. (**A**) MIP of the entire z-stack in the xy plane. Tissue contour is drawn based on the autofluorescence signal (not shown). (**A1**) Computational neurite tracing of the sympathetic fibers located in the boxed region in **A**. (**A2**) MIP of the entire stack in the yz plane, a 90° rotation from **A**. An optical section is highlighted in yellow to indicate depth into the tissue. (**B**) Optical section at the indicated level in **A2**. Tissue contour is drawn based on the autofluorescence signal (not shown). (**B1**) High-magnification image of boxed region in **B**. Arrowheads indicate distinct patterns of sympathetic innervation: (1) along blood vessel; (2) sparse adipose parenchymal innervation. Scale bars are indicated.

2.7 Discussion

We have described here a whole-tissue immunostaining and clearing technique, Adipo-Clear, which permits simultaneous evaluation of multiple structures in whole adipose tissue. This new tool has provided us with several new observations. First, we found a striking regional variation in beige fat biogenesis within iWAT. Second, we noted that subcutaneous (iWAT) and visceral fat (eWAT) have different architecture, likely reflecting their distinct developmental origins and physiological roles. Third, we delineated the pattern of sympathetic innervation of adipose tissue, including large nerve fibers and fine neurite projections that differ vastly between subcutaneous and visceral depots. The sympathetic innervation of iWAT also demonstrates a regional pattern that strongly associates with the beige adipocyte distribution pattern, with regions having denser parenchymal fibers corresponding to those showing more beige adipocyte biogenesis.

These findings highlight the value of 3D whole-tissue imaging as a discovery tool. The tissue level alterations we identified between iWAT and eWAT may help explain the strikingly different phenotypes observed in individuals with subcutaneous and visceral obesity. It is possible that the sparse sympathetic innervation of eWAT may partially contribute to the lack of cold-induced beige adipocyte formation in this depot. In addition, without a comprehensive analysis of the entire iWAT fat pad, we would not have appreciated the dramatic differences in beige fat biogenesis between the inguinal and the dorsolateral regions. Although we saw corresponding alterations in sympathetic neurite density in these regions, our data does not exclude the possibility that adipocytes located in distinct regions of iWAT may have intrinsic differences and may even derive from distinct developmental lineages. **Chapter 3 and 4** will focus on investigating whether regional beige adipocyte distribution is due to variable sympathetic innervation or intrinsic properties of adipocytes in these regions.

In addition, our studies using high-resolution 3D images provided a better understanding of how sympathetic control of beige adipocyte biogenesis is achieved. By carefully analyzing sympathetic parenchymal neurite morphology, organization, and density in iWAT under basal conditions, we found that parenchymal neurites in the inguinal region of iWAT are organized in a dense network that tightly surround adipocytes, with neurite terminals containing varicosities that can release norepinephrine upon sympathetic activation. Interestingly, a recent study found that beige adipocytes express high levels of connexin 43, a gap junction protein that facilitates propagation of signals such as cyclic AMP to adjacent cells (Zhu et al., 2016). Disruption of gap junction formation blocked the emergence of UCP1+ adipocytes following sympathetic activation to the same extent as did sympathetic denervation (Zhu et al., 2016), suggesting that propagation of sympathetic signals among coupled beige adipocytes is equally important as having intact sympathetic innervation. Altogether, effective beige adipocyte recruitment upon sympathetic activation likely requires 1) norepinephrine released from neurite terminal varicosities located in the near vicinity and 2) propagation of the neuronal signal to coupled beige adipocytes (**Figure 2.16**).

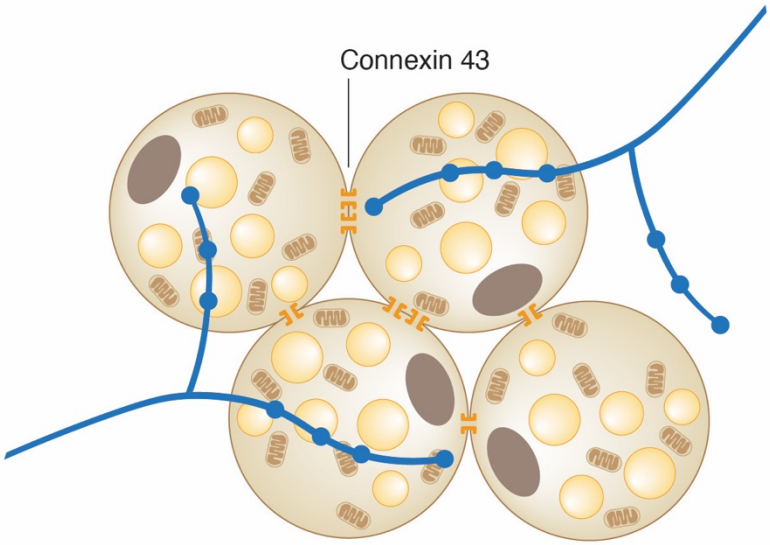

Figure 2.16 Schematic illustration of the interaction between sympathetic axon terminals and beige adipocytes in iWAT.

CHAPTER 3. The role of beige adipocytes in sympathetic neurite patterning.

3.1 Introduction

The sympathetic nervous system plays an important role in regulating two key aspects of adipose tissue function: lipolysis and thermogenesis. Sympathetic stimulation, such as cold exposure, induces sympathetic nerve endings to release norepinephrine in adipose tissue. This neurotransmitter activates β-adrenergic signaling in thermogenic brown and beige adipocytes, resulting in enhanced thermogenesis and lipolysis (Cannon and Nedergaard, 2004; Hsieh and Carlson, 1957). The important role of sympathetic stimulation in thermogenesis has driven great interest in understanding the structural and molecular details of sympathetic control of thermogenic adipocytes.

It has been reported by us and several other groups that dense sympathetic parenchymal innervation is observed in both iBAT and the inguinal region of iWAT, where beige adipocytes are primarily located. However, sparse innervation is found in eWAT and the dorsolateral region of iWAT, an area of the tissue that is devoid of beige adipocytes even under long term cold stimulation (Chi et al., 2018a; Dichamp et al., 2019; Huesing et al., 2020; Murano et al., 2009; Zeng et al., 2019). The strong association between thermogenic adipocytes and dense sympathetic neurites as well as the association between white adipocytes and sparse innervation suggest that adipocyte type may determine the density of sympathetic parenchymal innervation. Indeed, brown adipocyte-derived factors such as S100B and TGFβ1 have been shown to act on the sympathetic nervous system to regulate its structure and activity (Hu et al., 2020; Zeng et al., 2019). However, it remains largely unclear whether beige adipocytes, which are embedded in white fat depots, modulate their sympathetic innervation.

It has been well established that beige adipocyte development and function is determined by a transcriptional regulator, PRDM16 (Cohen et al., 2014; Seale et al., 2011). Mice with adipocyte-specific PRDM16 knockout (constitutive *Prdm16*^{KO} or c*Prdm16*^{KO}) are unable to recruit beige adipocytes in iWAT when exposed to cold, but exhibit normal development and function of brown and white adipocytes (Cohen et al., 2014). We therefore used c*Prdm16*^{KO} mice to achieve specific ablation of beige adipocyte function and evaluated how beige adipocytes affect sympathetic innervation. Assisted by Adipo-Clear and whole-tissue imaging, we found that the density of sympathetic parenchymal neurites in close apposition to beige adipocytes is regulated by a PRDM16-dependent program (Chi et al., 2018a). Furthermore, we found that beige adipocytes are required for sympathetic axon growth during a critical early postnatal period, but dispensable for maintaining sympathetic structure in adulthood (Chi et al., 2021).

3.2 Sympathetic neurite density in iWAT is regulated by *Prdm16* in beige adipocytes

To examine whether beige adipocytes play a role in regulating sympathetic innervation, we took advantage of the c*Prdm16*^{KO} model where beige adipocytes take on a phenotype more similar to white adipocytes due to the absence of PRDM16, the master transcriptional regulator of beige adipocyte phenotype (Cohen et al., 2014). We first confirmed that *Prdm16* deletion in adipocytes indeed blocked beige adipocyte recruitment following cold challenge in adult mice. Specifically, while cold exposure significantly induced mRNA levels of the thermogenic adipocyte markers in control mice, such induction was strongly attenuated when PRDM16 was absent (**Figure 3.1 A**).

The same pattern was also observed at the protein level for key thermogenic adipocyte markers such as UCP1 (**Figure 3.1 B-C**). Consistently, UCP1+ beige adipocytes failed to arise in the inguinal and dorsomedial regions following cold exposure in c*Prdm16*^{KO} (**Figure 3.1 D-K**). These results strongly support c*Prdm16*^{KO} as a valid model for studying the role of beige adipocytes in establishing sympathetic innervation.

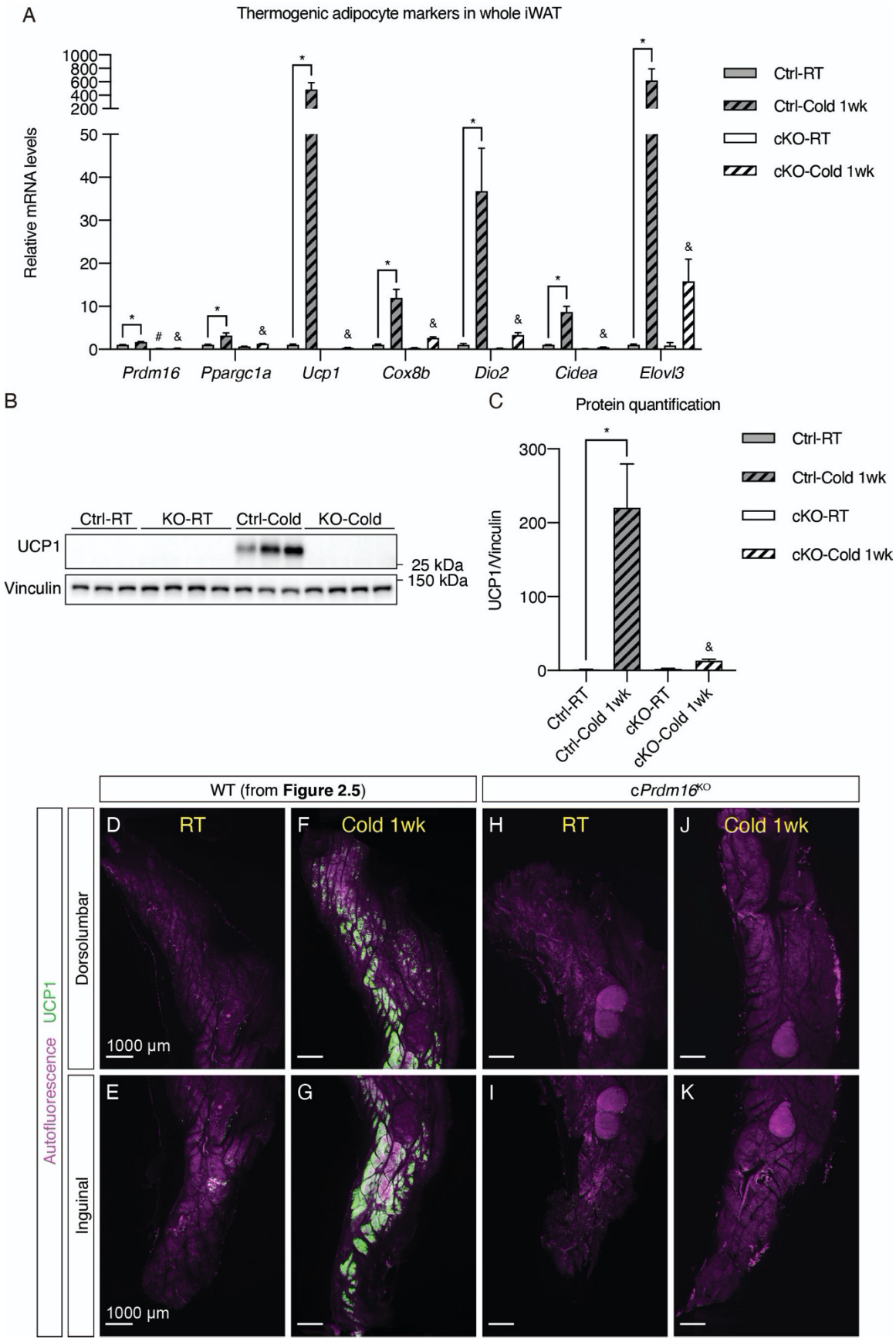
A
Thermogenic adipocyte markers in whole iWAT
Relative mRNA levels
Ctrl-RT
Ctrl-Cold 1wk
cKO-RT
cKO-Cold 1wk
Prdm16
Ppargc1a
Ucp1
Cox8b
Dio2
Cidea
Elovl3
B
Ctrl-RT
KO-RT
Ctrl-Cold
KO-Cold
UCP1
Vinculin
25 kDa
150 kDa
C
Protein quantification
UCP1/Vinculin
Ctrl-RT
Ctrl-Cold 1wk
cKO-RT
cKO-Cold 1wk
WT (from Figure 2.5)
cPrdm16KO
Autofluorescence UCP1
Dorsolumbar
Inguinal
D RT
F Cold 1wk
H RT
J Cold 1wk
E
G
I
K
1000 µm

Figure 3.1 Validation of constitutive *Prdm16*^{KO} mouse model.
Constitutive *Prdm16*^{KO} (cKO) and littermate control mice aged between 7-8 weeks were housed at RT or 8°C for 1 week, n=4-5. Whole iWAT samples were collected for molecular analysis. (**A**) Normalized gene expression. (**B**) Western blots of UCP1 and vinculin (loading control). (**C**) Quantification of UCP1 with normalization to vinculin. Molecular weights are indicated as kDa. (**A and C**) Data are normalized to control RT group, presented as mean + SEM, and analyzed by two-way ANOVA followed by Bonferroni's multiple comparisons test. * denotes $p<0.05$ RT- vs. cold-exposed control samples. # denotes $p<0.05$ cKO vs. control samples at RT. & denotes cKO vs. control samples at cold. (**D-K**) Representative maximum intensity projections of 20 μm z-stacks from iWAT samples collected from 7-8-week-old WT and c*Prdm16*^{KO} mice exposed to either RT or 8°C for 1 week. Tissue autofluorescence (magenta) and UCP1 (green) are shown. (**D-E**) WT RT. (**F-G**) WT cold 1 week. (**H-I**) c*Prdm16*^{KO} RT. (**J-K**) c*Prdm16*^{KO} cold 1 week. (**D, F, H, and J**) Images of the dorsolumbar region. (**E, G, I, and K**) Images of the inguinal region. Images presented in **D-G** are from the same samples shown in **Figure 2.5**. Scale bars are indicated.

We next carefully compared the sympathetic structures in c*Prdm16*^{KO} and control mice by whole-tissue imaging. Grossly, iWAT from a c*Prdm16*^{KO} mouse housed at RT showed no obvious differences in large features such as nerve bundles or blood vessel innervation as shown in maximum intensity projections (**Figure 3.2 E-F vs. A-B**) or thin sections with low-magnification (**Figure 3.2 G-H vs. C-D**). However, from high-magnification optical sections, we observed a reduction in parenchymal neurite projections to the inguinal region in the c*Prdm16*^{KO} sample (**Figure 3.2 M**), as compared to that from the WT sample (**Figure 3.2 I**). On the other hand, the innervation levels of the dorsolateral regions remained sparse regardless of the genotype (**Figure 3.2 O vs. K**).

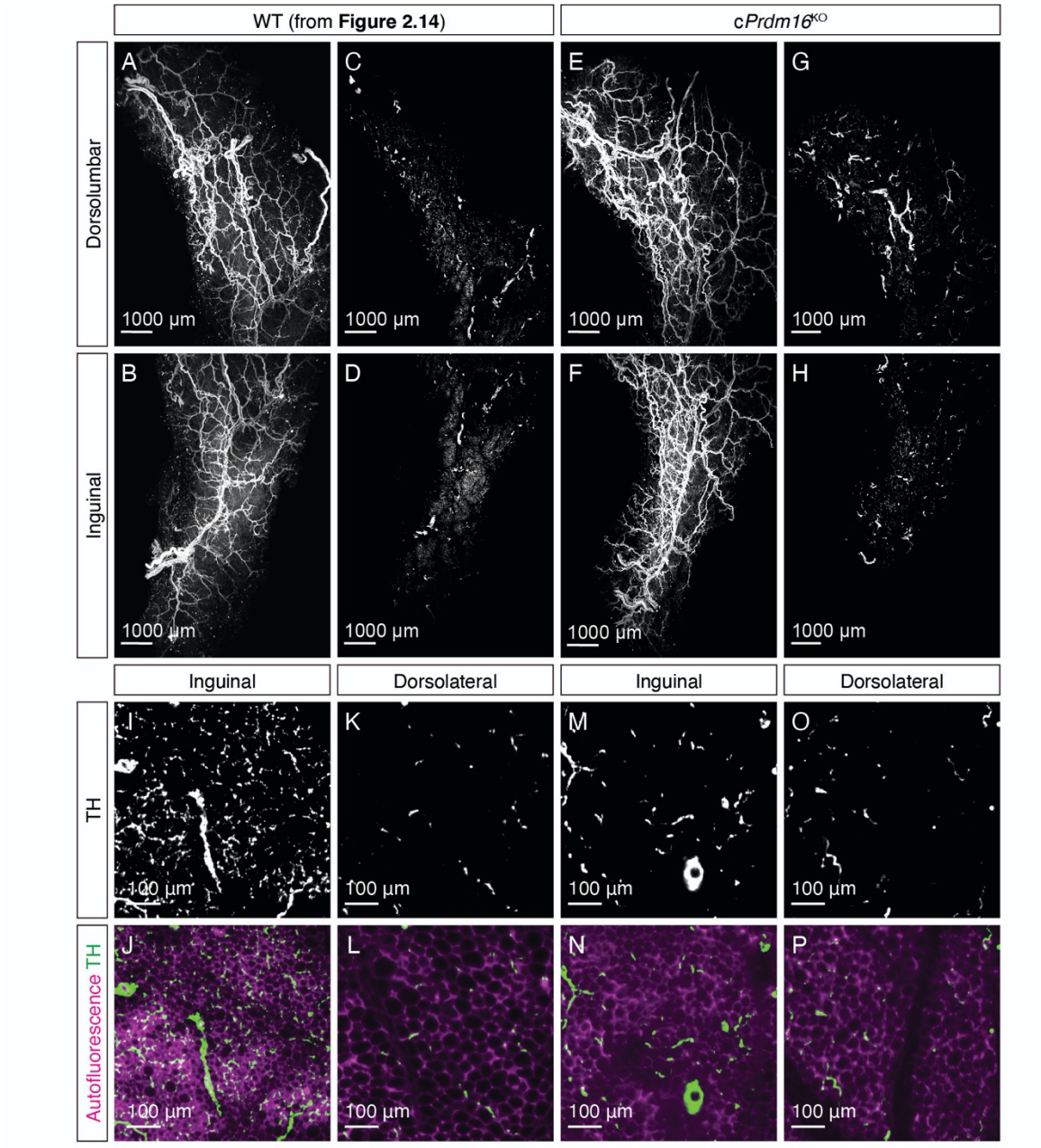
WT (from Figure 2.14)
cPrdm16KO
Dorsolumbar
Inguinal
A
B
C
D
E
F
G
H
1000 µm
Inguinal
Dorsolateral
Inguinal
Dorsolateral
TH
Autofluorescence TH
I
J
K
L
M
N
O
P
100 µm
Q
Inguinal
Dorsolateral
Neurite density
(normalized to volume)
Neurite length / volume
(µm/µm3)
0.005
0.004
0.003
0.002
0.001
0.000
####
****
WT
cKO
R
Inguinal
Dorsolateral
Adipocyte size
Mean adipocyte area (µm2)
1500
1000
500
0
%%%%
####
****
&
WT
cKO
S
Inguinal
Dorsolateral
Neurite density
(normalized to cell number)
Neurite length / adipocyte density
(arbitrary unit)
60
40
20
0
####
****
WT
cKO

Figure 3.2 Sympathetic innervation of iWAT from control and c*Prdm16*^{KO} mice.
(**A-B and E-F**) Maximum intensity projections of the entire z-stacks and (**C-D and G-H**) representative maximum intensity projections of 20 μm z-stacks from the same iWAT samples shown in **Figure 3.1 D-E and H-I**. TH channel is presented. (**A-D**) WT RT. (**E-H**) c*Prdm16*^{KO} RT. (**A, C, E, and G**) Images of the dorsolumbar region. (**B, D, F, and H**) Images of the inguinal region. (**I-P**) Representative optical sections with high magnification. (**I-J**) Inguinal region of WT. (**K-L**) Dorsolateral region of WT. (**M-N**) Inguinal region of c*Prdm16*^{KO}. (**O-P**) Dorsolateral region of c*Prdm16*^{KO}. (**I, K, M, and O**) TH channel. (**J, L, N, and P**) Overlay of TH (green) and autofluorescence (magenta). Scale bars are indicated. (**Q-S**) Quantification of sympathetic parenchymal neurite density and adipocyte size in the inguinal and the dorsolateral regions from WT and c*Prdm16*^{KO} mice. (**Q**) Total neurite length normalized to regional volume. (**R**) Mean adipocyte area. (**S**) Total neurite length normalized to adipocyte density. Individual data points are plotted with mean ± SEM and analyzed by two-way ANOVA followed by Bonferroni's multiple comparisons test. **** denotes $p<0.0001$ inguinal vs. dorsolateral in WT samples. #### denotes $p<0.0001$ inguinal regions of WT vs. cKO samples. & denotes $p<0.05$ inguinal vs. dorsolateral in cKO samples. %%%% denotes $p<0.0001$ dorsolateral regions of WT vs. cKO samples.

To quantitatively assess differences in parenchymal neurite density from the 3D images, we computationally traced and measured the parenchymal neurite lengths in randomly selected tissue volumes contained within lobules in the inguinal and the dorsolateral regions of iWAT (see **Chapter 5.3** for details). When total neurite lengths were normalized to volumes of the sampled regions, the 3-fold regional difference in parenchymal neurite density between the inguinal and the dorsolateral regions in WT sample was absent in c*Prdm16*^{KO} (**Figure 3.2 Q**). In addition, the inguinal region of c*Prdm16*^{KO} exhibited a 3-fold reduction in parenchymal neurite density relative to the same region in WT (**Figure 3.2 Q**). Interestingly, adipocytes in iWAT of c*Prdm16*^{KO} appeared larger as outlined by the tissue autofluorescence signal (**Figure 3.2 N and P vs. J and L**). Quantification of adipocyte area revealed that adipocytes in c*Prdm16*^{KO} were more than 2-fold larger in area than those in WT (**Figure 3.2 R**). It is possible that the decreased neurite density in c*Prdm16*^{KO} was due to a simple scaling effect; that is, the neurites appear sparser because the adipocytes are larger in size. To rule out this possibility, we also calculated neurite density by factoring in adipocyte density from each tissue volume (see **Chapter 5.3** for details), and still observed the lack of regionality following deletion of *Prdm16* (**Figure 3.2 S**).

Overall, we observed that the prominent regional difference between inguinal and dorsolateral regions in wild-type iWAT was absent following deletion of PRDM16 in fat cells. These data indicate that PRDM16 in adipocytes regulates regional neurite projections to adipose tissue, suggesting there is a PRDM16-dependent program by which adipocytes signal to neurons.

3.3 Timing of beige adipocyte-regulated sympathetic patterning

As neural projections and circuits can be regulated during development and by physiological stimuli in adult animals (Glebova and Ginty, 2005; Holtmaat and Svoboda, 2009), it is important to determine when the sympathetic innervation surrounding beige adipocytes is established. Using 3D whole-tissue imaging, we have begun to decipher the timing of when the interactions between sympathetic neurites and beige adipocytes in iWAT occur.

3.3.1 Development of parenchymal sympathetic neurites in mouse subcutaneous fat

To better understand adipocyte-sympathetic neurite interactions, we investigated whether the association between beige adipocytes and dense sympathetic innervation is developmentally determined. We first mapped the developmental timing of the sympathetic nervous system in iWAT using Adipo-Clear coupled with light sheet fluorescent imaging. Given that iWAT undergoes active tissue morphogenesis during late embryonic and early postnatal stages (Wang et al., 2013), we first performed whole tissue immunostaining and imaging in iWAT isolated from postnatal day (P) 6 mice using antibodies targeting TH to visualize the sympathetic network and CD31 to label vasculature.

Distinct features of sympathetic innervation in iWAT were observed at P6: a) travelling in parallel within nerve fascicles and b) wrapping around main blood vessels in a dense mesh-like morphology (**Figure 3.3 A-B**). Upon further analyzing the innervation pattern across the entire tissue, we observed that these structures were all interconnected to form a continuous sympathetic network. Specifically, we found several convergence points where TH+ nerve fibers within a nerve fascicle deviated from the bundle and merged with the innervation of the central blood vessel

(**Figure 3.3 A-B**), suggesting that sympathetic fibers leave the nerve fascicle and wrap around the main blood vessel as the first order of innervation. Subsequently, the main blood vessel innervation extended around branching arterioles and venules as the second order of innervation (**Figure 3.3 C**). Lastly, discrete nerve fibers became apparent at the terminals of the second order innervation to project into tissue parenchyma, where adipocytes are located. Notably, the majority of these nerve fibers appeared to follow capillaries to arrive in the tissue parenchyma (**Figure 3.3 D-E**).

Although nerve endings were visible in the tissue parenchyma at P6, we did not observe any extensive innervation surrounding adipocytes that resemble the dense parenchymal innervation in adult iWAT (**Figure 2.10 B**). In addition, both the dorsolumbar and inguinal regions of iWAT showed similar innervation patterns at this stage (**Figure 3.4 A-C**). The results from P6 mice indicate that the sympathetic axons in iWAT first grow along the vasculature before reaching the tissue parenchyma, consistent with previous findings showing that developing sympathetic axons follow the vasculature to reach their target organs (Glebova and Ginty, 2005).

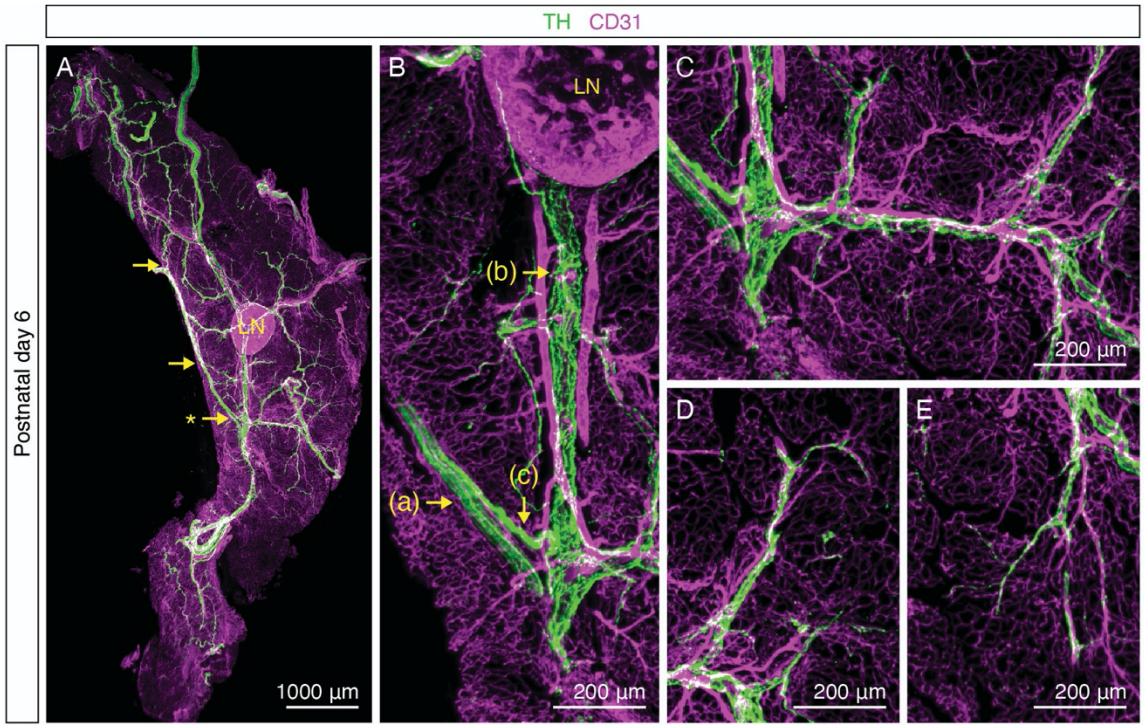

Figure 3.3 Organization of sympathetic nervous system in iWAT at P6.
Representative images of iWAT from a P6 C57BL6/J male mouse immunolabeled with TH (green) and CD31 (magenta). (**A**) Maximum intensity projection from a 1000 µm z-stack. Arrows indicate convergence points where nerve fibers deviate from nerve bundles to establish blood vessel innervation. (**B**) High-magnification image of the indicated (*) convergence point in (**A**). Arrows indicate distinct features of sympathetic innervation in iWAT: (a) nerve fascicle, (b) blood vessel innervation, (c) a nerve fiber departing from a nerve fascicle to join blood vessel innervation. (**C**) High-magnification image showing sympathetic innervation from main blood vessel extending to arterioles or venules. (**D-E**) High-magnification images showing discrete nerve endings project into tissue parenchyma.

Remarkably, adipocyte-innervating neurites became apparent four days later. In the inguinal region, dense parenchymal neurites surrounding adipocytes were first found at P10, in particular within lobules at the core of this region (**Figure 3.4 E**). At P14, the number of lobules that contain dense parenchymal neurites dramatically increased, spreading outwards from the core of the inguinal region (**Figure 3.4 G**). From P21 and onwards, more inguinal lobules were found to harbor dense parenchymal innervation (**Figure 3.4 I and K**), with the pattern comparable to that of adult iWAT (**Figure 2.10 B**). Interestingly, the emergence of dense parenchymal neurites in the dorsomedial region lagged behind (**Figure 3.4 B, D, F, H, and J**). While parenchymal neurites were detectable in the dorsomedial region at P14 and P21 (**Figure 3.4 F and H**), we did not observe densely innervated lobules in this region until P28 (**Figure 3.4 J**). Notably, the dorsolateral region of iWAT remained sparsely innervated relative to the inguinal region and the dorsomedial region throughout the early postnatal period (**Figure 3.4 B, D, F, H, and J**).

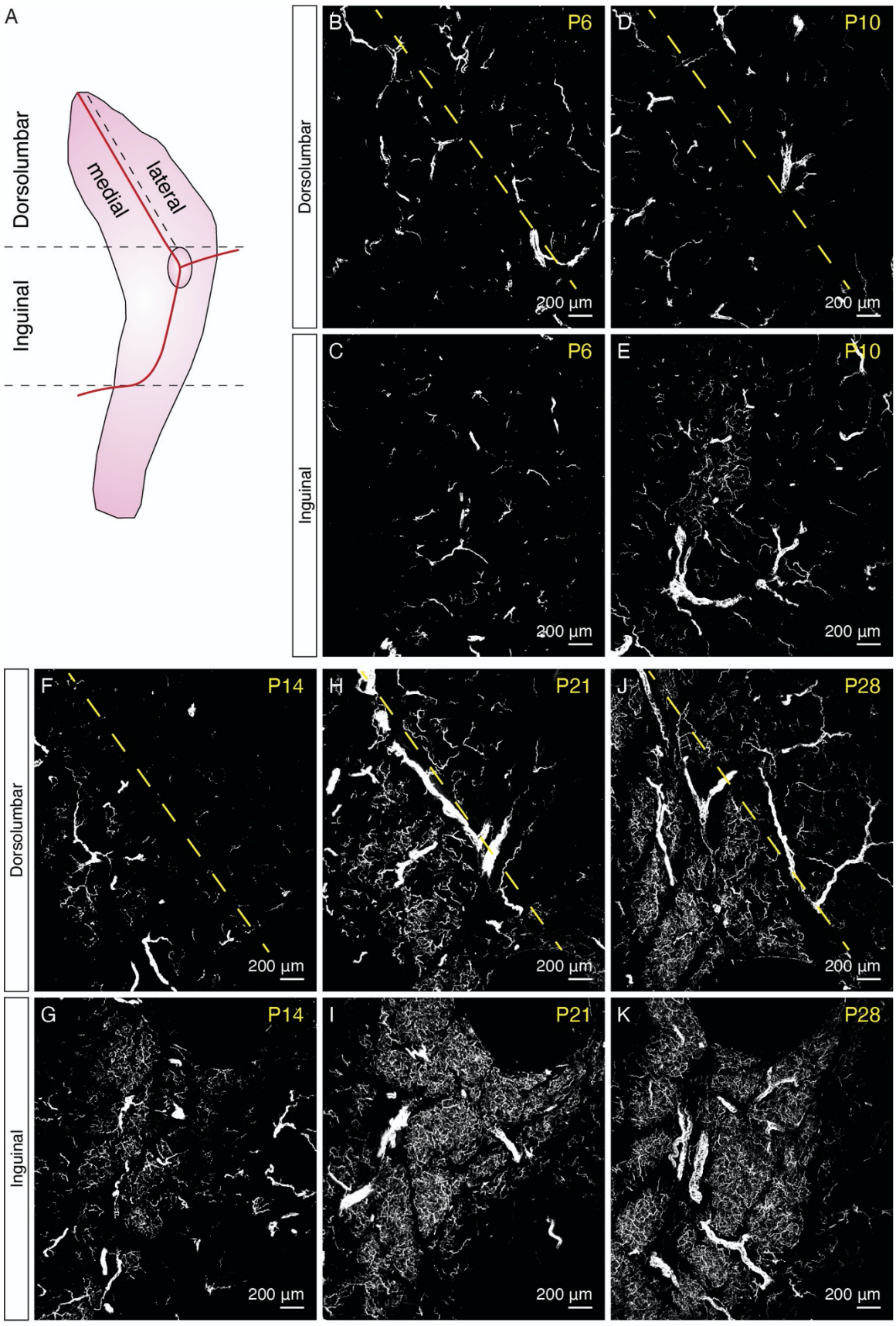
A
Dorsolumbar
Inguinal
medial
lateral
B
P6
200 µm
D
P10
200 µm
C
P6
200 µm
E
P10
200 µm
F
P14
200 µm
H
P21
200 µm
J
P28
200 µm
G
P14
200 µm
I
P21
200 µm
K
P28
200 µm

Figure 3.4 Development of sympathetic parenchymal innervation in iWAT.
(**A**) Schematic illustration of the anatomy of iWAT. (**B-K**) Representative whole-tissue images of iWAT immunolabeled with TH from (**B-C**) P6, (**D-E**) P10, (**F-G**) P14, (**H-I**) P21, and (**J-K**) P28 C57BL6/J male mice born and housed at room temperature. Maximum intensity projections from 50 μm z-stacks are shown. (**B, D, F, H, and J**) Images of the dorsolumbar region. Yellow dashed lines indicate the boundaries between the dorsomedial (left) and dorsolateral (right) regions. (**C, E, G, I, and K**) Images of the inguinal region. Scale bars are indicated.

3.3.2 UCP1+ beige adipocytes and dense sympathetic parenchymal innervation emerge together during early postnatal development

As our previous findings suggest that beige adipocytes interact with sympathetic projections and modulate the density of sympathetic parenchymal innervation (Chi et al., 2018a), we next investigated whether early postnatal development of sympathetic innervation may also be regulated by beige adipocytes. We analyzed the localization of beige adipocytes using an antibody against UCP1 and compared their distribution in relation to the sympathetic parenchymal innervation in iWAT using whole-tissue imaging. As expected, we observed a strong association between beige adipocytes and parenchymal innervation, even during early postnatal development (**Figure 3.5**).

Specifically, we found that beige adipocytes first emerge in iWAT of P6 animals that were born and housed at room temperature, as shown by a few UCP1+ adipocytes sparsely distributed in the core of the inguinal region, close to the inguinal lymph node (**Figure 3.5 B**). At P10, we detected clusters of UCP1+ adipocytes located in distinct lobules in the core of the inguinal region (**Figure 3.5 D**). Four days later, at P14, the lobules containing UCP1+ adipocytes further expanded from the core (**Figure 3.5 F**). At P21 and P28, extensive UCP1+ lobules occupied a significant portion of the inguinal region, comparable to the extent of UCP1+ cells only seen in adult animals after cold exposure (**Figure 3.5 H and J**). On the other hand, the emergence of UCP1+ adipocytes in the dorsolumbar region again lagged behind. UCP1+ adipocytes in the dorsomedial region first emerged in small clusters at P14 and then as distinct lobules at P21 (**Figure 3.5 A, C, E, and G**). At P28, the same region contained a large number of lobules harboring UCP1+ adipocytes (**Figure 3.5 I**). Interestingly, the dorsolateral region was devoid of UCP1+ adipocytes at all stages analyzed (**Figure 3.5 A, C, E, and G**).

When we overlaid the UCP1 and TH signals, we observed a dramatic overlap between the presence of dense parenchymal innervation and clusters of beige adipocytes, particularly from P10 onwards (**Figure 3.5 A-J**). To better observe the relationship between TH+ neurites and adipocytes, we performed confocal microscopy on iWAT of P14 mice, a key time point when both UCP1+ adipocytes and sympathetic parenchymal neurites are actively developing. Assisted by high-resolution images, we observed that UCP1+ adipocytes were surrounded by dense TH+ neurite arbors, while UCP1- adipocytes highlighted by tissue autofluorescence largely remained uninnervated (**Figure 3.5 K-N**). These results strongly suggest that early postnatal beige adipocytes are associated with the signals enabling sympathetic axon growth.

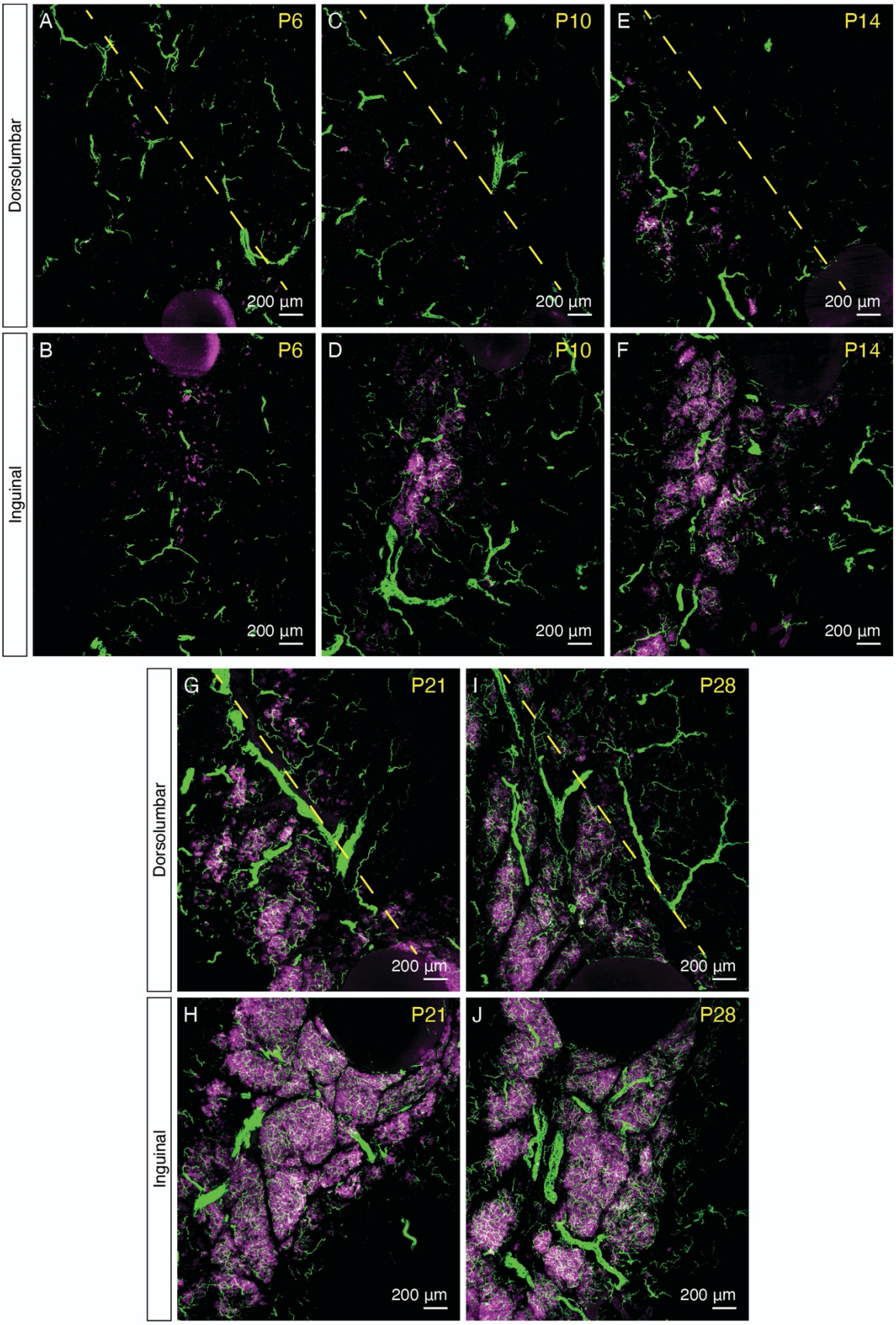
Dorsolumbar
Inguinal
A
P6
B
P6
C
P10
D
P10
E
P14
F
P14
G
P21
H
P21
I
P28
J
P28
200 µm

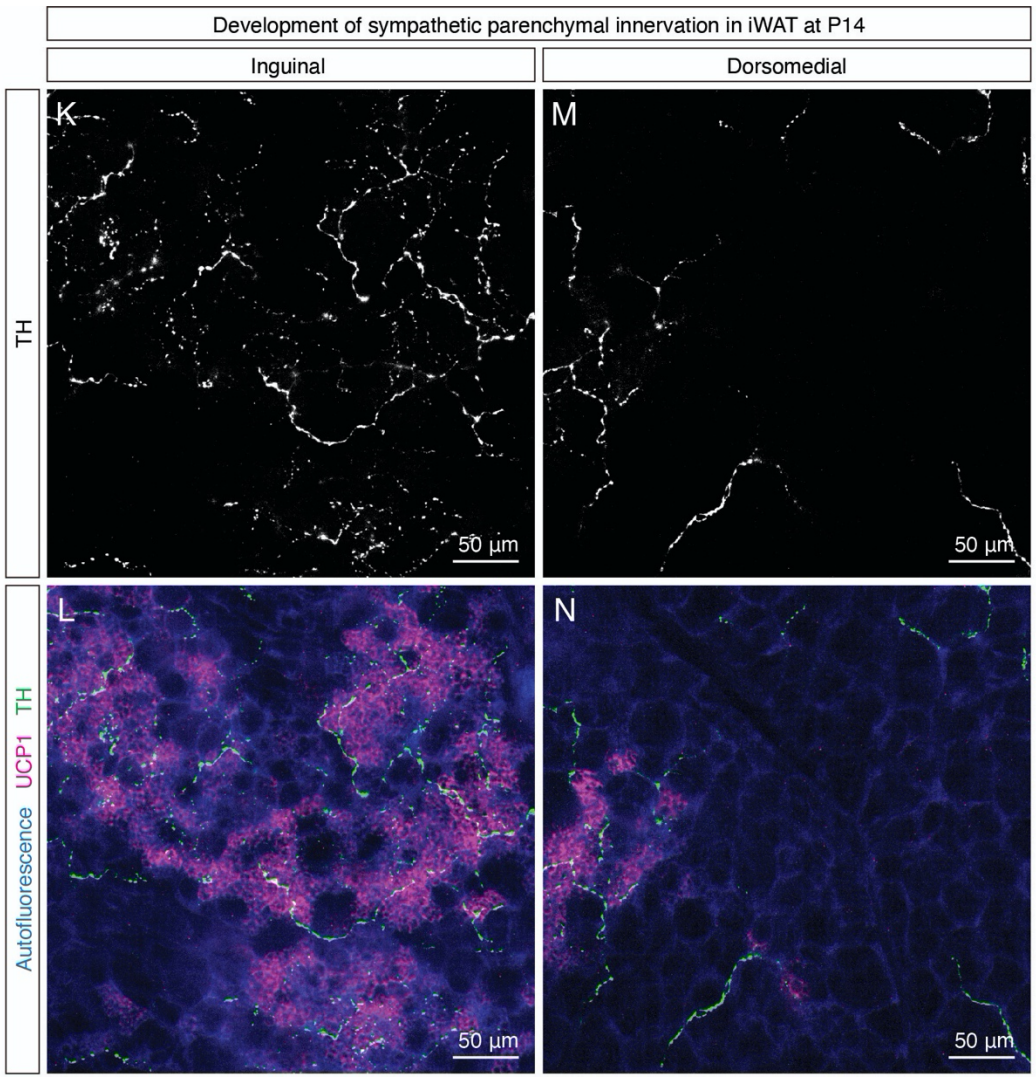

Figure 3.5 UCP1+ beige adipocytes and dense sympathetic parenchymal innervation emerge together during early postnatal development.

Representative MIPs of 50 µm z-stacks from iWAT immunolabeled with TH (green) and UCP1 (magenta) of (**A-B**) P6, (**C-D**) P10, (**E-F**) P14, (**G-H**) P21, and (**I-J**) P28 C57BL6/J male mice born and housed at room temperature, corresponding to **Figure 3.4 B-K**. (**A, C, E, G, and I**) Images of the dorsolumbar region. Yellow dashed lines indicate the boundaries between the dorsomedial (left) and dorsolateral (right) regions. (**B, D, F, H, and J**) Images of the inguinal region. (**K-N**) Confocal imaging of an iWAT from P14. MIPs of 20 µm z-stacks are shown. (**K and M**) TH channel. (**L and N**) Overlay of tissue autofluorescence (blue), UCP1 (magenta), and TH (green). (**K-L**) Representative images of the inguinal region. (**M-N**) Representative images of the dorsomedial region. Scale bars are indicated.

3.3.3 *Prdm16* regulates the emergence of early postnatal beige adipocytes and dense sympathetic parenchymal innervation

As PRDM16 controls development and function of cold-induced beige adipocytes during adulthood, we next examined whether PRDM16 is also important for the formation of early postnatal beige adipocytes and their associated dense sympathetic innervation. We analyzed iWAT of adipocyte-specific *Prdm16* knockout mice (c*Prdm16*^{KO} mice) at postnatal days 6, 14, and 21, which are key time points in the course of beige adipocyte and sympathetic innervation development.

At P6, we observed minimal beige adipocytes and scant parenchymal innervation in both control and c*Prdm16*^{KO} mice (**Figure 3.6 A-D and A'-D'**), suggesting that the sympathetic nervous system develops similarly in both models prior to the emergence of beige adipocyte clusters. At P14, the deletion of *Prdm16* completely ablated UCP1+ adipocytes that normally arise in the inguinal region of control mice (**Figure 3.6 E-H**). Correspondingly, the increase seen in parenchymal innervation density in the inguinal region of control mice was not observed in c*Prdm16*^{KO} mice (**Figure 3.6 E-H and E'-H'**). At P21, we observed similar ablation of UCP1+ adipocytes and lack of growth in parenchymal innervation in c*Prdm16*^{KO} relative to control samples (**Figure 3.6 I-L and I'-L'**). These results indicate that early postnatal beige adipocytes indeed depend on PRDM16, the well-characterized transcriptional determinant of brown and beige adipocytes. Importantly, these data strongly suggest that sympathetic axon growth during early iWAT morphogenesis may be regulated by PRDM16-dependent signals from beige adipocytes or associated cell types.

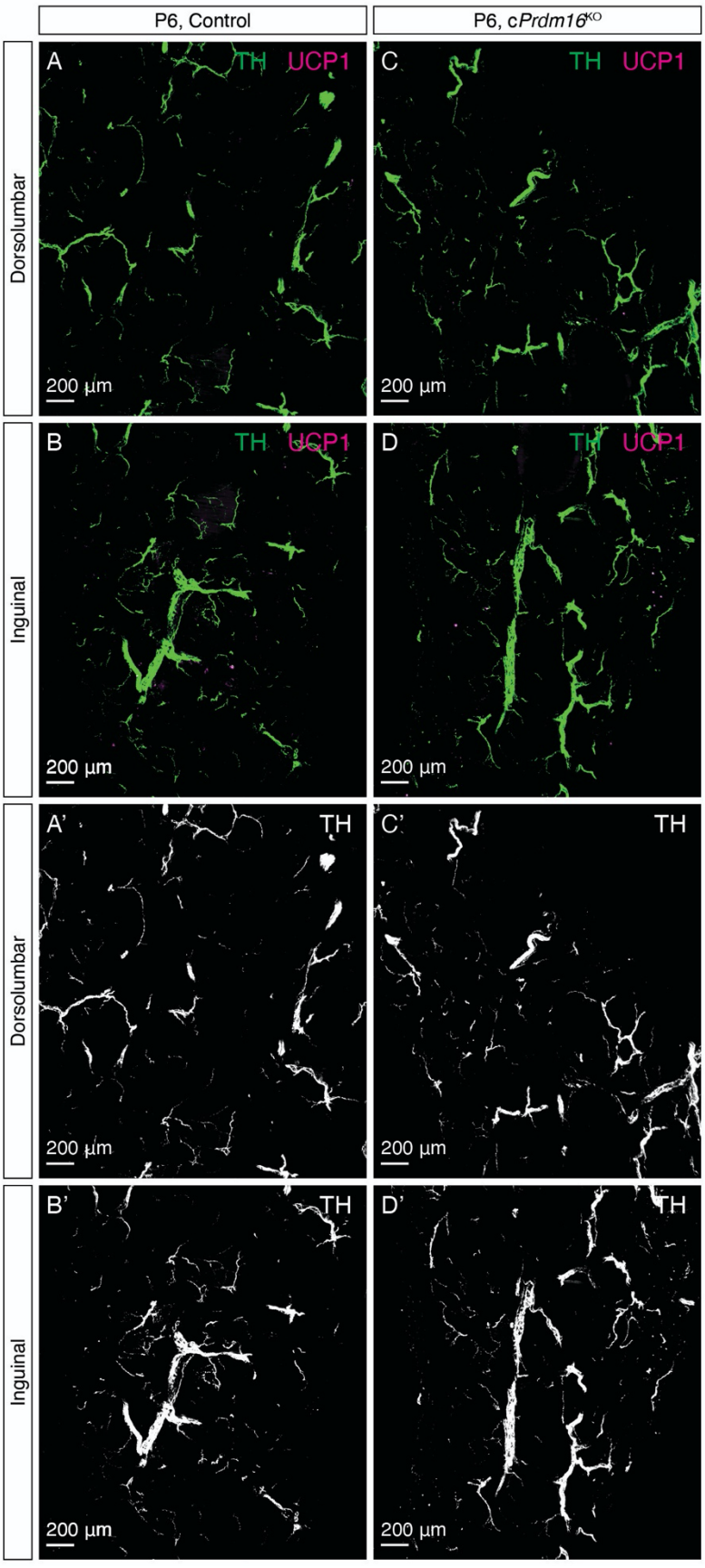
P6, Control
P6, cPrdm16KO
Dorsolumbar
Inguinal
A
B
C
D
A'
B'
C'
D'
TH
UCP1
200 µm

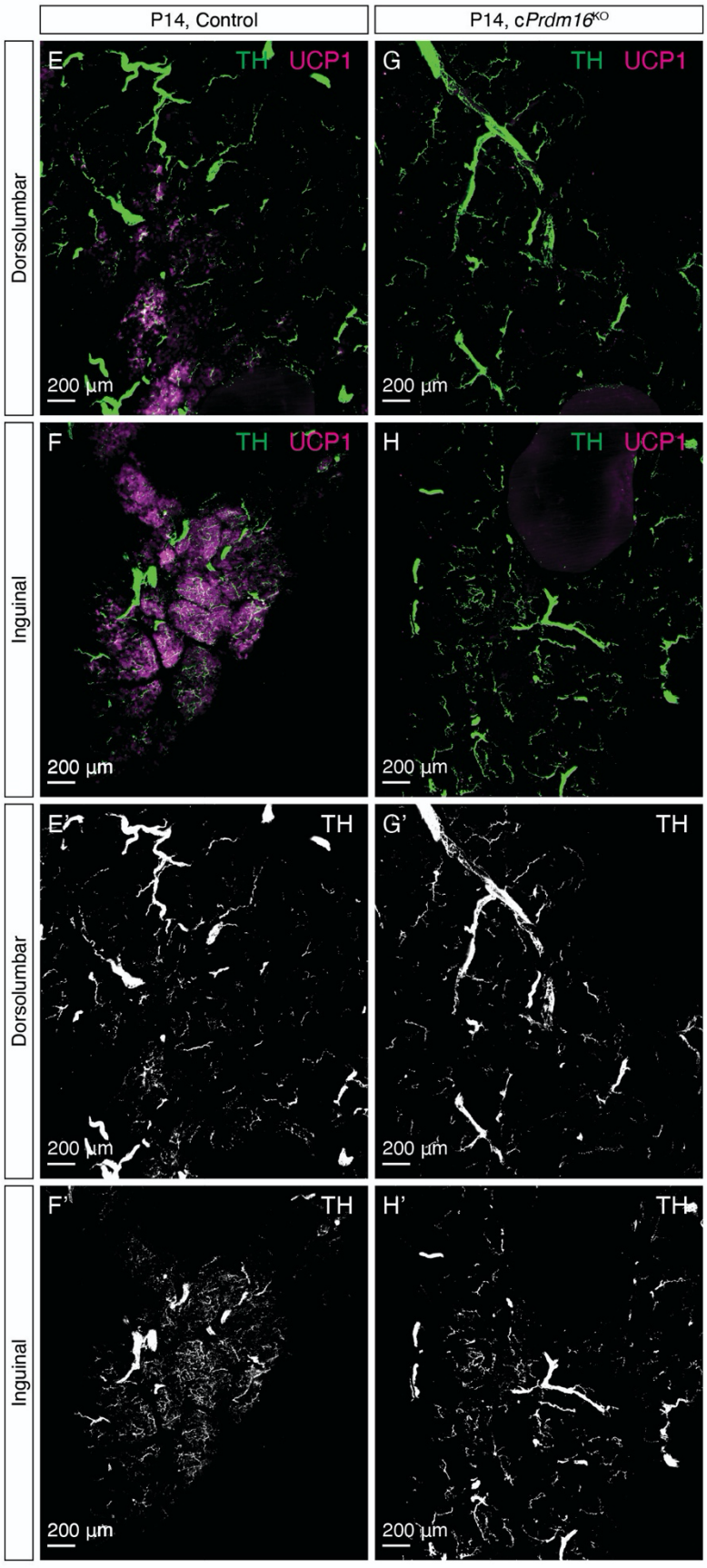
P14, Control
P14, cPrdm16KO
Dorsolumbar
Inguinal
Dorsolumbar
Inguinal
E
TH UCP1
G
TH UCP1
F
TH UCP1
H
TH UCP1
E'
TH
G'
TH
F'
TH
H'
TH
200 µm

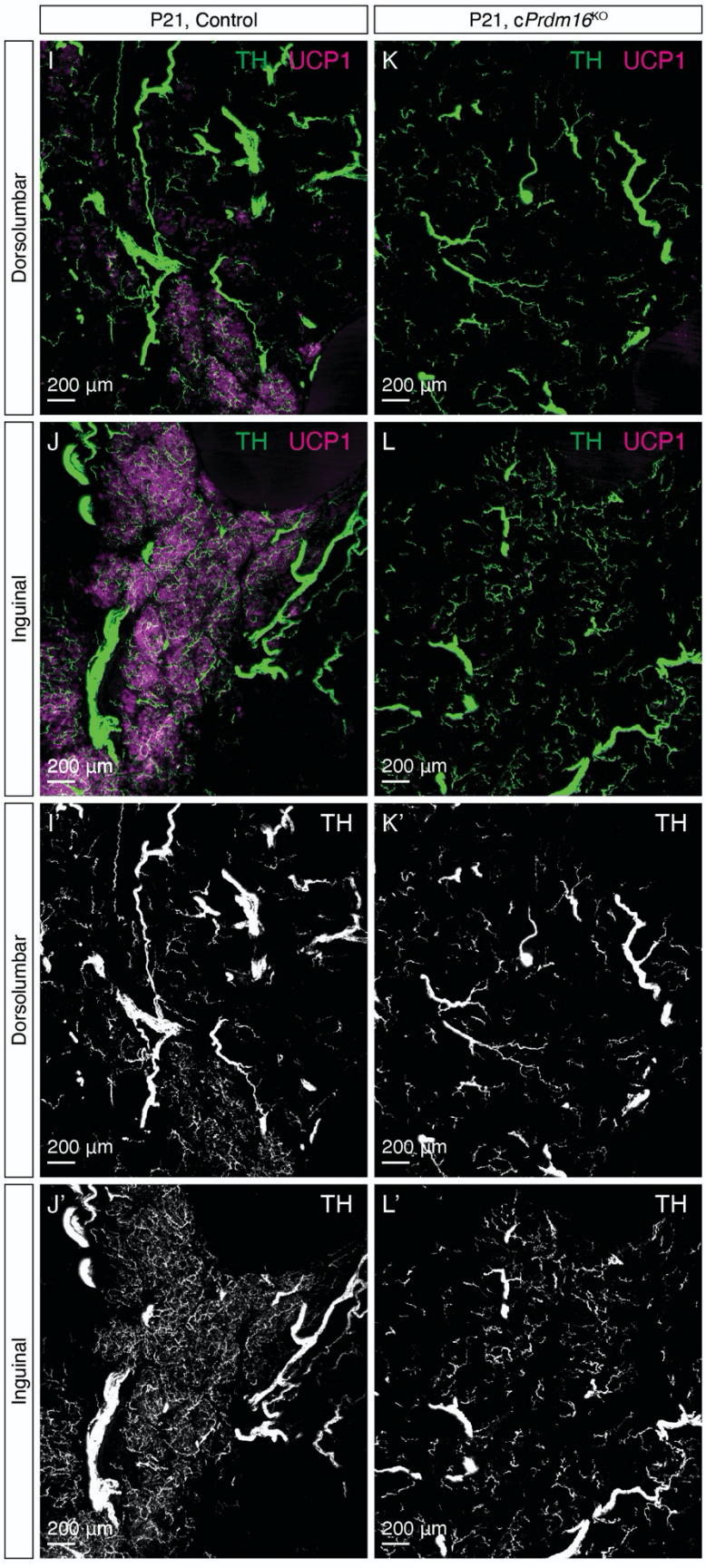
P21, Control
P21, cPrdm16KO
Dorsolumbar
Inguinal
Dorsolumbar
Inguinal
I
TH UCP1
200 µm
K
TH UCP1
200 µm
J
TH UCP1
200 µm
L
TH UCP1
200 µm
I'
TH
200 µm
K'
TH
200 µm
J'
TH
200 µm
L'
TH
200 µm

Figure 3.6 PRDM16 regulates the emergence of early postnatal beige adipocytes and dense sympathetic parenchymal innervation.
(**A-D**) Representative maximum intensity projections of 50 μm z-stacks from iWAT immunolabeled with TH (green) and UCP1 (magenta) from (**A-B**) control and (**C-D**) c*Prdm16*^{KO} mice at P6. (**A'-D'**) Images showing TH signals only, corresponding to (**A-D**). (**E-H**) Representative maximum intensity projections of 50 μm z-stacks from iWAT immunolabeled with TH (green) and UCP1 (magenta) from (**E-F**) control and (**G-H**) c*Prdm16*^{KO} mice at P14. (**E'-H'**) Images showing TH signals only, corresponding to (**E-H**). (**I-L**) Representative maximum intensity projections of 50 μm z-stacks from iWAT immunolabeled with TH (green) and UCP1 (magenta) from (**I-J**) control and (**K-L**) c*Prdm16*^{KO} mice at P21. (**I'-L'**) Images showing TH signals only, corresponding to (**I-L**). (**A, A', C, C', E, E', G, G', I, I', K, and K'**) Images of the dorsolumbar region. (**B, B', D, D', F, F', H, H', J, J', L, and L'**) Images of the inguinal region. Scale bars are indicated.

3.3.4 Ablation of beige adipocyte function during early development causes decreased sympathetic parenchymal innervation

To further delineate the critical time window for sympathetic innervation patterning in iWAT, we generated an inducible mouse model to ablate beige adipocyte function (*Adipoq*^{rtTA}; *TRE-Cre*; *Prdm16*$^{lox/lox}$; hereafter noted as inducible *Prdm16*^{KO} or i*Prdm16*^{KO} mice), where *Prdm16* can be deleted in adipocytes in a doxycycline-dependent manner (**Figure 3.7 A**). To test whether sympathetic parenchymal innervation may be developmentally determined during a defined time window, doxycycline was delivered to mice from embryonic day (E) 14 until P21, the period of time when both beige adipocytes and parenchymal innervation development become clearly apparent. Following doxycycline treatment, i*Prdm16*^{KO} and littermate control mice were switched back to chow diet for two weeks and subsequently exposed to either room temperature (RT) or 8°C for two days (**Figure 3.7 B**).

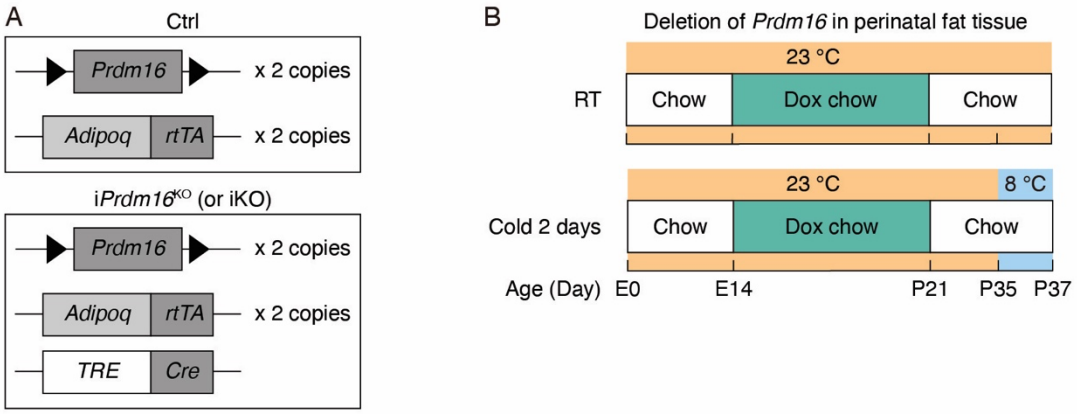

Figure 3.7 Inducible deletion of *Prdm16* in adipocytes.
(**A**) Schematic representation of the genetic components of the control and i*Prdm16*^{KO} mice. i*Prdm16*^{KO} mice carry floxed *Prdm16* alleles (*Prdm16*$^{lox/lox}$), two copies of *Adipoq*^{rtTA} transgene, and one copy of *TRE-Cre* transgene. Littermates carrying only *Prdm16*$^{lox/lox}$ and *Adipoq*^{rtTA} (i.e., Cre-) were used as the control animals. (**B**) Control (Cre-) and i*Prdm16*^{KO} (Cre+) mice housed at RT (23 °C) were kept on a doxycycline-containing chow diet from E14 until P21 before being switched to a regular chow diet for another two weeks. Control and i*Prdm16*^{KO} mice were either maintained at RT (23 °C) or exposed to cold (8 °C) for 2 days at P35.

We first confirmed that perinatal doxycycline treatment led to a strong reduction in *Prdm16* in adipose depots at the mRNA (70% reduction in the inguinal region of iWAT, 65% reduction in iBAT) and protein levels (**Figure 3.8 A-B**). Both i*Prdm16*^{KO} (perinatal deletion, 5wk-old) and littermate control mice developed similarly, with no difference in body mass (**Figure 3.8 C**). To examine whether the perinatal deletion of *Prdm16* led to ablation of beige adipocyte function, we analyzed mRNA levels of thermogenic adipocyte markers that are upregulated in wild-type cold-induced beige adipocytes. Since we have consistently observed that the inguinal region of iWAT is enriched in both early postnatal and cold-inducible beige adipocytes (**Figure 2.5** and **Figure 3.5**), we hereafter focused on analyzing changes in the inguinal region. As expected, the control inguinal regions exhibited robust increases in the entire panel of thermogenic adipocyte markers following 2 days of cold exposure (e.g., 35-fold induction in *Ucp1*) (**Figure 3.8 E**). In contrast, the cold-induced increases were almost completely blocked following perinatal deletion of *Prdm16* (**Figure 3.8 E**), mirroring our previous findings in constitutive *Prdm16*^{KO} mice (Cohen et al., 2014). On the other hand, the transient *Prdm16* deletion did not significantly alter adipocyte differentiation or function, as shown by *Pparg*, *Fabp4*, and *Adipoq* mRNA levels (**Figure 3.8 D**), suggesting that *Prdm16* deletion removed adipocytes' ability to become thermogenic but did not alter their maturation levels. Taken together, perinatal treatment with doxycycline achieved robust adipocyte-specific deletion of *Prdm16* and subsequently blocked cold-induced thermogenic gene expression in i*Prdm16*^{KO} mice (perinatal deletion, 5wk-old), confirming that this is a valid model for studying the importance of early postnatal beige adipocyte function.

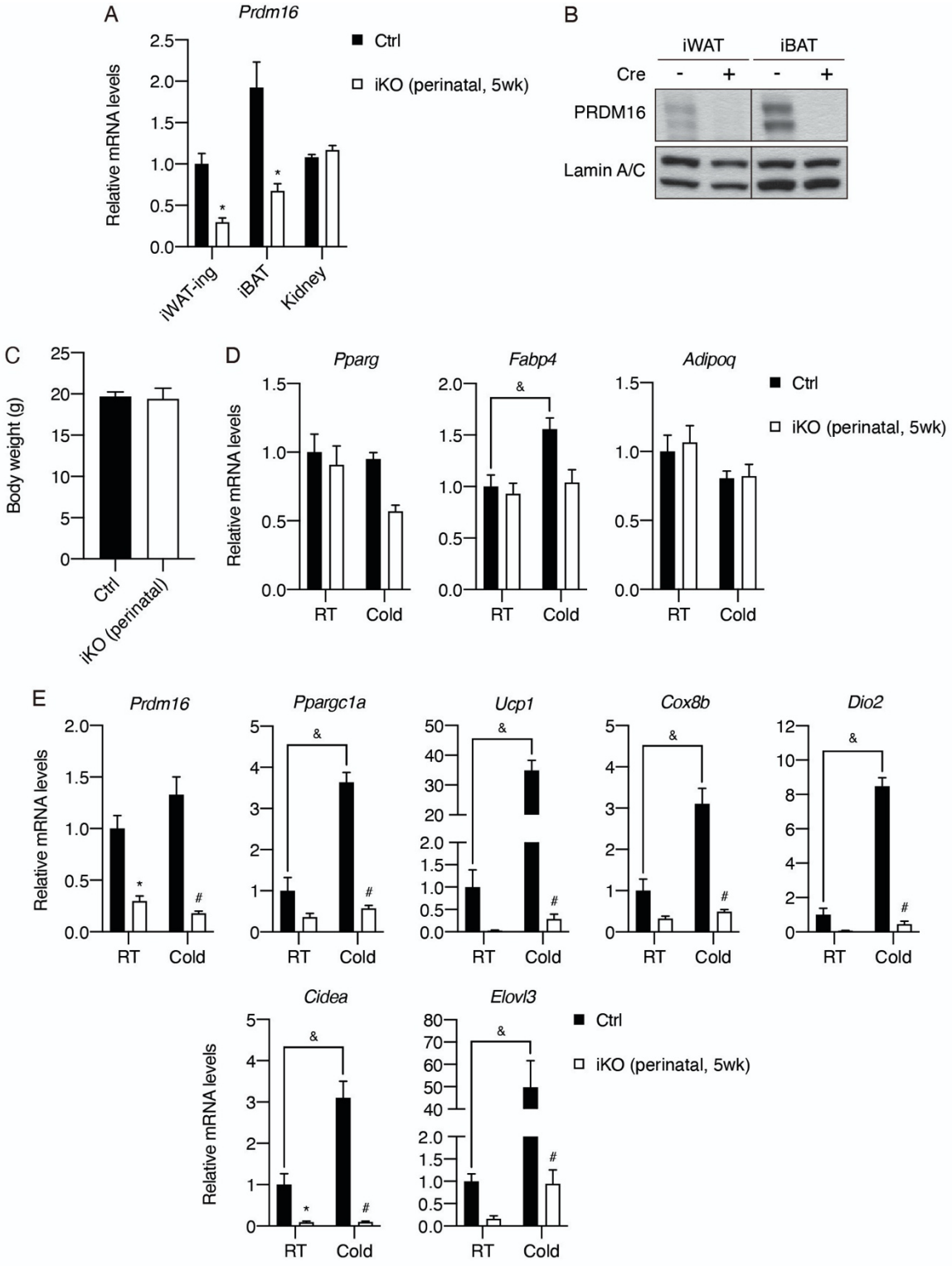
A
Prdm16
Relative mRNA levels
Ctrl
iKO (perinatal, 5wk)
iWAT-ing
iBAT
Kidney
B
iWAT
iBAT
Cre
PRDM16
Lamin A/C
C
Body weight (g)
Ctrl
iKO (perinatal)
D
Pparg
Fabp4
Adipoq
RT
Cold
E
Prdm16
Ppargc1a
Ucp1
Cox8b
Dio2
Cidea
Elovl3

Figure 3.8 Perinatal deletion of *Prdm16* blocks cold-induced thermogenic gene expression. (**A**) Normalized *Prdm16* mRNA expression of the indicated tissue types from control and i*Prdm16*^{KO} (perinatal deletion) mice maintained at RT, n=4-5. Data are presented as mean + SEM and analyzed by Student's t test. * denotes $p<0.05$ iKO (perinatal) vs. control samples for each tissue type. (**B**) Western blot of PRDM16 and lamin A/C from nuclear extracts of iWAT and iBAT of control (Cre-) and i*Prdm16*^{KO} (perinatal, 5wk-old) (Cre+) samples. (**C**) Body weights of control and i*Prdm16*^{KO} (perinatal, 5wk-old) mice before sacrifice. Data are presented as mean + SEM and analyzed by Student's t test. (**D-E**) Normalized gene expression of inguinal regions of iWAT from control and i*Prdm16*^{KO} (perinatal, 5wk-old) mice exposed to RT or cold for 2 days, n=3-5. (**D**) Representative genes involved in the adipogenic program and (**E**) enriched in thermogenic adipocytes. Data are normalized to control RT group, presented as mean + SEM, and analyzed by two-way ANOVA followed by Bonferroni's multiple comparisons test. * denotes $p<0.05$ iKO (perinatal) vs. control samples at RT. # denotes $p<0.05$ iKO (perinatal) vs. control samples at cold. & denotes $p<0.05$ cold- vs. RT-exposed control samples.

We next performed whole-tissue imaging on cleared iWAT of control and i*Prdm16*^{KO} (perinatal deletion, 5wk-old) to assess whether perinatal *Prdm16* deletion is sufficient to reproduce the innervation defect seen in c*Prdm16*^{KO}. While the gross features of sympathetic innervation such as nerve fascicles and blood vessel innervation were preserved in i*Prdm16*^{KO} (perinatal deletion, 5wk-old), the parenchymal innervation that localized to the inguinal region of control iWAT was dramatically reduced in i*Prdm16*^{KO} (perinatal deletion, 5wk-old) (**Figure 3.9 A-F**). We next assessed differences in parenchymal neurite density from 3D images by computational neurite tracing in randomly selected tissue volumes from the inguinal region of iWAT. When neurite lengths were normalized to volumes of the sampled regions, i*Prdm16*^{KO} (perinatal deletion, 5wk-old) samples showed a 74.5% reduction in parenchymal neurite density compared to control samples (**Figure 3.9 K**). Interestingly, we noticed that adipocytes in i*Prdm16*^{KO} (perinatal deletion, 5wk-old) samples also appeared larger in size as outlined by the tissue autofluorescence and vasculature signal (**Figure 3.9 G-J**). To rule out a scaling effect caused by changes in adipocyte size, we also calculated neurite density by factoring in adipocyte density from each tissue volume, and still observed a significant 52.8% decrease in density following perinatal *Prdm16* deletion (**Figure 3.9 L**).

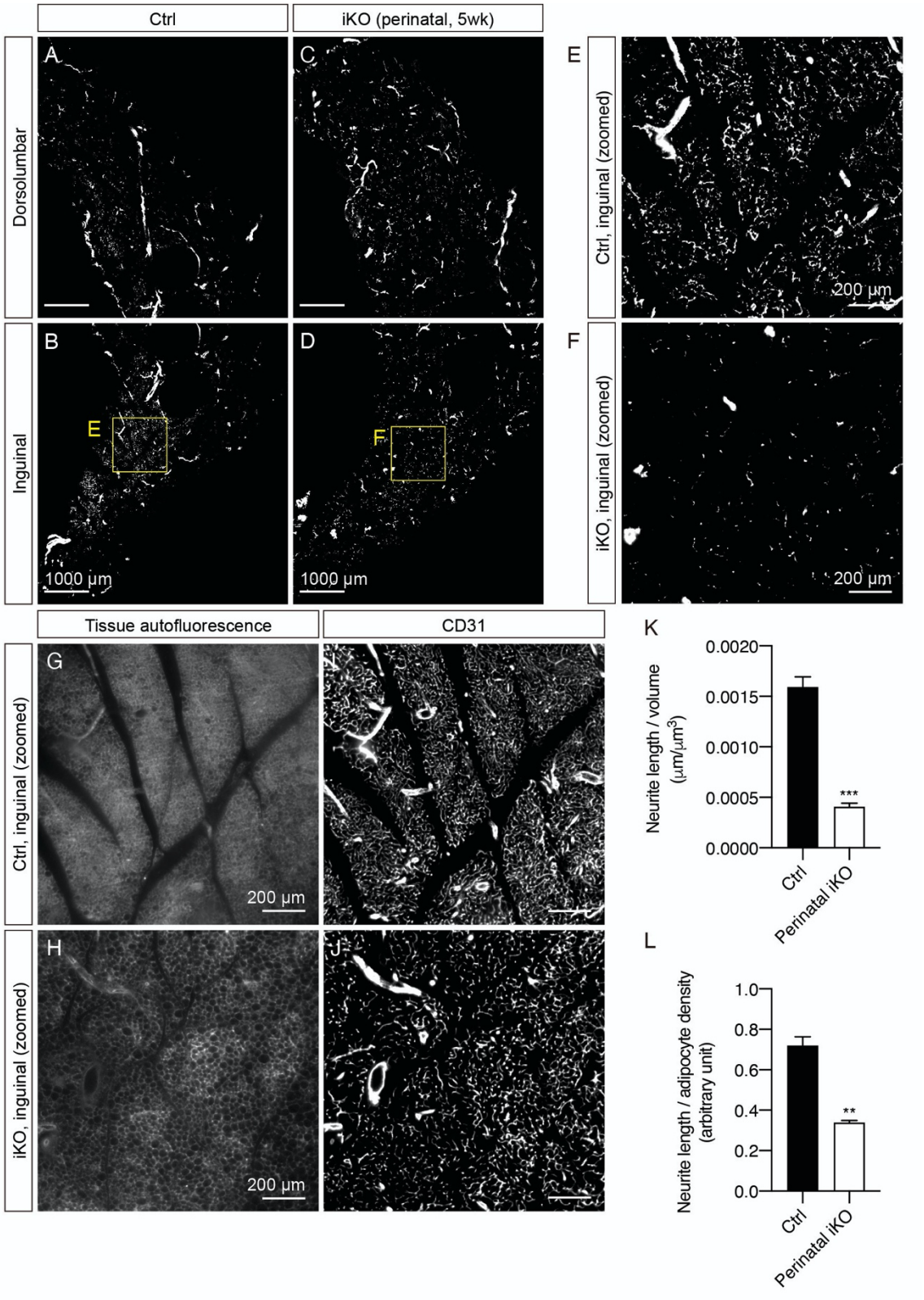
Ctrl
iKO (perinatal, 5wk)
Dorsolumbar
Inguinal
A
B
C
D
E
F
1000 μm
1000 μm
Ctrl, inguinal (zoomed)
iKO, inguinal (zoomed)
200 μm
200 μm
Tissue autofluorescence
CD31
G
H
I
J
200 μm
200 μm
K
Neurite length / volume (μm/μm³)
0.0020
0.0015
0.0010
0.0005
0.0000
***
Ctrl
Perinatal iKO
L
Neurite length / adipocyte density (arbitrary unit)
1.0
0.8
0.6
0.4
0.2
0.0
**
Ctrl
Perinatal iKO

Figure 3.9 Perinatal deletion of *Prdm16* causes decreased sympathetic parenchymal innervation.
(**A-D**) Representative low-magnification optical sections of iWAT from (**A-B**) control and (**C-D**) i*Prdm16*^{KO} (perinatal deletion, 5wk-old) mice maintained at RT. TH channel was presented. (**A and C**) Images of the dorsolumbar region. (**B and D**) Images of the inguinal region. (**E, G, and I**) High-magnification optical sections of the boxed region in **B**. (**F, H, and J**) High-magnification optical sections of the boxed region in **D**. (**E-F**) TH. (**G-H**) Tissue autofluorescence. (**I-J**) CD31. (**K and L**) Quantification of sympathetic parenchymal innervation in inguinal regions with total neurite length normalized to (**K**) regional volume or (**L**) adipocyte density. N=3 biological replicates per genotype were analyzed. Average neurite density from 5-7 randomly selected tissue volumes (technical replicates) contributes to neurite density measurement of one biological sample. Data are presented as mean + SEM and analyzed by Student's t test. ** and *** denote $p<0.01$ and $p<0.001$, respectively.

To assess whether the innervation defect following perinatal deletion of *Prdm16* may be rescued as animals age, we performed the same perinatal deletion of *Prdm16* but let animals reach 8 weeks of age on a chow diet, hereafter referred to as i*Prdm16*^{KO} (perinatal, 8wk-old) (**Figure 3.10 A**). As iWAT continues to expand in young adult mice, we reasoned that newly developed adipocytes during iWAT expansion might also affect sympathetic innervation. Consistent with the results from the i*Prdm16*^{KO} (perinatal, 5wk-old) experiment, we observed significantly reduced expression of *Prdm16* in i*Prdm16*^{KO} (perinatal, 8wk-old) relative to control (**Figure 3.10 B**). We also observed significantly blunted cold-induction in all thermogenic adipocyte markers in i*Prdm16*^{KO} (perinatal, 8wk-old) relative to control (**Figure 3.10 B**), while adipogenic markers remained unaltered (**Figure 3.10 C**). Importantly, TH+ fibers still appeared substantially sparser in i*Prdm16*^{KO} (perinatal, 8wk-old) than control (**Figure 3.10 D-I**). Taken together, these results demonstrate that interactions between beige adipocytes and sympathetic nerve endings during an early developmental window are required for establishing the sympathetic network in iWAT, as perturbations during this window lead to lasting effects on parenchymal innervation density.

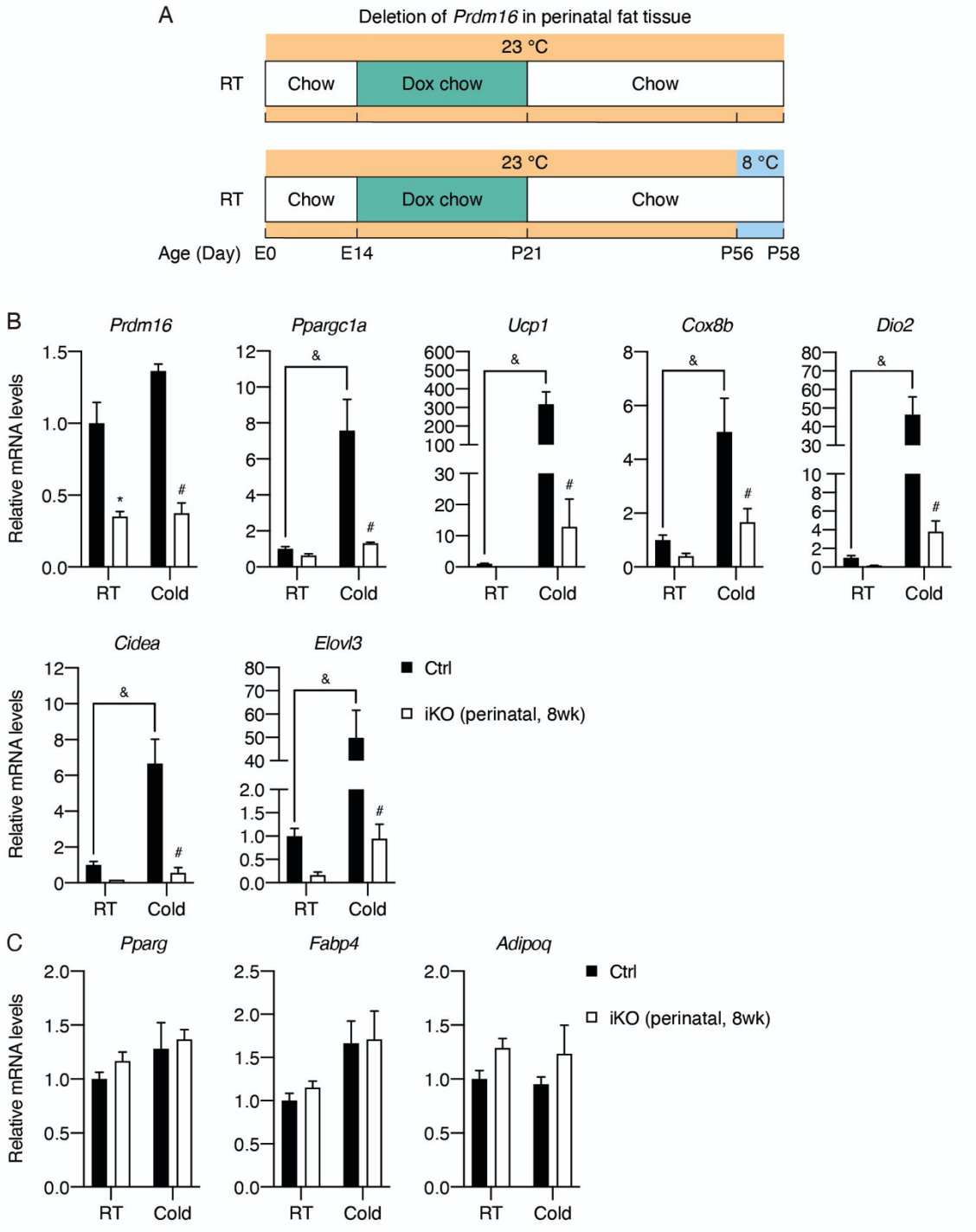
A
Deletion of Prdm16 in perinatal fat tissue
23 °C
RT
Chow
Dox chow
Chow
23 °C
8 °C
RT
Chow
Dox chow
Chow
Age (Day) E0
E14
P21
P56
P58
B
Prdm16
Ppargc1a
Ucp1
Cox8b
Dio2
Relative mRNA levels
RT
Cold
Cidea
Elovl3
Ctrl
iKO (perinatal, 8wk)
C
Pparg
Fabp4
Adipoq
Relative mRNA levels
Ctrl
iKO (perinatal, 8wk)

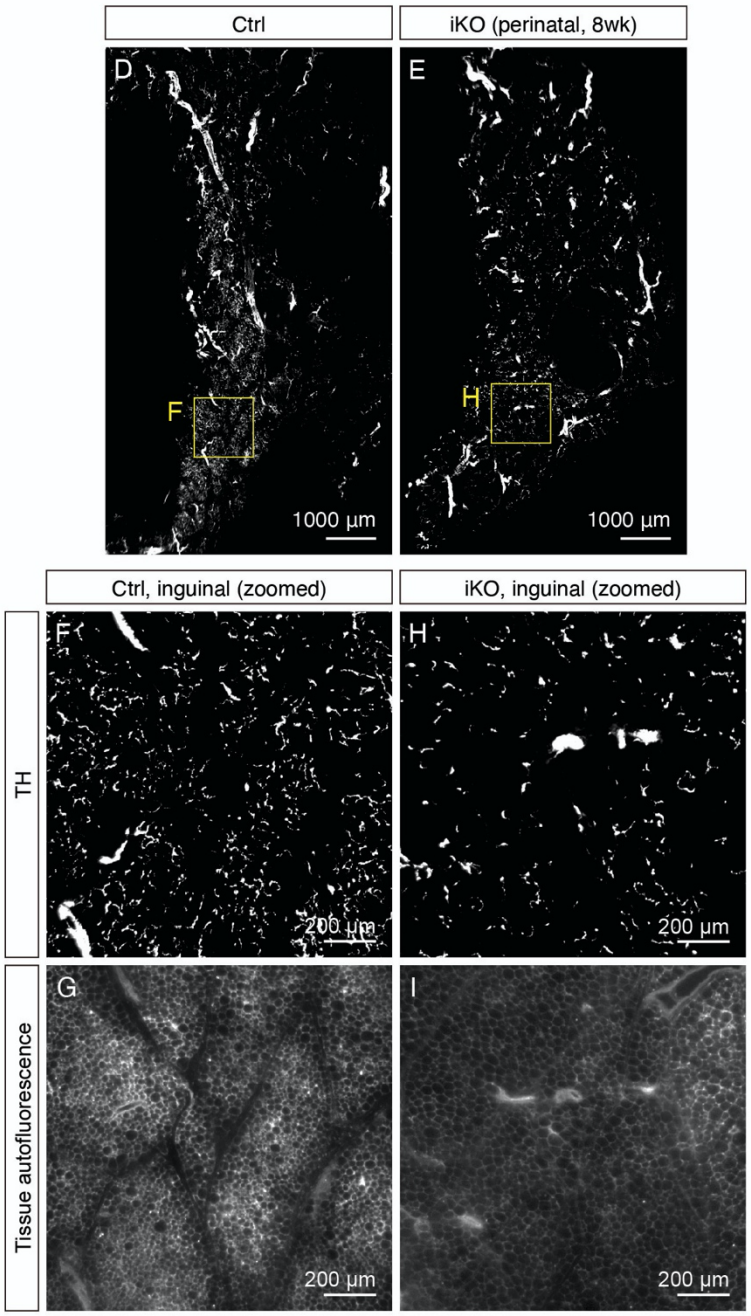
Ctrl
iKO (perinatal, 8wk)
D
E
F
H
1000 µm
1000 µm
Ctrl, inguinal (zoomed)
iKO, inguinal (zoomed)
TH
Tissue autofluorescence
F
H
G
I
200 µm
200 µm
200 µm
200 µm

Figure 3.10 Perinatal deletion of *Prdm16* causes decreased sympathetic parenchymal innervation that persists into adulthood.
(**A**) Control (Cre-) and i*Prdm16*^{KO} (Cre+) mice housed at RT (23 °C) were kept on a doxycycline-containing chow diet from E14 until P21 before being switched to a regular chow diet and maintained until 8 weeks old. Control and i*Prdm16*^{KO} mice were either maintained at RT (23 °C) or exposed to cold (8 °C) for 2 days at P56. (**B-C**) Normalized gene expression of inguinal regions of iWAT from control and i*Prdm16*^{KO} (perinatal, 8wk-old) mice exposed to RT or cold for 2 days, n=3-5. (**B**) Representative genes enriched in thermogenic adipocytes and (**C**) involved in the adipogenic program. Data are normalized to control RT group, presented as mean + SEM, and analyzed by two-way ANOVA followed by Bonferroni's multiple comparisons test. * denotes $p<0.05$ iKO (perinatal, 8wk-old) vs. control samples at RT. # denotes $p<0.05$ iKO vs. control samples at cold. & denotes $p<0.05$ cold- vs. RT-exposed control samples. (**D-I**) Representative optical sections of iWAT from (**D and F**) control and (**E and H**) i*Prdm16*^{KO} (perinatal, 8wk-old) mice maintained at RT, immunolabeled with TH. (**D and E**) Images of the whole iWAT. (**F**) High-magnification optical section of the boxed region in **D**. (**H**) High-magnification optical section of the boxed region in **E**. (**G and I**) Tissue autofluorescence images corresponding to (**F**) and (**H**), respectively. Scale bars are indicated.

3.3.5 Beige adipocyte function is not required for maintaining sympathetic structure during adulthood

Next, we assessed whether beige adipocyte function is also important for maintaining sympathetic parenchymal innervation in adult animals. To that end, we started doxycycline treatment when mice were 8 weeks of age. Following 4 weeks of doxycycline treatment, i*Prdm16*^{KO} (adult deletion) and littermate control mice were placed at either RT or 8°C for two days to allow subsequent analysis of the thermogenic gene program (**Figure 3.11 A**). As expected, doxycycline treatment in adult mice led to a robust reduction in *Prdm16* at the mRNA (83% in the inguinal region of iWAT at RT) and protein levels (**Figure 3.11 B-C**). No body mass difference was observed between i*Prdm16*^{KO} (adult deletion) and control mice (**Figure 3.11 D**). We also observed significant attenuation of cold-induced upregulation in all thermogenic adipocyte markers following *Prdm16* deletion (**Figure 3.11 E**). Consistent with our previous findings, *Prdm16* deletion did not significantly alter markers of adipocyte differentiation (**Figure 3.11 F**).

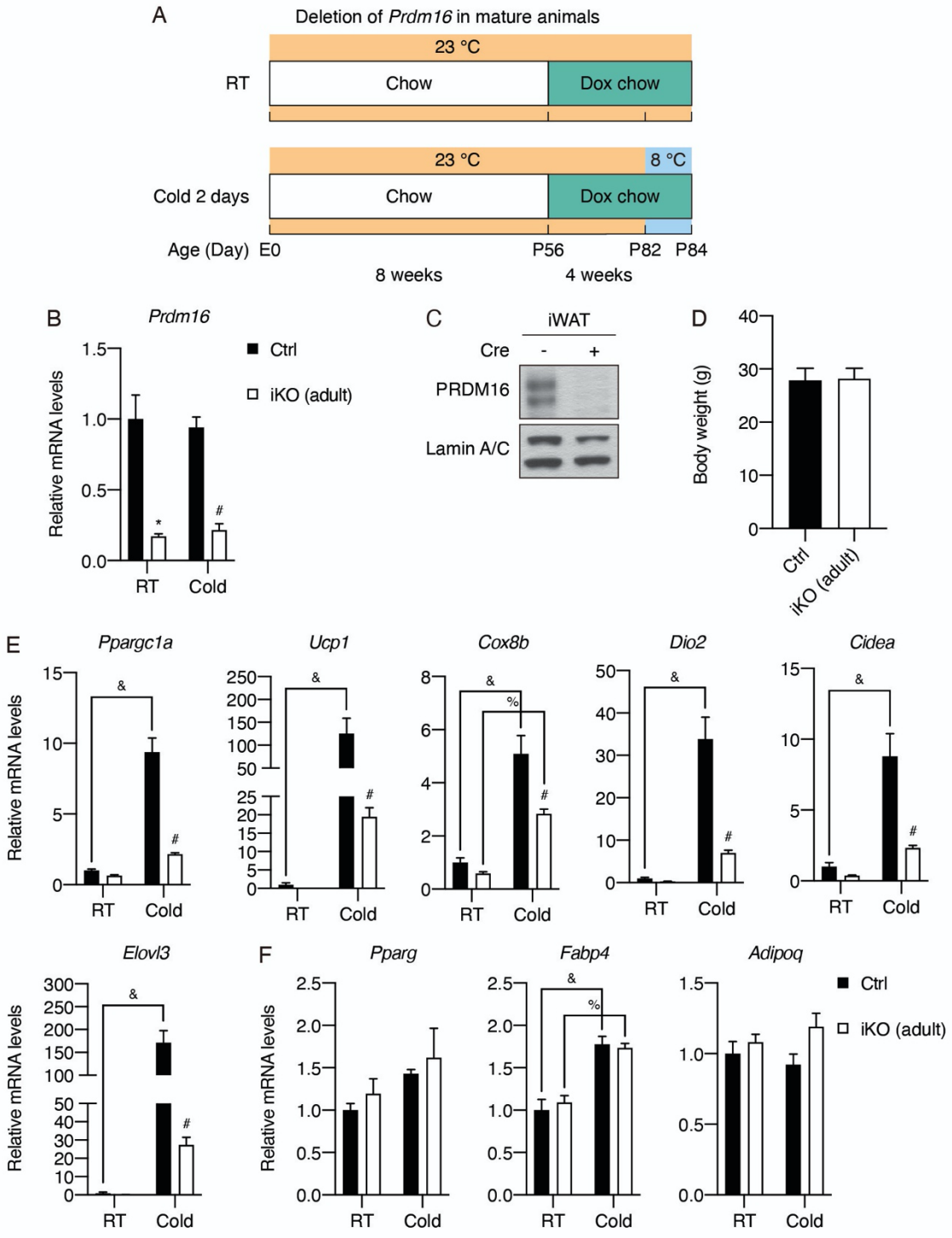
A
Deletion of Prdm16 in mature animals
23 °C
RT
Chow
Dox chow
23 °C
8 °C
Cold 2 days
Chow
Dox chow
Age (Day) E0
P56
P82
P84
8 weeks
4 weeks
B
Prdm16
Relative mRNA levels
Ctrl
iKO (adult)
RT
Cold
C
iWAT
Cre
-
+
PRDM16
Lamin A/C
D
Body weight (g)
Ctrl
iKO (adult)
E
Ppargc1a
Ucp1
Cox8b
Dio2
Cidea
Elovl3
Relative mRNA levels
RT
Cold
F
Pparg
Fabp4
Adipoq
Relative mRNA levels
Ctrl
iKO (adult)
RT
Cold

Figure 3.11 Deletion of *Prdm16* in mature iWAT blocks cold-induced expression of thermogenic adipocyte-enriched genes.
(**A**) Control (Cre-) and i*Prdm16*^{KO} (Cre+) mice housed at RT (23 °C) were kept on a regular chow diet until 8 weeks of age before being switched to a doxycycline-containing chow diet for 4 weeks. Control and i*Prdm16*^{KO} mice were either maintained at RT (23 °C) or exposed to cold (8 °C) for 2 days at the end of doxycycline treatment. (**B**) Normalized *Prdm16* mRNA expression of inguinal regions from control and i*Prdm16*^{KO} (adult) mice exposed to RT or cold, n=3-5. Data are normalized to control RT group, presented as mean + SEM, and analyzed by two-way ANOVA followed by Bonferroni's multiple comparisons test. * denotes $p<0.05$ iKO (adult) vs. control samples at RT. # denotes $p<0.05$ iKO (adult) vs. control samples at cold. (**C**) Western blot of PRDM16 and lamin A/C (loading control) from nuclear extracts of iWAT from control (Cre-) and i*Prdm16*^{KO} (adult) (Cre+) samples. (**D**) Body weights of control and i*Prdm16*^{KO} (adult) mice maintained at RT before sacrifice. Data are presented as mean + SEM and analyzed by Student's t test. (**E-F**) Normalized gene expression of inguinal regions of iWAT from control and i*Prdm16*^{KO} (adult) mice exposed to RT or cold, n=3-5. (**E**) Representative genes enriched in thermogenic adipocytes and (**F**) involved in the adipogenic program. Data are normalized to control RT group, presented as mean + SEM, and analyzed by two-way ANOVA followed by Bonferroni's multiple comparisons test. # denotes $p<0.05$ iKO (adult) vs. control samples at cold. & denotes $p<0.05$ cold- vs. RT-exposed control samples. % denotes $p<0.05$ cold- vs. RT-exposed iKO (adult) samples.

Interestingly, we found dense sympathetic parenchymal innervation present in the inguinal regions of iWAT from both i*Prdm16*^{KO} (adult deletion) and control samples (**Figure 3.12 A-F**). Quantitative analysis of the parenchymal neurite density (normalized by volume) from the 3D images resulted in a small, insignificant decrease (17.6%) in neurite density in adult i*Prdm16*^{KO} relative to control samples (**Figure 3.12 K**). Furthermore, as the adipocytes appeared larger in adult i*Prdm16*^{KO} samples (**Figure 3.12 G-J**), we normalized neurite length by adipocyte density. As a result, we observed a reverse relationship with the neurite density in adult i*Prdm16*^{KO} being slightly higher (1.23-fold) than that of controls (**Figure 3.12 L**). These results suggest that the small density difference when normalized by volume is likely driven by a scaling effect rather than actual neurite remodeling. Importantly, these data indicate that ablating beige adipocyte function in adult animals, at least in this context, causes minimal changes in sympathetic parenchymal neurite density, strongly supporting the early postnatal period being the critical window during which interactions between beige adipocytes and sympathetic nerve endings occur.

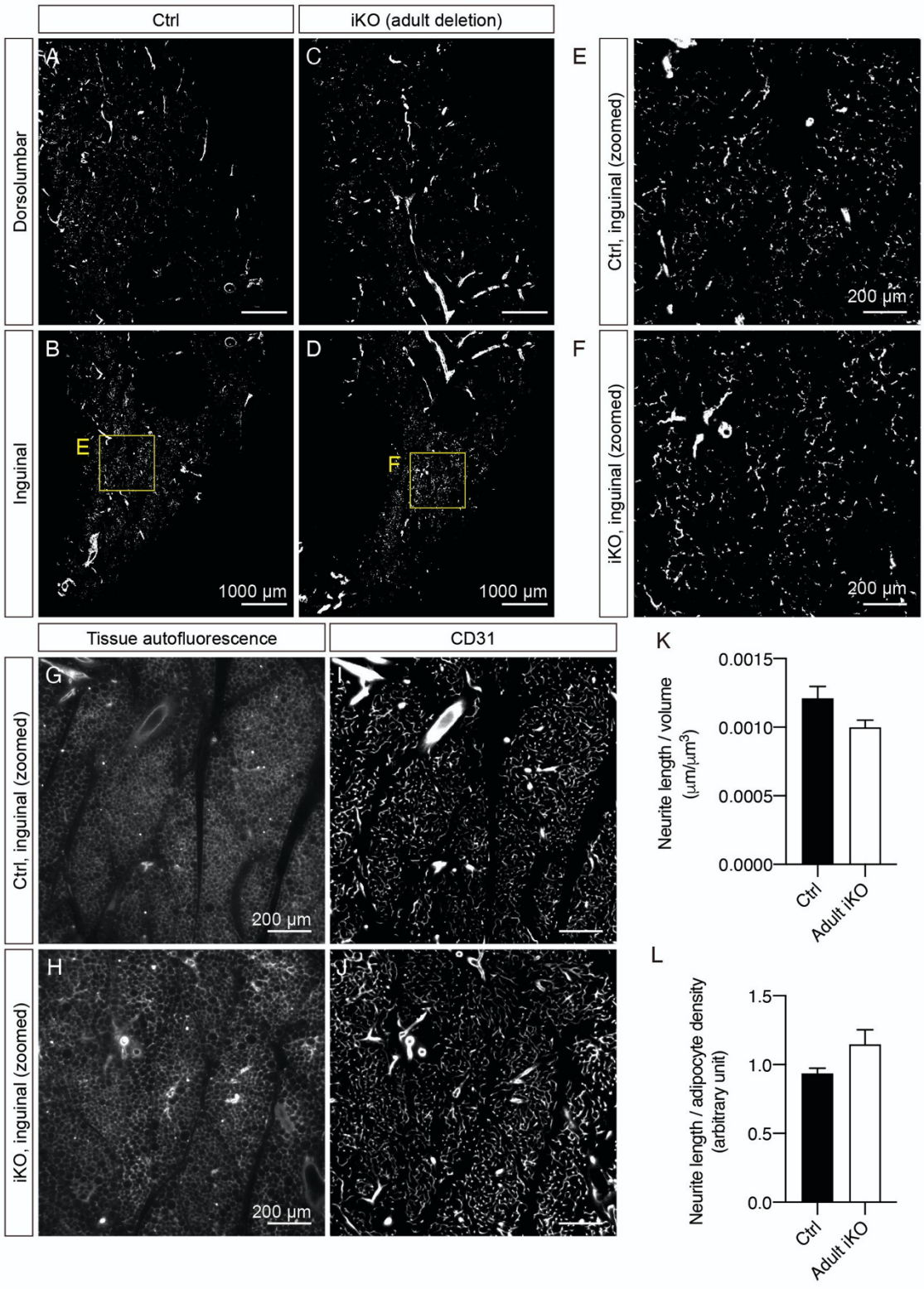
Ctrl
iKO (adult deletion)
Dorsolumbar
Inguinal
A
B
C
D
E
F
1000 µm
1000 µm
Ctrl, inguinal (zoomed)
iKO, inguinal (zoomed)
200 µm
200 µm
Tissue autofluorescence
CD31
G
H
I
J
200 µm
200 µm
K
Neurite length / volume (µm/µm³)
0.0015
0.0010
0.0005
0.0000
Ctrl
Adult iKO
L
Neurite length / adipocyte density (arbitrary unit)
1.5
1.0
0.5
0.0
Ctrl
Adult iKO

Figure 3.12 *Prdm16* is not required for maintaining sympathetic parenchymal innervation in mature iWAT.
(**A-D**) Representative low-magnification optical sections of iWAT from (**A-B**) control and (**C-D**) i*Prdm16*^{KO} (adult deletion) mice maintained at RT. TH channel is presented. (**A and C**) Images of the dorsolumbar region. (**B and D**) Images of the inguinal region. (**E, G, and I**) High-magnification optical sections of the boxed region in **B**. (**F, H, and J**) High-magnification optical sections of the boxed region in **D**. (**E-F**) TH. (**G-H**) Tissue autofluorescence. (**I-J**) CD31. (**K and L**) Quantification of sympathetic parenchymal innervation in inguinal regions with total neurite length normalized to (**K**) regional volume or (**L**) adipocyte density. N=3 biological replicates per genotype were analyzed. Average neurite density from 4-8 randomly selected tissue volumes (technical replicates) contributes to neurite density measurement of one biological sample. Data are presented as mean + SEM and analyzed by Student's t test.

3.3.6 Cold-induced beige adipocyte recruitment during adulthood does not lead to sympathetic neurite outgrowth

In addition to the early postnatal period, beige adipocytes also arise in adult iWAT when stimulated by cold. It is possible that cold-induced beige adipocytes stimulate further sympathetic neurite growth during adulthood. Using two-dimensional sections, a prior study showed a positive correlation between TH+ parenchymal fibers and the number of UCP1+ adipocytes, and reported that cold stimulates sympathetic neurite outgrowth (Murano et al., 2009). Nonetheless, two-dimensional sections are not optimal for delineating TH+ innervation. Moreover, imaging of tissue sections is often performed with high-magnification optical microscopy, which allows detailed examination of cellular properties (Murano et al., 2009; Wang et al., 2013). However, without referring to whole-tissue views, comparisons can be biased by zooming in on regions that are dissimilar to each other.

We revisited the notion of cold-induced neurite outgrowth by careful analysis of sympathetic parenchymal fiber density in iWAT from RT-housed and cold-exposed adult animals using whole-tissue 3D imaging. To achieve robust beige adipocyte recruitment and allow for neurites to remodel, we treated mice with cold for 1 week. The overall sympathetic network in cold-exposed sample was similar to that of the RT condition (**Figure 3.13 A-H**). With high-magnification images, similar regional differences in parenchymal neurite density were found between the inguinal and dorsolateral regions in both conditions (**Figure 3.13 I-R**). Quantification of neurite density in 3D images showed no evidence that cold itself induced neurite outgrowth in either region when compared to RT (**Figure 3.13 S-U**). However, when TH protein levels were analyzed by immunoblotting whole tissue lysate with the same TH antibody, we observed a 1.5-fold increase in TH protein following 1 week of cold exposure (**Figure 3.13 V-W**), possibly suggesting cold-induced upregulation in TH protein content without structural remodeling. Taken together, when similar anatomical regions were compared between samples, we found no apparent induction in parenchymal neurite outgrowth following cold challenge in iWAT.

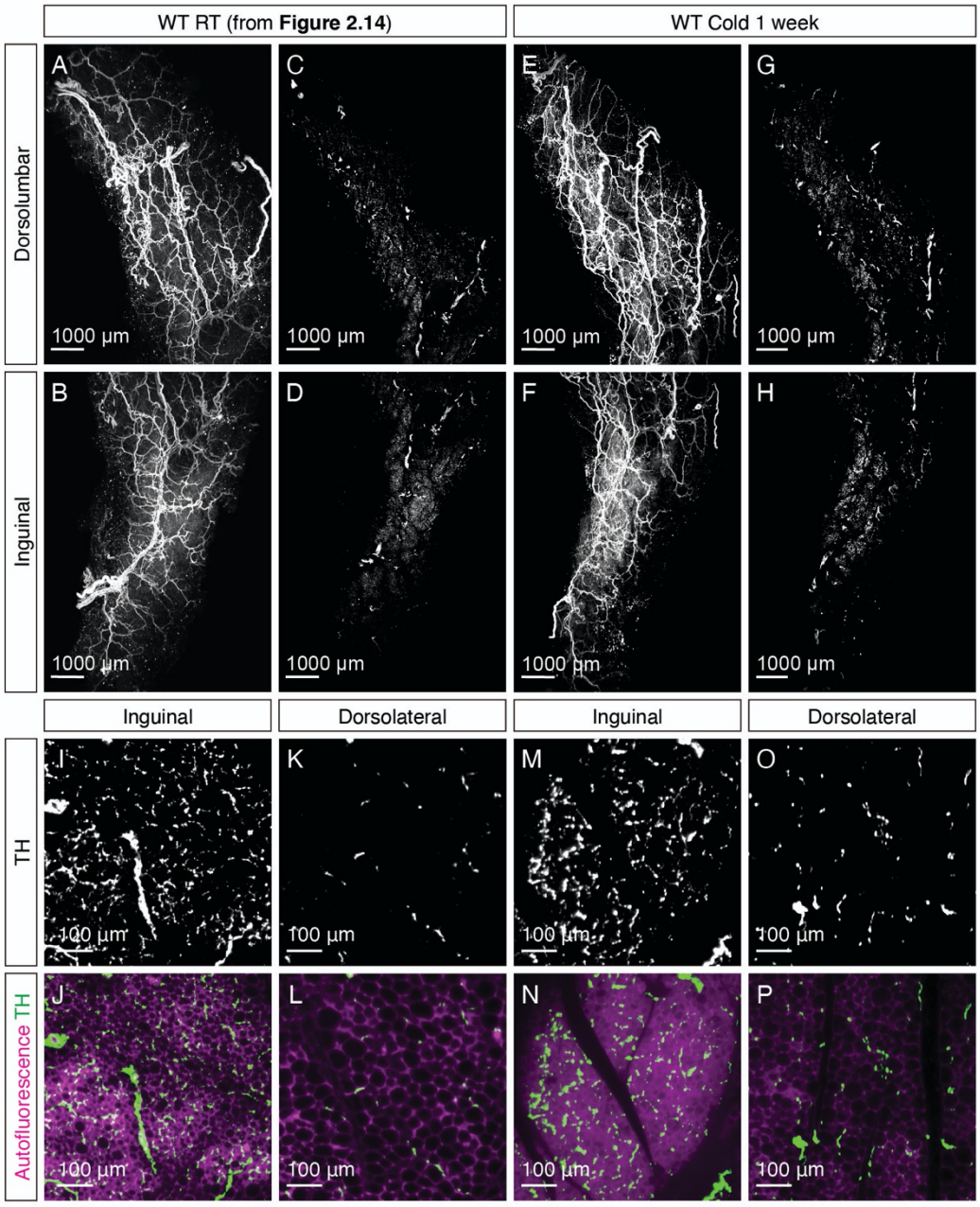
WT RT (from Figure 2.14)
WT Cold 1 week
Dorsolumbar
Inguinal
A
B
C
D
E
F
G
H
1000 µm
Inguinal
Dorsolateral
Inguinal
Dorsolateral
TH
Autofluorescence TH
I
J
K
L
M
N
O
P
100 µm

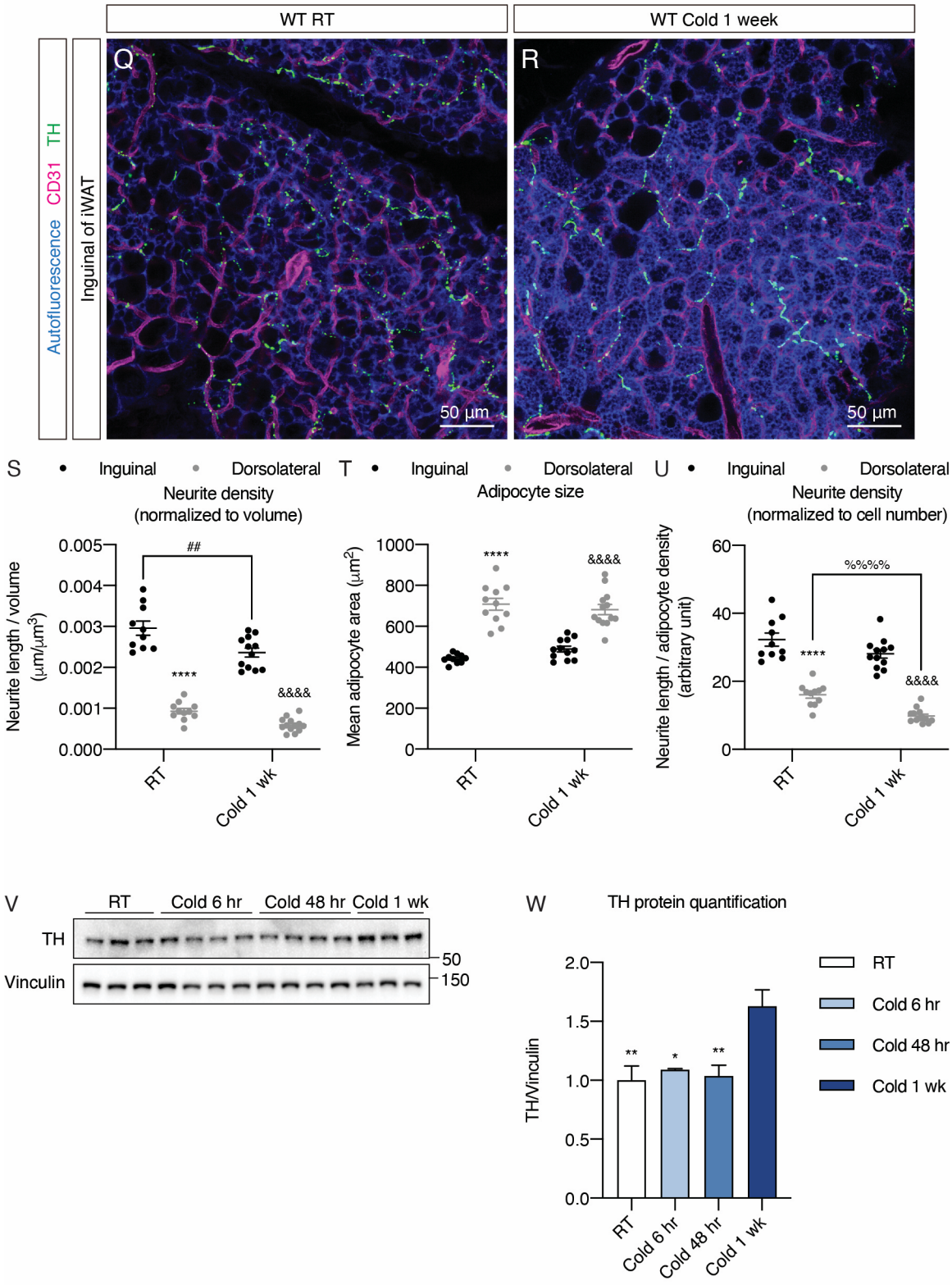
WT RT
WT Cold 1 week
Q
R
Autofluorescence CD31 TH
Inguinal of iWAT
50 µm
50 µm
S
Inguinal
Dorsolateral
Neurite density
(normalized to volume)
Neurite length / volume
(µm/µm3)
0.005
0.004
0.003
0.002
0.001
0.000
##
****
&&&&
RT
Cold 1 wk
T
Inguinal
Dorsolateral
Adipocyte size
Mean adipocyte area (µm2)
1000
800
600
400
200
0
****
&&&&
RT
Cold 1 wk
U
Inguinal
Dorsolateral
Neurite density
(normalized to cell number)
Neurite length / adipocyte density
(arbitrary unit)
60
40
20
0
%%%%
****
&&&&
RT
Cold 1 wk
V
RT
Cold 6 hr
Cold 48 hr
Cold 1 wk
TH
Vinculin
50
150
W
TH protein quantification
TH/Vinculin
2.0
1.5
1.0
0.5
0.0
**
*
**
RT
Cold 6 hr
Cold 48 hr
Cold 1 wk
RT
Cold 6 hr
Cold 48 hr
Cold 1 wk

Figure 3.13 Analysis of sympathetic innervation of iWAT following 1 week of cold exposure. (**A-B and E-F**) Maximum intensity projections of the entire z-stacks and (**C-D and G-H**) representative maximum intensity projections of 20 μm z-stacks from iWAT samples from 8-week-old WT C57BL6/J mice housed at (**A-D**) RT or (**E-H**) 8°C for 1 week. TH channel is presented. WT RT sample was the same as **Figure 2.14**. (**A, C, E, and G**) Images of the dorsolumbar region. (**B, D, F, and H**) Images of the inguinal region. (**I-P**) Representative optical sections with high magnification. (**I-J**) Inguinal region of WT RT. (**K-L**) Dorsolateral region of WT RT. (**M-N**) Inguinal region of WT cold 1 week. (**O-P**) Dorsolateral region of WT cold 1 week. (**I, K, M, and O**) TH channel. (**J, L, N, and P**) Overlay of TH (green) and autofluorescence (magenta). (**Q-R**) Confocal images of iWAT from 8-week-old WT mice exposed (**Q**) RT or (**R**) cold 1 week, stained with TH and CD31. MIPs of 5 μm z-stacks from a representative lobule in the inguinal region are presented. Images contain autofluorescence (blue), CD31 (magenta), and TH (green). Scale bars are indicated. (**S-U**) Quantification of sympathetic parenchymal neurite density and adipocyte size in the inguinal and the dorsolateral regions from WT RT and WT cold 1 week mice. (**S**) Total neurite length normalized to regional volume. (**T**) Mean adipocyte area. (**U**) Total neurite length normalized to adipocyte density. Individual data points are plotted with mean ± SEM and analyzed by two-way ANOVA followed by Bonferroni's multiple comparisons test. **** denotes $p<0.0001$ inguinal vs. dorsolateral in WT RT. ## denotes $p<0.01$ inguinal regions of WT RT vs. WT cold 1 week. &&&& denotes $p<0.0001$ inguinal vs. dorsolateral in WT cold 1 week. %%%% denotes $p<0.0001$ dorsolateral regions of WT RT vs. WT cold 1 week. (**V**) Western blot of TH and vinculin (loading control) from iWAT of the same animals as **Figure 2.4 B**. (**W**) Quantification of the blot in **V**, with TH normalized to vinculin. Molecular weights are indicated as kDa. Data are normalized to RT group, presented as mean + SEM, and analyzed by one-way ANOVA followed by Bonferroni's multiple comparisons test. * and ** denote $p<0.05$ and $p<0.01$ vs. cold 1 week group.

3.3.7 *Prdm16* deletion does not affect sympathetic innervation in iBAT

Interestingly, although PRDM16 also plays a critical role in brown adipocyte determination and function, deletion of *Prdm16* in iBAT does not affect its development or thermogenic function in young adults (Cohen et al., 2014; Harms et al., 2014). Previous studies have shown that the role of PRDM16 in iBAT formation and function is compensated for by PRDM3, a transcriptional regulator closely related to PRDM16 (Harms et al., 2014). Consistent with these findings, we detected similarly extensive sympathetic parenchymal innervation in iBAT of both control and c*Prdm16*^{KO} mice (**Figure 3.14 A-B**). Similarly, perinatal *Prdm16* knockout in adipocytes did not significantly affect thermogenic or adipogenic markers in iBAT (**Figure 3.14 C-D**). In line with this, the sympathetic parenchymal innervation levels did not appear different between control and perinatal i*Prdm16*^{KO} iBAT samples (**Figure 3.14 E-F**).

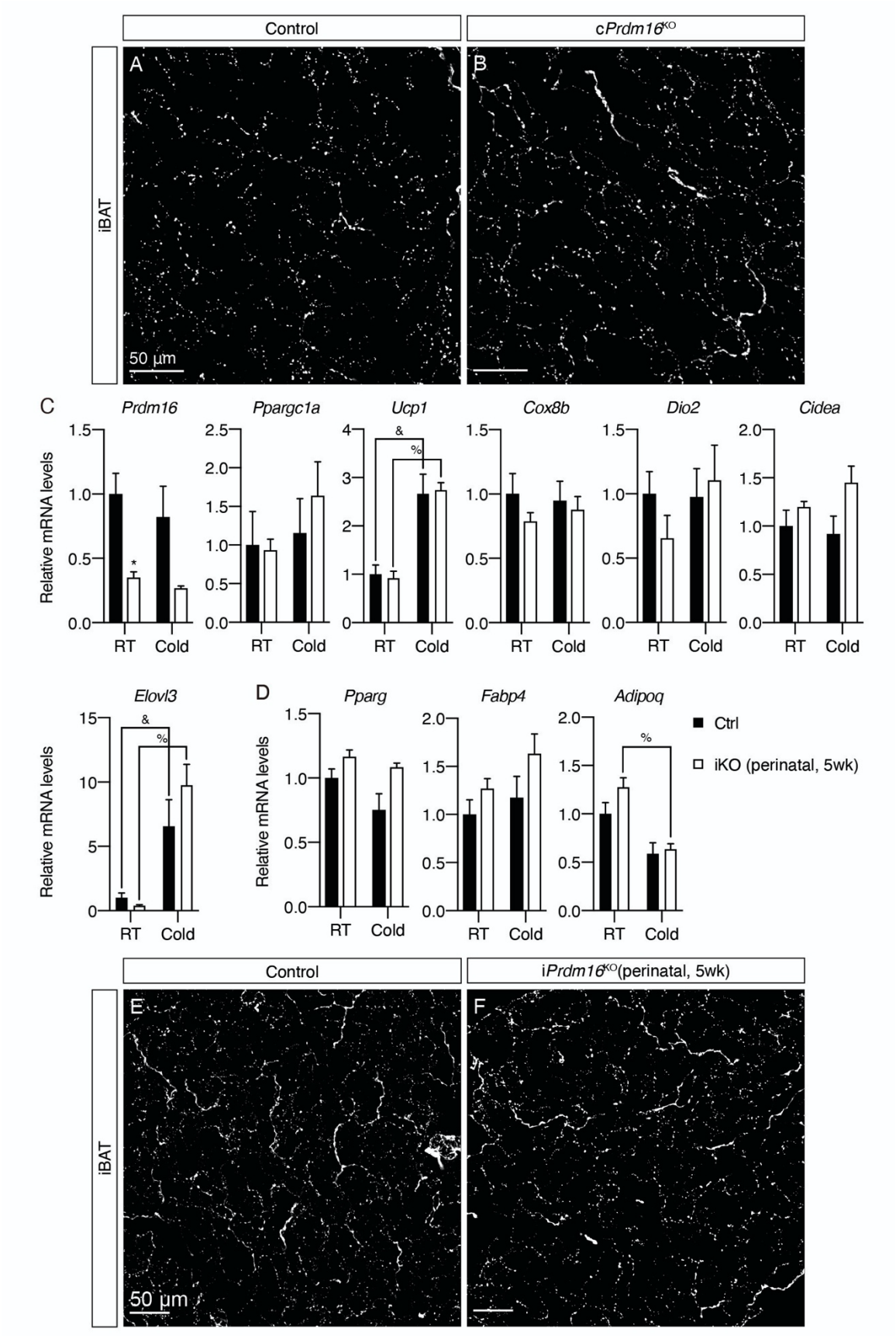
Control
cPrdm16KO
iBAT
A
B
50 μm
C
Prdm16
Ppargc1a
Ucp1
Cox8b
Dio2
Cidea
Relative mRNA levels
RT
Cold
Elovl3
D
Pparg
Fabp4
Adipoq
Ctrl
iKO (perinatal, 5wk)
Control
iPrdm16KO(perinatal, 5wk)
E
F
50 μm

Figure 3.14 *Prdm16* deletion does not affect sympathetic innervation or thermogenic gene expression in iBAT.
(**A-B**) Representative images of iBAT sections from (**A**) control and (**B**) c*Prdm16*^{KO} 8-week-old mice, immunolabeled with TH. MIPs of 5 μm z-stacks are shown. (**C-D**) Normalized gene expression of iBAT from control and i*Prdm16*^{KO} (perinatal, 5wk-old) mice exposed to RT or cold, n=3-5. (**C**) Representative genes involved in the thermogenic program and (**D**) the adipogenic program. Data are normalized to control RT group, presented as mean + SEM, and analyzed by two-way ANOVA followed by Bonferroni's multiple comparisons test. * denotes $p<0.05$ iKO (perinatal, 5wk-old) vs. control samples at RT. & denotes $p<0.05$ cold- vs. RT-exposed control samples. % denotes $p<0.05$ cold- vs. RT-exposed iKO (perinatal, 5wk-old) samples. (**E-F**) Representative images of iBAT sections from (**E**) control and (**F**) i*Prdm16*^{KO} (perinatal, 5wk-old) mice, immunolabeled with TH. MIPs of 10 μm z-stacks are shown. Scale bars are indicated.

3.4 Discussion

The association between thermogenic adipocytes and dense sympathetic innervation has been reported by several groups including us. When and how this association is established has remained unclear. Here, our studies showed that sympathetic neurite density depends on the presence of functional beige adipocytes. Adipocyte-specific deletion of *Prdm16* ablated beige adipocyte function and significantly reduced sympathetic neurite density in the inguinal region of iWAT, suggesting that adipocytes can interact with neurons to modulate neurite density. To investigate when this modulation occurs, we delineated key stages of sympathetic nervous system development in iWAT using whole tissue imaging. Specifically, we observed that sympathetic parenchymal innervation in close apposition to adipocytes is established between P6 and P28. Importantly, the appearance of UCP1+ beige adipocytes precedes the emergence of dense parenchymal neurites during early postnatal development. We further demonstrated that both early postnatal beige adipocytes and dense parenchymal neurites depend on *Prdm16* expression in adipocytes. Using an inducible *Prdm16* deletion model, we identified an early critical period during which beige adipocytes modulate sympathetic axon growth. However, *Prdm16* deletion in adult mice did not alter the sympathetic structure.

3.4.1 Development of the sympathetic nervous system and beige adipocytes during the early postnatal period

Assisted by whole-tissue images, our studies carefully examined the growth of sympathetic axons in iWAT. We observed that sympathetic fibers travel in nerve fascicles to arrive at iWAT, and then depart from nerve fascicles to reach main blood vessels within iWAT. By P6, the sympathetic innervation on blood vessels demonstrated a dense mesh-like structure, resembling that of mature iWAT. However, dense parenchymal innervation surrounding adipocytes, which several studies have characterized in mature iWAT (Chi et al., 2018a; Jiang et al., 2017a), is not established at P6. Instead, we observed sparse discrete sympathetic fibers and small vessels in congruence within the tissue parenchyma, a common phenomenon in sympathetic nerve fiber development where vasculature serves as a guide to direct developing fibers to reach their targets, such as the heart (Nam et al., 2013). Subsequently, from P10 until P28, dense parenchymal innervation becomes obvious where clusters of UCP1+ beige adipocytes are located.

Although beige adipocytes emerge in white fat depots of adult mice following cold challenge, we observed strong beige adipogenesis during early postnatal development, similar to the "peri-weaning" beige adipocytes reported in recent studies (Wu et al., 2020a, 2020b). Using high-resolution whole tissue imaging focusing on the inguinal region of iWAT, we detected scattered UCP1+ adipocytes at P6, subsequent emergence of small UCP1+ adipocyte clusters at P10, and an expansion to almost all lobules from P14 to P28. On the other hand, beige adipogenesis is delayed in the dorsolumbar region, where small clusters of beige adipocytes are not detected until P14. Potential mechanisms driving the preferential localization of early postnatal beige adipocytes will be discussed in more detail in **Chapter 4**.

3.4.2 Modulation of sympathetic patterning by beige adipocytes occurs during a critical period

Using constitutive and inducible adipocyte-specific *Prdm16* deletion models, we observed ablation of early postnatal beige adipocyte function and dramatically reduced parenchymal sympathetic neurites in iWAT. Our findings suggest that early postnatal beige adipocytes may express PRDM16-dependent neurotrophic factors that stimulate sympathetic axon growth or downregulate inhibition cues. Recent studies have unveiled important roles of brown adipocyte-derived factors, such as S100B and TGFβ1, in regulating sympathetic innervation in iBAT (Hu et al., 2020; Zeng et al., 2019). As beige and brown adipocytes share similarities, it is possible that these factors may also affect sympathetic innervation in iWAT. Interestingly, *S100b*, but not *Tgfb1*, showed a regional pattern at the mRNA level during early iWAT development, with higher expression in the inguinal region in a PRDM16-dependent manner (**Figure 3.15**). This result suggests that S100B may be one of the potential cues in regulating iWAT sympathetic development. It is also likely that sympathetic neurites are indirectly regulated by additional beige adipocyte-associated cell types, such as immune or stromal cells. Follow-up studies will need to evaluate the role of S100B and other potential factors in modulating sympathetic axon growth during early iWAT morphogenesis.

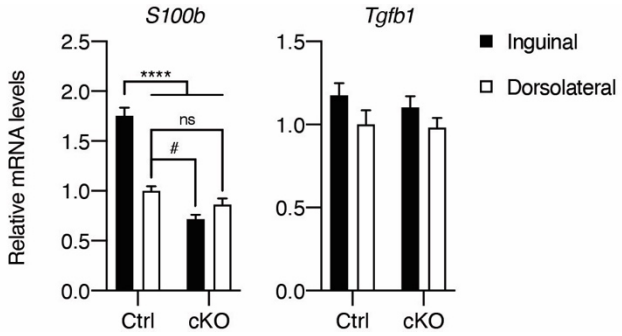

Figure 3.15 mRNA analysis of potential neurotrophic factors in iWAT.
qPCR analysis of *S100b* and *Tgfb1* mRNA levels in inguinal and dorsolateral regions of control and c*Prdm16*^{KO} mice at P14, n=4. Data are normalized to control dorsolateral group, presented as mean + SEM, and analyzed by two-way ANOVA followed by Bonferroni's multiple comparisons test. **** denotes $p<0.0001$ control inguinal vs. the rest of the groups. # denotes $p<0.05$ control dorsolateral vs. cKO inguinal.

Our studies using an inducible adipocyte-specific *Prdm16* deletion model indicated a critical developmental window for the interactions between beige adipocytes and sympathetic nerve terminals. Restricted *Prdm16* deletion during early tissue morphogenesis resulted in a lasting reduction in parenchymal neurite density. However, *Prdm16* deletion in fully mature mice failed to alter sympathetic neurite density. These results indicate that sympathetic neurites in iWAT respond to signals from beige adipocytes or associated cells during early development. However, when the innervation pattern is fully established, such signals are no longer required for maintaining the innervation level during adulthood. In line with this, we observed that cold-induced beige adipocytes do not promote sympathetic neurite outgrowth in adult iWAT when equivalent tissue regions are compared. Taken together, our data suggest that sympathetic neurite

density is regulated by local cues from beige adipocytes during a specific developmental window and exhibits limited plasticity once the pattern is established.

Of note, a recent study demonstrated leptin-mediated central regulation of sympathetic innervation in adipose tissue (Wang et al., 2020). Specifically, chronic leptin treatment acting on hypothalamic neurons was found to rescue the defect in sympathetic innervation in iBAT and iWAT of adult leptin-deficient mice. It is possible that the central and local regulation of sympathetic innervation in adipose tissue acts with different timing and through distinct mechanisms. Interestingly, the sympathetic axon growth period we observed (P10-P21) largely overlaps with a postnatal leptin surge (P8-P20) reported previously (Ahima et al., 1998; Wu et al., 2020a). Future studies are needed to uncouple central (leptin surge) and local (beige adipocyte-associated factors) effects to fully understand how adipose sympathetic innervation is regulated by each mechanism. It is also worth noting that current studies rely on neurite morphological changes such as length to characterize sympathetic growth or remodeling. As adipocyte size dramatically changes in response to caloric excess or deprivation, sympathetic neurite density may appear different even without active remodeling. A better understanding of sympathetic neurite structural change will be assisted by identifying markers specific to actively remodeling neurites.

Thermogenic adipocytes have been demonstrated to provide metabolic benefits that may combat obesity and associated metabolic diseases. As thermogenic adipocytes are primarily induced by sympathetic stimulation, many studies have turned to the sympathetic nervous system in search of novel therapeutic targets for enhancing thermogenic adipocyte function. Our studies here demonstrated a critical developmental window during which beige adipocytes regulate sympathetic neurite density, providing fundamental knowledge about the development of the sympathetic nervous system in mouse subcutaneous white fat and providing a framework for future attempts to identify the molecular mechanism underlying this regulation. Our imaging studies in murine adipose tissue will also serve as a guide for future studies that investigate the organization of human brown and white adipose tissue.

CHAPTER 4. Formation of beige adipocytes in murine subcutaneous fat

4.1 Introduction

Whole-tissue imaging of beige adipocyte distribution revealed strong regionality in iWAT. To address whether beige adipocyte spatial distribution is due to regional differences in tissue microenvironment such as the sympathetic nervous system, we carefully examined the interaction between beige adipocytes and sympathetic innervation. We indeed found denser sympathetic parenchymal neurites localizing to regions where beige adipocytes readily arise. However, this innervation pattern is in fact set by beige adipocytes that emerge during the early postnatal period. These data led us to examine whether beige adipocyte regionality is due to intrinsic differences in adipocytes or adipocyte progenitor cells in various regions.

How beige adipocytes emerge and the identity of beige adipocyte progenitor cells have been studied extensively for almost a decade. However, the answers to these questions still remain unclear. Beige adipocytes are suggested to be either a phenotypic variation of white adipocytes or a completely distinct cell type (Shao et al., 2019). While active beige adipocytes have been shown to arise from conversion of existing white-like adipocytes (Barbatelli et al., 2010; Lee et al., 2015), they have also been found to derive from *de novo* differentiation of progenitor cells with a unique molecular profile (Berry et al., 2016; Long et al., 2014; Wang et al., 2013; Wu et al., 2012) (**Figure 1.3**). Several fate mapping studies investigated the mode of formation for beige adipocytes and provided evidence supporting both conversion from existing white mature adipocytes as well as *de novo* differentiation from progenitor cells (Lee et al., 2015; Shao et al., 2019; Wang et al., 2013). However, it remains puzzling as to why beige adipocytes with distinct lineages could also arise from phenotypic conversion of mature white adipocytes.

Importantly, the previous fate mapping studies relied on high-magnification optical microscopy, with the regional information largely lost. Using whole-tissue imaging, we previously observed that the length of cold exposure and the spatial location within iWAT are important factors that influence the behavior of beige adipocytes (**Figure 2.5**). The results from this study and our future experiments will take into account the developmental stages, whole tissue architecture, and length of cold stimulation. A holistic view will provide a better understanding of how beige adipocytes arise.

Moreover, the identity of beige adipocyte progenitor cells remains unclear. Several studies have pointed to vascular smooth muscle cells as a source of beige adipocyte progenitor cells (Berry et al., 2016; Long et al., 2014). Although lineage tracing of vascular smooth muscle cells indeed resulted in robust labeling of UCP1+ beige adipocytes, a large proportion (30-40%) still remained unlabeled (Berry et al., 2016), suggesting potential heterogeneity in beige progenitor cells. Single cell RNA sequencing will be needed to address this question.

In this chapter, we further characterized early postnatal beige adipocytes and uncovered a surprising link between early postnatal and adult beige adipocytes. Through fate mapping of early postnatal beige adipocytes, we found that they were predominantly traced into UCP1+ beige adipocytes in adult iWAT. Furthermore, early postnatal beige adipocytes appeared to come from distinct beige progenitor cells and developed independently from sympathetic activation. Building

upon these observations, we suggest a new model for beige adipocyte formation and discuss future directions that are needed to clarify the origin and fate of beige adipocytes.

4.2 Characterization of early postnatal beige adipocytes

Although it is well-known that beige adipocyte biogenesis can be activated in adult murine iWAT, we and others have recently reported the presence of early postnatal beige adipocytes in the same fat depot (Chi et al., 2021; Wu et al., 2020a, 2020b). While using whole-tissue imaging to investigate how sympathetic innervation is regulated by beige adipocytes, we serendipitously observed the developmental pattern of early postnatal beige adipocytes, which actively expanded from a few scattered cells on P6, to small cell clusters on P10, to entire lobules on P28 (**Figure 4.1 A-R**). Remarkably, the emergence of early postnatal beige adipocytes also exhibits regionality. UCP1+ adipocytes developed in the inguinal region as early as P6 (**Figure 4.1 A-C**), while those in the dorsomedial region did not become apparent until P14 (**Figure 4.1 G, H, and J**). However, minimal UCP1+ cells were found in the dorsolateral region across all early postnatal time points (**Figure 4.1 A-R**). It is worth noting that the whole-tissue UCP1+ patterns at P21 and P28 closely resemble that of adult mice following cold exposure (**Figure 4.1 K, L, M, and P**).

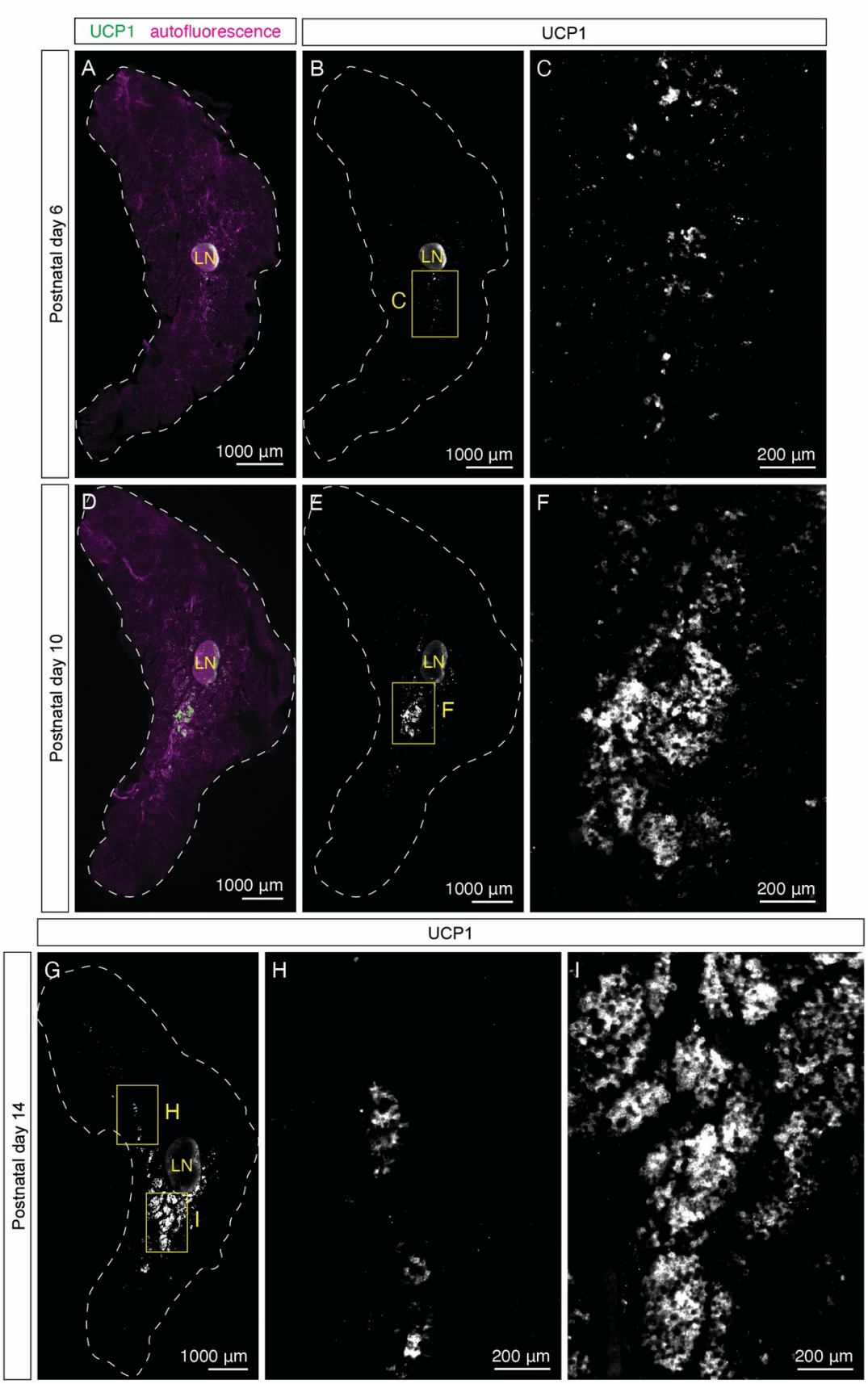
UCP1 autofluorescence
UCP1
Postnatal day 6
Postnatal day 10
Postnatal day 14
A
B
C
D
E
F
G
H
I
LN
1000 µm
200 µm

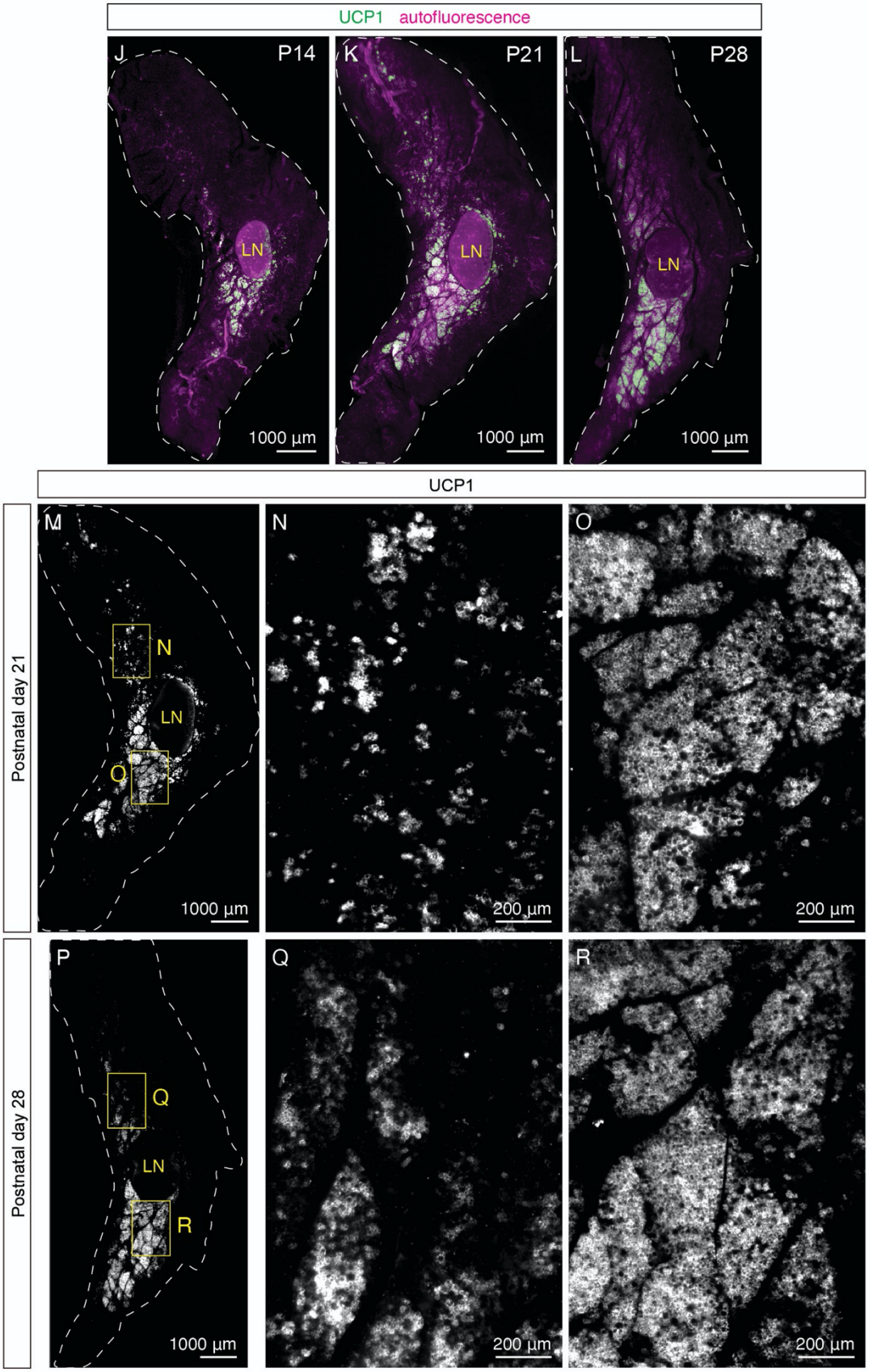
UCP1 autofluorescence
J
P14
LN
1000 µm
K
P21
LN
1000 µm
L
P28
LN
1000 µm
UCP1
Postnatal day 21
M
N
LN
Q
1000 µm
N
200 µm
O
200 µm
Postnatal day 28
P
Q
LN
R
1000 µm
Q
200 µm
R
200 µm

Figure 4.1 Development of early postnatal beige adipocytes in iWAT.
Representative optical sections of iWAT from P6, P10, P14, P21, and P28 C57BL6/J mice immunolabeled with UCP1. The same samples are shown in **Figure 3.5**. (**A-B**) Whole-tissue optical sections of a P6 iWAT. (**A**) UCP1 (green) and autofluorescence (magenta). (**B**) UCP1 channel. (**C**) High-magnification view of the boxed inguinal region in **B**. (**D-F**) Whole-tissue optical sections of a P10 iWAT. (**D**) UCP1 (green) and autofluorescence (magenta). (**E**) UCP1 channel. (**F**) High-magnification view of the boxed inguinal region in **E**. (**G**) Whole-tissue optical section of a P14 iWAT, with UCP1 staining. (**H**) High-magnification view of the boxed dorsolumbar region in **G**. (**I**) High-magnification view of the boxed inguinal region in **G**. (**J-L**) Whole-tissue optical sections of iWAT samples from (**J**) P14, (**K**) P21, and (**L**) P28 mice. Tissue autofluorescence (magenta) and UCP1 (green) are shown. (**M**) Whole-tissue optical section of P21 iWAT with UCP1 channel, corresponding to **K**. (**N**) High-magnification view of the boxed dorsolumbar region in **M**. (**O**) High-magnification view of the boxed inguinal region in **M**. (**P**) Whole-tissue optical section of P28 iWAT with UCP1 channel, corresponding to **L**. (**Q**) High-magnification view of the boxed dorsolumbar region in **P**. (**R**) High-magnification view of the boxed inguinal region in **P**. Lymph node is indicated as LN. Scale bars are indicated. Imaging was performed in at least three independent animals, and representative images are shown.

4.2.1 Molecular analysis of early postnatal beige adipocytes

While whole-tissue imaging allowed comprehensive analysis of beige adipocyte emergence in developing iWAT, quantitative assessment of fluorescent intensities from sample to sample is challenging. For example, fluorescent signals in thick samples may appear artificially low as light has to travel long distances to reach the detector. In order to obtain a quantitative measure of early postnatal beige adipocytes, we performed mRNA analysis of thermogenic adipocyte-enriched genes in developing iWAT. Due to small tissue size, we analyzed inguinal and dorsolumbar regions, without further separating the dorsolumbar into the medial and lateral sub-regions (**Figure 4.2 A**). Data from the dorsolumbar region will therefore represent an intermediate phenotype of the two sub-regions.

In line with the imaging results, *Ucp1* mRNA expression showed a gradual increase from P6 to P14 in the inguinal region (**Figure 4.2 B**). To our surprise, although we observed more extensive UCP1+ adipocytes in the inguinal region at P21 and P28 by imaging, *Ucp1* mRNA levels peaked around P12-P16, with the expression level at P14 being 4-fold and 8-fold higher than that of P21 and P28, respectively (**Figure 4.2 B**). Other thermogenic adipocyte markers (*Cidea* and *Cox8b*) also gradually increased their mRNA expression from P6 to P14, followed by a small downward trend after P21 (**Figure 4.2 B**). These quantitative transcriptional data suggest that early postnatal beige adipocytes may exhibit peak thermogenic potential around two to three weeks of age and gradually become less active as animals mature. On the other hand, all thermogenic adipocyte markers showed significantly lower mRNA expression in the dorsolumbar region compared to the inguinal region at most time points (**Figure 4.2 B**).

Of note, *Prdm16*, the transcriptional coregulator that determines beige adipocyte phenotype, showed a consistent 1.5 to 2-fold increase in mRNA levels in the inguinal relative to the dorsolumbar region across all time points (**Figure 4.2 C**). Other transcriptional regulators of beige adipocyte development, such as *Cebpb* and *Ppargc1a*, showed similarly consistent regional differences (around 1.5-fold for *Cebpb* and 2-fold for *Ppargc1a*) during early development (**Figure 4.2 C**). Furthermore, we did not observe any significant regional differences in markers of adipocyte maturation and function (*Fabp4*, *Pparg*, and *Adipoq*) (**Figure 4.2 D**). Taken together, these data indicate that adipocytes from the two regions of iWAT are equally differentiated, but the inguinal region harbors more beige adipocytes that express high levels of thermogenic markers. Moreover, it is possible that the inguinal region may harbor more beige progenitor cells or mature adipocytes with the potential to emerge as beige adipocytes.

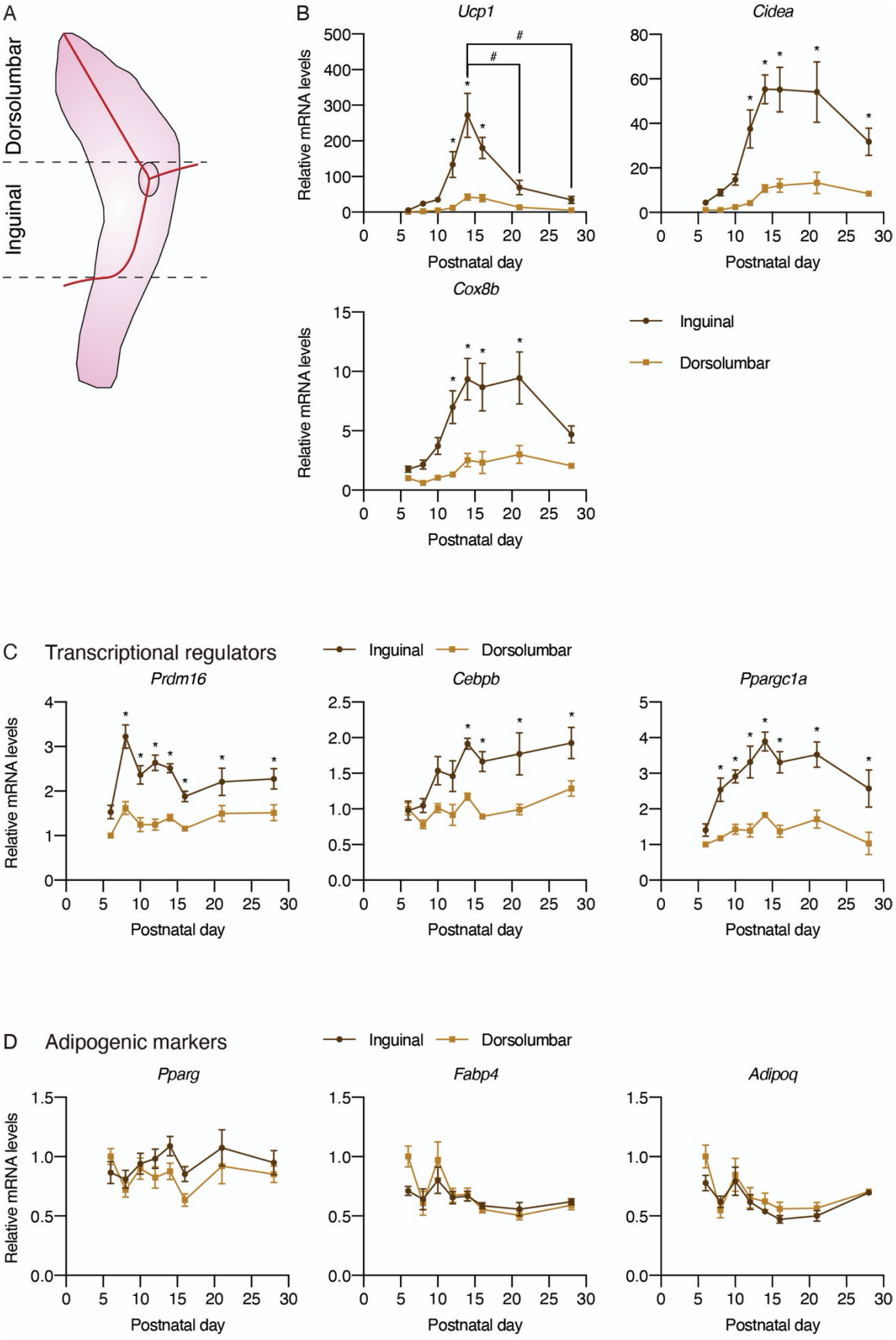
A
Dorsolumbar
Inguinal
B
Ucp1
Cidea
Cox8b
Relative mRNA levels
Postnatal day
Inguinal
Dorsolumbar
C
Transcriptional regulators
Prdm16
Cebpb
Ppargc1a
D
Adipogenic markers
Pparg
Fabp4
Adipoq

Figure 4.2 Quantitative analysis of early postnatal beige adipocytes.
(**A)** Schematic illustration of regional dissection of iWAT. **(B-D**) Normalized gene expression of dorsolumbar vs. inguinal regions in iWAT from P6, P8, P10, P12, P14, P16, P21, and P28 C57BL6/J mice, n=4. Representative genes involved in (**B**) the thermogenic program, (**C**) transcriptional regulation of beige adipocyte development and function, and (**D**) the adipogenic program. Data are presented as mean ± SEM and analyzed by two-way ANOVA followed by Bonferroni's multiple comparisons test. * denotes $p<0.05$ dorsolumbar vs. inguinal region at each time point. # denotes $p<0.05$ inguinal region at P14 in comparison to inguinal regions at other time points.

4.3 The link between early postnatal beige adipocytes and cold-induced beige adipocytes during adulthood

Whole-tissue imaging in developing and adult iWAT revealed remarkably similar distribution patterns of UCP1+ adipocytes, suggesting there may be a link between early postnatal and adult beige adipocytes. In addition, the thermogenic gene expression of early postnatal beige adipocytes diminishes as mice mature. It is possible that early postnatal beige adipocytes gradually become inactivated during maturation, and cold challenge re-activates the same cells in adult mice (**Figure 4.3 A**).

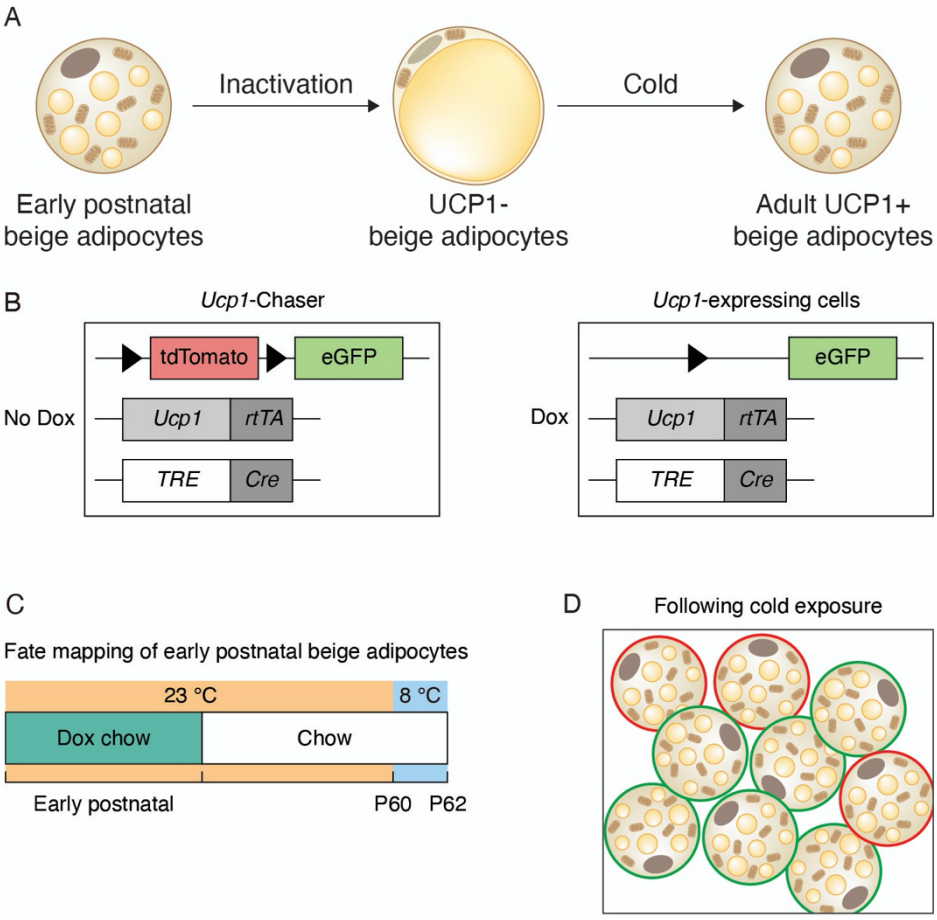

Figure 4.3 Fate mapping of early postnatal beige adipocytes with *Ucp1*-Chaser.
(**A**) Schematic representation of the link between early postnatal and adult beige adipocytes. (**B**) Schematic of the genetic components of the *Ucp1*-Chaser mouse model. These mice carry ROSA$^{mT/mG}$, *Ucp1*^{rtTA}, and *TRE-Cre*. Left panel: Without doxycycline treatment, membrane-targeted tdTomato is expressed in all cells in mice. Right panel: When treated with doxycycline, Cre recombinase becomes present in *Ucp1*-expressing cells, deleting the tdTomato cassette flanked between the two loxP sites and allowing expression of membrane-targeted eGFP. (**C**) *Ucp1*-Chaser mice housed at RT (23 °C) were fed a doxycycline-containing chow diet during early postnatal development and then kept on a regular chow diet until maturity (8-9 weeks of age). These mice were then exposed to cold (8 °C) for 2 days to induce adult beige adipocyte biogenesis. (**D**) Following cold exposure in adult mice, UCP1+ adipocytes with membrane-labeled GFP come from early postnatal beige adipocytes.

To test the link between early postnatal and adult beige adipocytes, we generated a tetracycline-dependent mouse model that allows fate mapping of early postnatal beige adipocytes (*Ucp1*^{rtTA}; *TRE-Cre*; ROSA$^{mT/mG}$; hereafter noted as *Ucp1*-Chaser mice) (**Figure 4.3 B**). In this model, all cells in mice are labeled with cell-membrane localized tdTomato, a red fluorescent protein. Upon doxycycline treatment, *Ucp1*-expressing cells will have the tdTomato cassette permanently replaced by an eGFP (enhanced green fluorescent protein) cassette, and therefore labeled with cell-membrane targeted GFP (**Figure 4.3 B**). To label early postnatal beige adipocytes, *Ucp1*-Chaser mice were treated with a doxycycline-containing chow diet during the early postnatal period, and then kept on a standard chow diet until maturity. These mice were next exposed to cold for 2 days to induce beige adipocyte recruitment during adulthood (**Figure 4.3 C**). If early postnatal beige adipocytes contribute to adult beige adipocyte recruitment, we expect to find cells that are simultaneously labeled with both UCP1 and GFP (**Figure 4.3 D**).

Following the fate-mapping procedure, we analyzed the presence of GFP-labeled UCP1+ adipocytes in iWAT with imaging. Consistent with our previous observations, strong beige adipocyte biogenesis occurred in the inguinal region after two days of cold exposure (**Figure 4.4 B and D**), while only small clusters of active beige adipocytes were found in the dorsomedial region (**Figure 4.4 A and C**). Interestingly, a large proportion of the UCP1+ adipocytes were also labeled with membrane-localized GFP (**Figure 4.4 E-K**). These data strongly support that a significant proportion of adult beige adipocytes come from early postnatal beige adipocytes.

Moreover, our previous experiments with perinatal deletion of *Prdm16* further support this link. When early postnatal beige adipocytes failed to develop normally in the absence of *Prdm16*, cold-induced upregulation of thermogenic adipocyte markers was almost completely blocked in adult mice (**Figure 3.8 and 3.10**), suggesting impaired adult beige adipocyte recruitment. Together with the fate mapping experiment, these data strongly support that early postnatal beige adipocytes significantly contribute to adult cold-induced beige adipocyte biogenesis. Additional experiments will be carried out to further investigate the origin and fate of the early postnatal beige adipocytes (see **4.6** for more discussion).

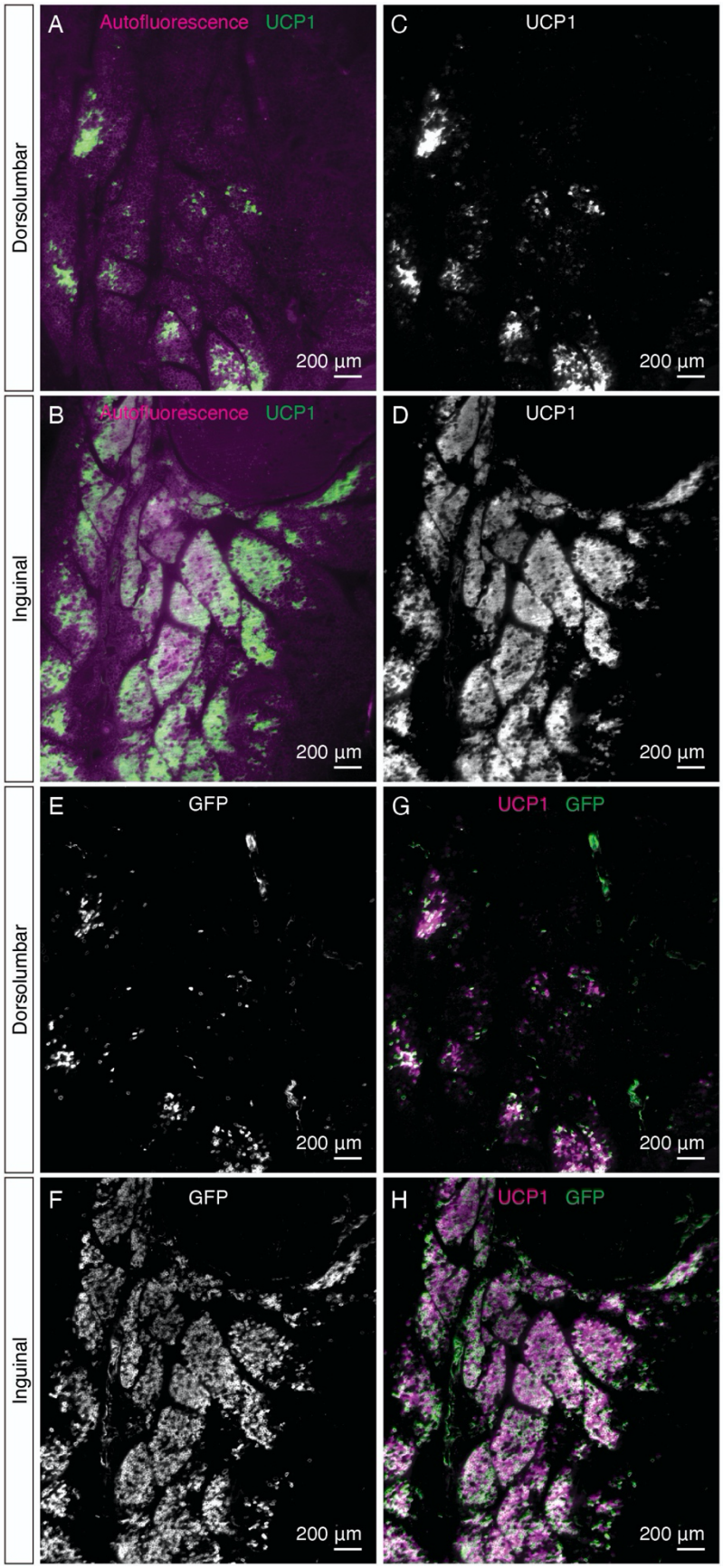
Dorsolumbar
A
Autofluorescence
UCP1
200 µm
C
UCP1
200 µm
Inguinal
B
Autofluorescence
UCP1
200 µm
D
UCP1
200 µm
Dorsolumbar
E
GFP
200 µm
G
UCP1
GFP
200 µm
Inguinal
F
GFP
200 µm
H
UCP1
GFP
200 µm

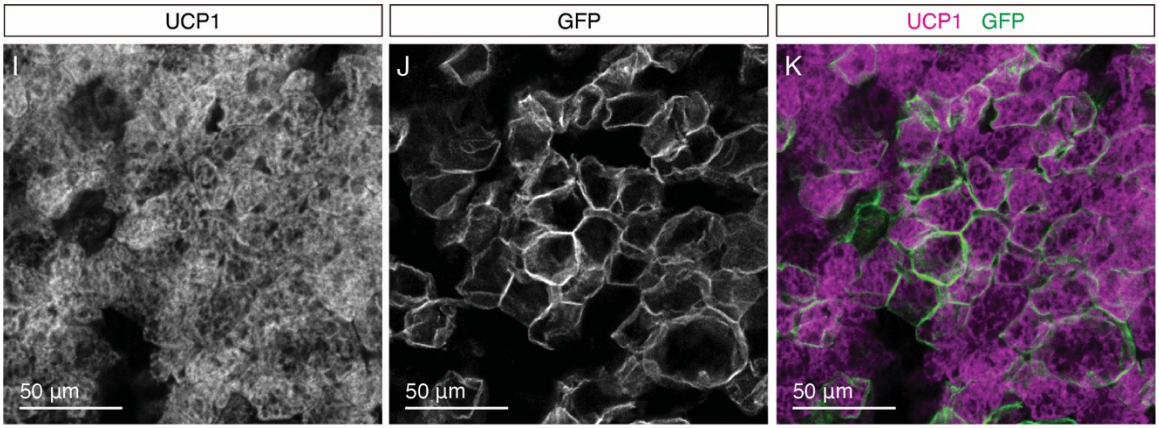

Figure 4.4 The link between early postnatal and adult beige adipocytes.
Ucp1-Chaser mice were treated with doxycycline from P21 until P28 and exposed to 8°C for 2 days at 9-week-old. (**A-H**) Representative whole-tissue optical sections of iWAT immunostained with UCP1 and GFP. (**A-B**) Overlay of autofluorescence (magenta) and UCP (green). (**C-D**) UCP1. (**E-F**) GFP. (**G-H**) Overlay of UCP1 (magenta) and GFP (green). (**A, C, E, and G**) Images of the dorsolumbar region. (**B, D, F, and H**) Images of the inguinal region. (**I-K**) Confocal images of lobules containing UCP1+ adipocytes in the inguinal region. (**I**) UCP1. (**J**) GFP. (**K**) Overlay of UCP1 (magenta) and GFP (green).

4.4 Investigating the cause of early postnatal beige adipogenesis

4.4.1 Distinct adipocyte progenitor cells may contribute to early postnatal beige adipogenesis

We next wondered what the driver of early postnatal beige adipocytes could be. Adult beige adipocytes can arise from distinct beige progenitor cells or from existing mature adipocytes (Shao et al., 2019). If early postnatal beige adipocytes come from unique adipocyte progenitor cells (APCs), we should expect enrichment of beige APCs in the inguinal region relative to the dorsolumbar region. To test this possibility, we isolated crude APCs from the inguinal and dorsolumbar regions of iWAT and studied them *in vitro*. Specifically, we dissociated cells from the two iWAT regions of young mice, separated lipid-laden adipocytes from the stromal vascular fraction (APCs, immune cells, and fibroblasts) by centrifugation, and grew the stromal vascular cells with culture medium that supports proliferation and maintenance of APCs (see **Chapter 5.4** for details). Upon treatment with an adipogenic cocktail, the crude APCs gradually differentiated into lipid-laden mature adipocytes *in vitro* (**Figure 4.5 A**). We collected cells from various differentiation dates and analyzed their gene expression patterns. Although the progenitor cells from the two regions became equally differentiated (**Figure 4.5 B**), we observed a robust regional difference in thermogenic adipocyte markers where higher *Ucp1* and *Prdm16* mRNA levels were found in the inguinal region at several time points (**Figure 4.5 C**). As cells growing in a dish are no longer supported by their native microenvironment, these results strongly support that APCs isolated from the inguinal region exhibit unique intrinsic properties, which allow them to differentiate into mature adipocytes that express higher levels of thermogenic genes.

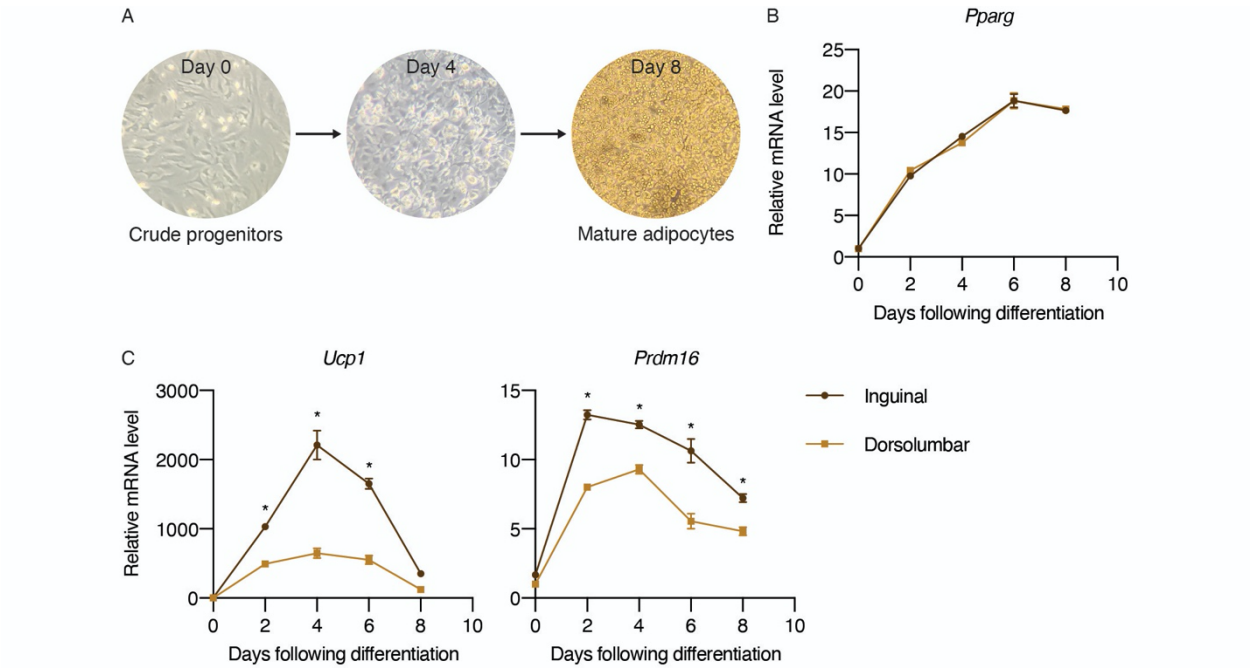

Figure 4.5 Beige adipocyte progenitor cells are more enriched in the inguinal region of iWAT.

(**A**) Cell morphology at day 0, 4, and 8 following differentiation. An adipogenic cocktail was added on day 0. (**B-C**) Normalized gene expression of cells from dorsolumbar vs. inguinal regions of iWAT from young C57BL6/J mice, n=3. (**B**) Representative adipogenic marker: *Pparg*. (**C**) Representative thermogenic markers: *Ucp1* and *Prdm16*. Data are presented as mean ± SEM and analyzed by two-way ANOVA followed by Bonferroni's multiple comparisons test. * denotes $p<0.05$ dorsolumbar vs. inguinal region at each time point.

4.4.2 Early postnatal beige adipocyte development does not require sympathetic activation

As beige adipocyte recruitment in adult iWAT is triggered by extrinsic factors such as sympathetic stimulation, it is possible that early postnatal beige adipocytes arise as a result of cold-induced sympathetic stimulation. Room temperature (23°C) is considered a mild cold stress to mice, particularly in developing animals that do not have their adult fur pattern. We found that when mice were born and raised at a warmer temperature (30°C), at which cold-induced sympathetic firing is minimized, early postnatal beige adipocytes arise in iWAT with the same patterning as that of room temperature-housed mice (**Figure 4.6 A-B**). In addition, mRNA analysis of *Ucp1* transcripts revealed a developing pattern in 30°C-housed mice that is similar to RT-housed mice (**Figure 4.6 C**). Importantly, a recent study using genetic sympathetic ablation showed that early postnatal beige adipocytes develop normally in the absence of sympathetic innervation (Wu et al., 2020b). Together, these data suggest that the development of beige adipocytes is not through sympathetic activation, but likely based on a developmentally hard-wired program.

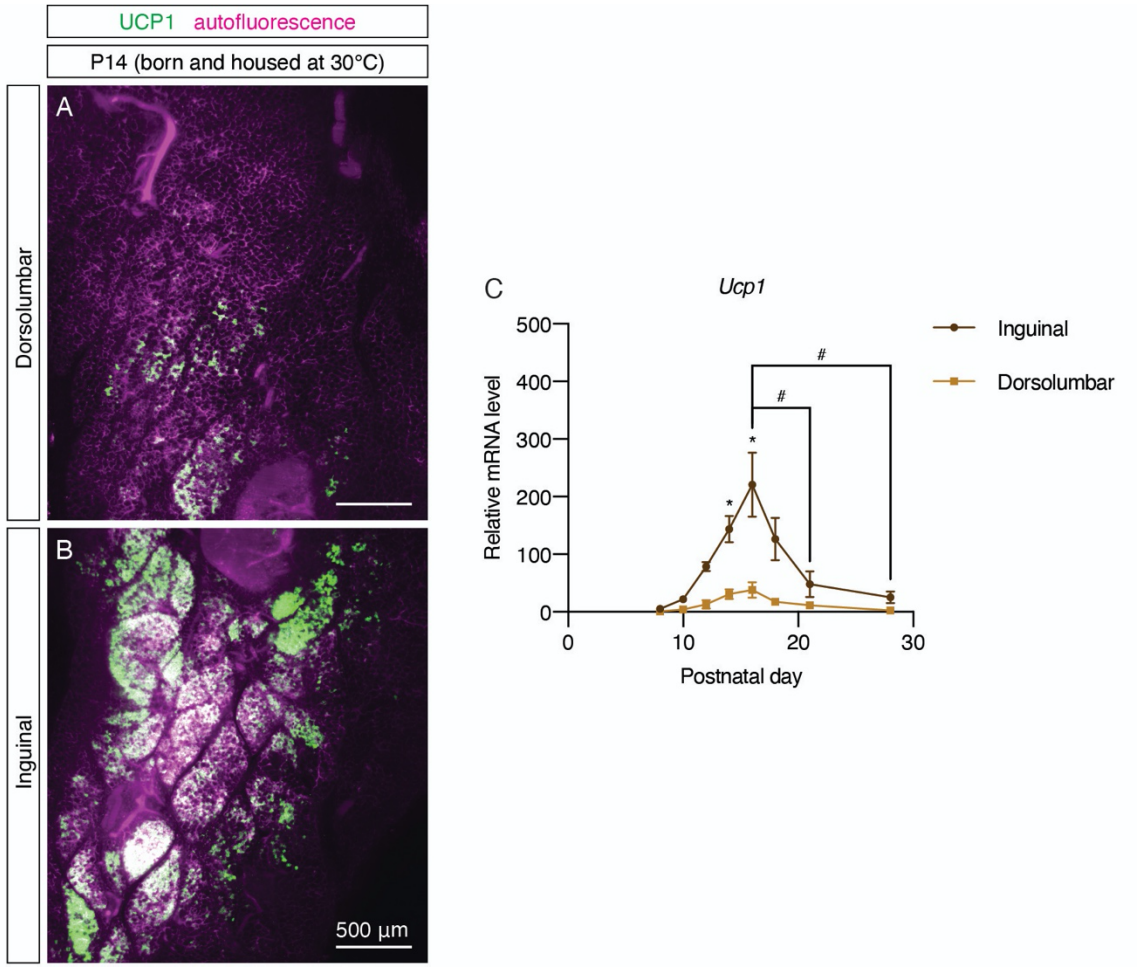

Figure 4.6 Early postnatal beige adipocytes develop normally regardless of housing temperatures.

iWAT samples collected from P8, P10, P12, P14, P16, P18, P21, and P28 C57BL6/J mice born and housed at 30 °C were used for imaging and mRNA analysis. (**A-B**) High-magnification MIPs of 20 µm z-stacks from iWAT of a P14 mouse (30 °C). UCP1 (green) and autofluroescence (magenta) channels are shown. (**A**) Image of the dorsolumbar region. (**B**) Image of the inguinal region. Scale bars are indicated. (**C**) Normalized *Ucp1* expression, n=2-4. Data are presented as mean ± SEM and analyzed by two-way ANOVA followed by Bonferroni's multiple comparisons test. * denotes $p<0.05$ dorsolumbar vs. inguinal region at each time point. # denotes $p<0.05$ inguinal region at P16 in comparison to inguinal regions at other time points.

4.4.3 Blood and lymph vessels may contribute to early postnatal beige adipocyte formation

Besides sympathetic activation, beige adipocyte recruitment during adulthood has been shown to be regulated by other adipose tissue components such as immune cells and the vasculature (Brestoff et al., 2014; Sun et al., 2012). We next examined the location of additional tissue structures such as the blood and lymph vessels in relation to beige adipocytes. As we observed that UCP1+ adipocytes originated from the center of the inguinal region (P6-P10) and then gradually radiated to the entire region (P14-P28), we particularly focused on tissue structures located in this core region.

We have previously noted the presence of several vessels traversing the core of the inguinal region by CD31 staining (**Figure 3.3**). Since CD31 labels endothelial cells that line both blood and lymph vessels, we opted for markers that can distinguish the two structures. We labeled lymph vessels with an antibody targeting lymphatic vessel endothelial hyaluronan receptor 1 (LYVE1), a well-recognized marker for lymphatic endothelial cells in various tissue types (Podgrabinska et al., 2002; Potente and Mäkinen, 2017). In addition to the lymph node, we observed that LYVE1 staining revealed cell-like and vessel-like structures in iWAT (**Figure 4.7 A, D, and E**). The LYVE1+ vessel originating from the lymph node is likely a lymph vessel. Importantly, this vessel lies adjacent to the main blood vessel that is heavily innervated by TH+ fibers and travels through the center of the inguinal region (**Figure 4.7 B-E**). It is likely that the blood and lymph vessels in this region may be associated with beige APCs or elaborate factors to drive early beige adipocyte formation. Further experiments that manipulate blood and lymph vessel-associated cell types within adipose tissue will be needed to assess their role in the development of early postnatal beige adipocyte.

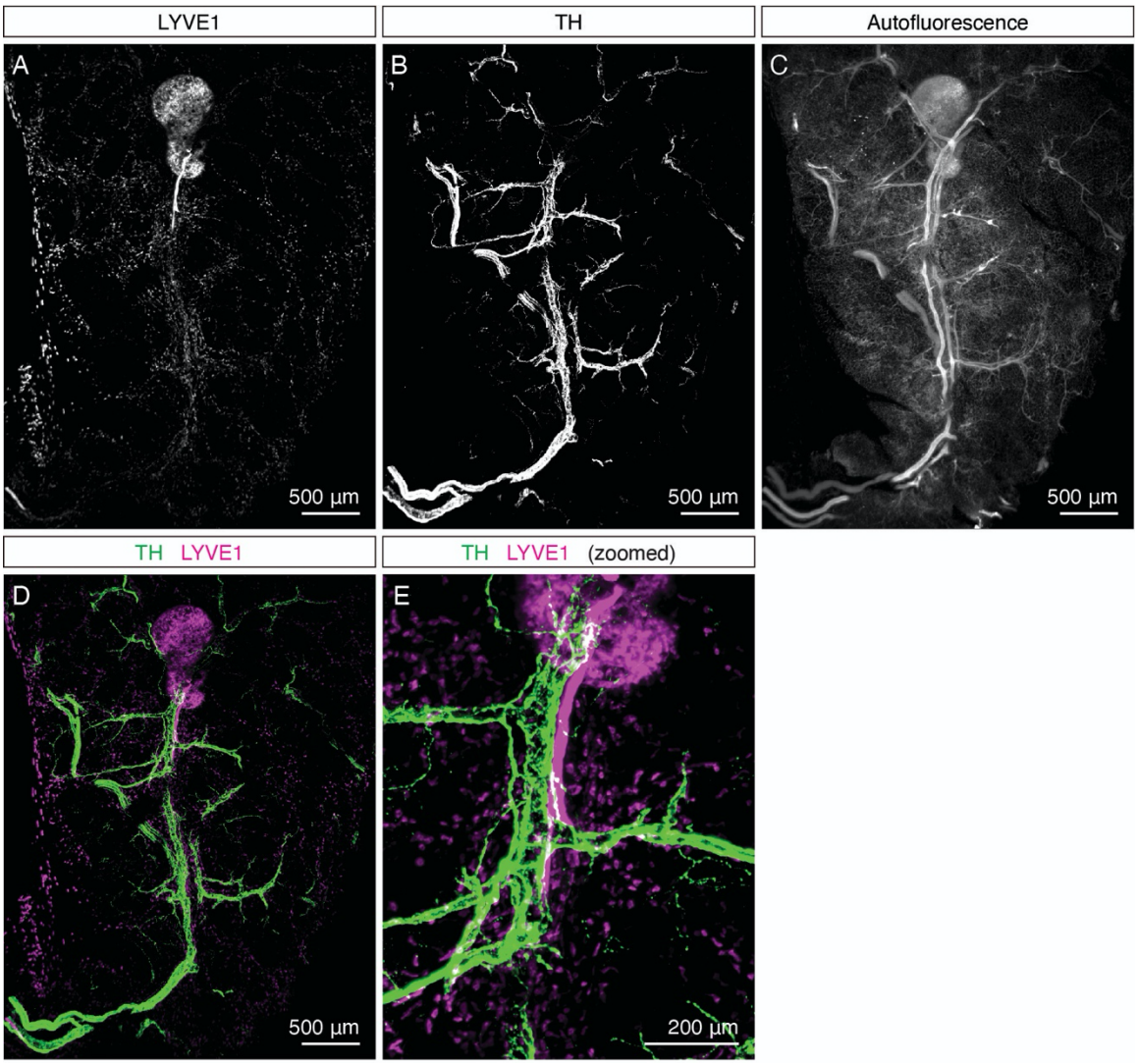

Figure 4.7 Localization of lymph and blood vessels in the inguinal region of iWAT.
(**A-E**) Representative of iWAT from a P8 C57BL6/J mouse immunolabeled with LYVE1 (magenta) and TH (green). MIPs of 50 µm z-stacks are shown. (**A**) LYVE1. (**B**) TH. (**C**) autofluorescence. (**D**) Overlay of TH (green) and LYVE1 (magenta). (**E**) Zoomed-in view of the peri-lymph node region in **D**.

4.5 Discussion and future directions

Our studies have carefully characterized beige adipocyte biogenesis at various developmental stages using whole-tissue imaging and molecular analysis. In addition to the well-studied adult beige adipocytes that appear upon β-adrenergic stimulation, we and others have recently described UCP1+ beige adipocytes that develop independently of sympathetic stimulation during the early postnatal period (Chi et al., 2021; Wu et al., 2020b). The remarkable similarities between the distribution patterns of early postnatal and adult beige adipocytes led us to hypothesize that the two beige adipocyte populations may be of the same identity. We further performed fate mapping studies to demonstrate that early postnatal beige adipocytes indeed greatly contribute to adult beige adipocytes upon short cold exposure. In addition, the thermogenic gene expression of early postnatal beige adipocytes diminishes as mice mature. It is possible that early postnatal beige adipocytes gradually become inactivated during maturation, and cold challenge re-activates the same cells in adult mice.

Based on these observations, we developed a new model to explain the cellular origins of beige adipocytes (**Figure 4.8**). The inguinal region of iWAT primarily recruits beige adipocytes through **mode A** (**Figure 4.8**). Specifically, early postnatal beige adipocytes arise from distinct progenitor cells during early tissue morphogenesis. As mice mature, these beige adipocytes gradually become dormant by losing their thermogenic gene expression and appearing unilocular. Although these dormant beige adipocytes appear indistinguishable from mature white adipocytes in cell morphology, they still retain their identity as beige adipocytes and can readily be activated by short β-adrenergic stimulation (i.e., two days of cold exposure).

The phenomenon that beige adipocytes arise from conversion of existing white adipocytes (Lee et al., 2015; Shao et al., 2019; Wang et al., 2013) may instead have been due to the reactivation of dormant beige adipocytes. *Adipoq*-based fate-mapping models label all mature adipocytes but cannot distinguish white vs. dormant beige adipocytes. Our studies using *Ucp1*-promoter-driven fate-mapping allowed more precise tracing of cells that were once UCP1+ beige adipocytes. Together, these fate-mapping studies strongly support that a significant proportion of adult beige adipocytes arise from dormant beige adipocytes that were born during early postnatal period.

β-adrenergic signaling also occurs in adipocyte progenitor cells that reside in adult iWAT upon cold exposure (Jiang et al., 2017b). These cells can then differentiate into new beige adipocytes (**Figure 4.8**). However, *de novo* differentiation process likely takes more time than does reactivation of existing mature adipocytes. It is possible that the contribution of newly born beige adipocytes will become greater as time progresses. It is worth noting that beige adipocyte formation in the dorsomedial region was not obvious until prolonged cold exposure (i.e., seven days of cold treatment) (**Figure 2.5**). Future studies will examine the contribution of *de novo* adipogenesis over time within various iWAT regions. We will particularly focus on examining whether recruitment of beige adipocytes in the dorsomedial region primarily relies on **mode B** (**Figure 4.8**).

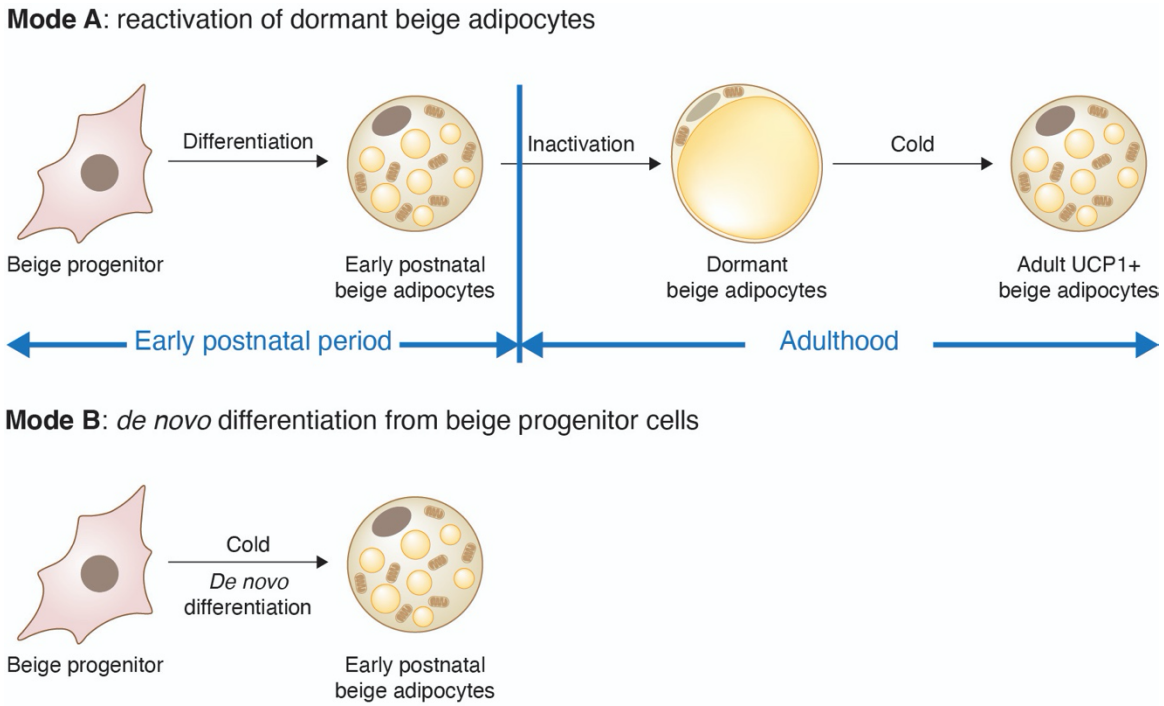

Figure 4.8 A new model for beige adipocyte formation in iWAT.
Mode A illustrates reactivation of dormant beige adipocytes derived from early postnatal beige adipocytes. Mode B illustrates *de novo* differentiation from beige progenitor cells.

Moreover, our *in vitro* studies revealed that beige adipocyte progenitors are likely more enriched in the inguinal region than the dorsolumbar region in developing fat pads. We will perform single cell RNA sequencing from cells isolated from the two iWAT regions to identify beige progenitor cells. We will analyze the distribution of the progenitor cells in relation to the core inguinal region where beige adipocytes first emerge using whole-tissue imaging. Lineage tracing from various progenitor cell populations will allow us to assess the contribution of each population. We will also examine whether the same cell types remain in adult iWAT and how they contribute to adult beige adipogenesis.

Lastly, it will be of great interest to investigate the mechanism underlying the inactivation of early postnatal beige adipocytes. Previous studies have taken cold-exposed adult mice to warm temperatures and described progressive "whitening" of adult beige adipocytes (Altshuler-Keylin et al., 2016; Roh et al., 2018; Rosenwald et al., 2013). The beige-to-white transition has been found to be mediated by a transcription factor ZFP423 (Roh et al., 2018) and autophagy-dependent mitochondria clearance (Altshuler-Keylin et al., 2016). Interestingly, "whitened" beige adipocytes were found to retain epigenetic memory of prior cold exposure, which facilitates rapid reactivation in response to subsequent cold exposure (Roh et al., 2018). Future studies will investigate whether inactivation of early postnatal beige adipocytes occurs through similar mechanisms, and what triggers the upregulation of ZFP423 or mitochondria clearance. A better understanding of the inactivation mechanism may allow development of strategies to prevent beige adipocytes from being dormant.

4.6 Conclusion

Overall, whole-tissue 3D imaging provided us with a holistic view of adipose tissue architecture and allowed us to uncover strong heterogeneity in mouse inguinal subcutaneous fat. We exploited the heterogeneity in beige adipocyte distribution and sympathetic innervation to unravel the interaction between the two structures. Our findings that beige adipocytes guide sympathetic innervation establishment during a critical period will provide a framework for further mechanistic studies and development of therapeutic targets. Our developmental and fate mapping studies revealed an unprecedented link between early postnatal and adult beige adipocytes. Together with our future experiments, this insight has the potential to clarify the origin and fate of beige adipocytes. This fundamental knowledge may offer more effective means to enhance the thermogenic capacity of beige adipocytes, and therefore provide new opportunities for obesity treatment.

CHAPTER 5. Materials and Methods
5.1 Adipo-Clear

Adipo-Clear for whole-mount adipose tissue

Sample collection: Mice were heavily anesthetized with an overdose of isofluorane and an intracardiac perfusion and fixation was performed with 1xPBS followed by 4% PFA. All harvested samples were post-fixed in 4% PFA at 4°C overnight. Fixed samples were washed in PBS for 1 hour three times.

Delipidation and permeabilization: Fixed samples were washed in 20%, 40%, 60%, 80% methanol in H_2O/0.1% Triton X-100/0.3 M glycine (B1N buffer, pH 7-7.4), and 100% methanol for 30 min each. Sample were then delipidated with 100% dichloromethane (DCM; Sigma-Aldrich) for 30 min three times. After delipidation, samples were washed in 100% methanol for 30 min twice, then in 80%, 60%, 40%, 20% methanol in B1N buffer for 30 min each step. All procedures above were carried out at 4°C with shaking. Samples were then washed in B1N for 30 min twice followed by PBS/0.1% Triton X-100/0.05% Tween 20/2μg/ml heparin (PTwH buffer) for 1hr twice before further staining procedures.

Immunolabeling: Samples were incubated in primary antibody dilutions in PTxwH for 4 days. After primary antibody incubation, samples were washed in PTxwH for 5 min, 10 min, 15 min, 30 min, 1 hr, 2 hr, 4 hr, and overnight, and then incubated in secondary antibody dilutions in PTxwH for 4 days. Samples were finally washed in PTwH for 5 min, 10 min, 15 min, 30 min, 1 hr, 2 hr, 4 hr, and overnight. See **Table 5.1** for primary and secondary antibodies.

Tissue Clearing: Samples were embedded in 1% agarose in PBS, and then dehydrated in 25%, 50%, 75%, 100%, 100% methanol/H_2O series for 30 min at each step at RT. Following dehydration, samples were washed with 100% DCM for 1 hour three times, followed by an overnight clearing step in benzyl ether (DBE; Sigma-Aldrich). Samples were switched to fresh DBE and stored at RT in the dark until imaging.

A detailed Adipo-Clear protocol is published on JoVE (Chi et al., 2018b).

Immunostaining using delipidated cryo-sections

Adipose samples were dissected from mice perfused and fixed with 1x PBS followed by 4% PFA. Harvested samples were post-fixed in 4% PFA at 4 °C overnight and subsequently washed with 1x PBS for 1 hr at RT three times. Samples were then delipidated and permeabilized as described above. Fully delipidated samples were incubated in 25% sucrose/PBS solution for 2 hours until sinking, and then frozen in Tissue-Tek O.C.T Compound (Sakura Finetek USA, 4583). Frozen samples were sectioned into thick slices (40 μm for iBAT and 50-100 μm for iWAT or eWAT) using a Leica CM3050 S cryostat. Cryo-sections were blocked with PBS/0.1% Triton X-100/0.05% Tween 20/2 μg/ml heparin (PtxwH buffer) containing 3% donkey serum for 1 hour at RT, and then incubated with primary antibodies diluted in PtxwH buffer at RT overnight. Samples were then rinsed in PtxwH buffer for 5 min, 10 min, and 30 min to remove unbound antibodies. Secondary antibodies diluted in PtxwH buffer were then applied to samples at RT for 4 hours. Samples were next rinsed with PtxwH buffer for 5 min, 10 min, and 30 min, followed by 1x PBS

for 10 min twice. Finally, samples were immersed in antifade mountant (ProLong Gold, ThermoFisher Scientific, P10144) and sealed with a coverslip.

Table 5.1 List of antibodies used in this study.

Antibody name	Source	Identifiers	Antibody concentration
anti-tyrosine hydroxylase (Rabbit polyclonal)	Millipore	Cat# AB152, RRID:AB_390204	IF(1:200)
anti-tyrosine hydroxylase (Sheep polyclonal)	Millipore	Cat# AB1542, RRID:AB_90755	IF(1:200)
anti-CD31/PECAM-1 (Goat polyclonal)	R&D Systems	Cat# AF3628, RRID:AB_2161028	IF(1:200)
anti-UCP1 (Rabbit polyclonal)	Abcam	Cat# ab10983, RRID:AB_2241462	IF(1:200)
anti-CD68 (Rat monoclonal)	Bio-Rad	Cat# MCA1957, RRID:AB_322219	IF(1:400)
anti-LYVE1 (Rabbit polyclonal)	Abcam	Cat# ab14917, RRID:AB_301509	IF(1:200)
anti-PRDM16 (Sheep polyclonal)	R&D Systems	Cat# AF6295, RRID:AB_10717965	WB(1:500)
anti-Lamin A/C (Mouse monoclonal)	Santa Cruz Biotechnology	Cat# sc-376248, RRID:AB_10991536	WB(1:2000)
anti-Rabbit IgG (H+L), Alexa Fluor 568 (Donkey polyclonal)	Thermo Fisher Scientific	Cat# A10042, RRID:AB_2534017	IF(1:200)
anti-Rabbit IgG (H+L), Alexa Fluor 647 (Donkey polyclonal)	Thermo Fisher Scientific	Cat# A32795, RRID:AB_2762835	IF(1:200)
anti-Sheep IgG (H+L), Alexa Fluor 647 (Donkey polyclonal)	Thermo Fisher Scientific	Cat# A-21448, RRID:AB_2535865	IF(1:200)
anti-Goat IgG (H+L), Alexa Fluor 568 (Donkey polyclonal)	Thermo Fisher Scientific	Cat# A-11057, RRID:AB_2534104	IF(1:200)

5.2 Imaging and processing

Imaging

Whole-tissue iWAT samples were all imaged on a light sheet microscope (Ultramiscroscope II, LaVision Biotec) equipped with 1.3X and 4X objective lenses and an sCMOs camera (Andor Neo). Images were acquired with the ImspectorPro software (LaVision BioTec). Samples were positioned in an imaging chamber filled with DBE and illuminated from one side by the laser light sheet with 488, 561, and 640 nm laser channels. Samples were scanned at a step-size of 4-5 μm for the 1.3x objective and 2.5-3 μm for the 4x objective. Fluorescently labeled cryo-sections were imaged on an inverted LSM 880 NLO laser scanning confocal and multiphoton microscope (Zeiss) with a 20X lens (NA 0.8).

Image Processing

All images and videos were generated using Imaris software (Bitplane). 3D tissue reconstruction was generated using the "Volume" function. Maximum intensity projections and optical slices were obtained using the "Ortho Slicer" function. All images were captured using the "Snapshot" tool, while all videos were made using the "Animation" tool.

5.3 Sympathetic parenchymal neurite quantification and adipocyte size estimation

Various regions of iWAT were imaged with the 4X objective lens on the light sheet microscope. In each 3D image, we randomly isolated small cuboidal volumes (4-8 volumes per sample) that were completely contained within lobules using the "Surfaces" tool followed by the mask channel option of Imaris (**Figure 5.1 A-B**). Volumes of the isolated segments were automatically generated by "Surfaces". To sample parenchymal neurites, we avoided placing volumes in areas that contain nerve bundles or blood vessel innervation. Using the "Filament" tool, we computationally reconstructed parenchymal neurites by automatically tracing the TH signal and calculated the total neurite length within each volume (**Figure 5.1 C-D**). We presented the ratio of total neurite length (μm) by regional volume (μm^3) as neurite density within a volume (**Figure 5.1 F, upper panel**). To adjust for adipocyte size/number, we manually counted adipocyte number as shown by the tissue autofluorescence signal from multiple representative slices within each volume. The average adipocyte number per slice was then multiplied by the height (z depth) of that volume to generate a factor representing adipocyte density (**Figure 5.1 E**). The ratio of total neurite length (μm) by adipocyte density (arbitrary unit) is presented (**Figure 5.1 F, bottom panel**). To estimate adipocyte area, area of each representative slice was divided by the corresponding adipocyte number. This ratio is averaged across all representative slices within a cuboid, and the average is taken as mean adipocyte area (μm^2) of that cuboid.

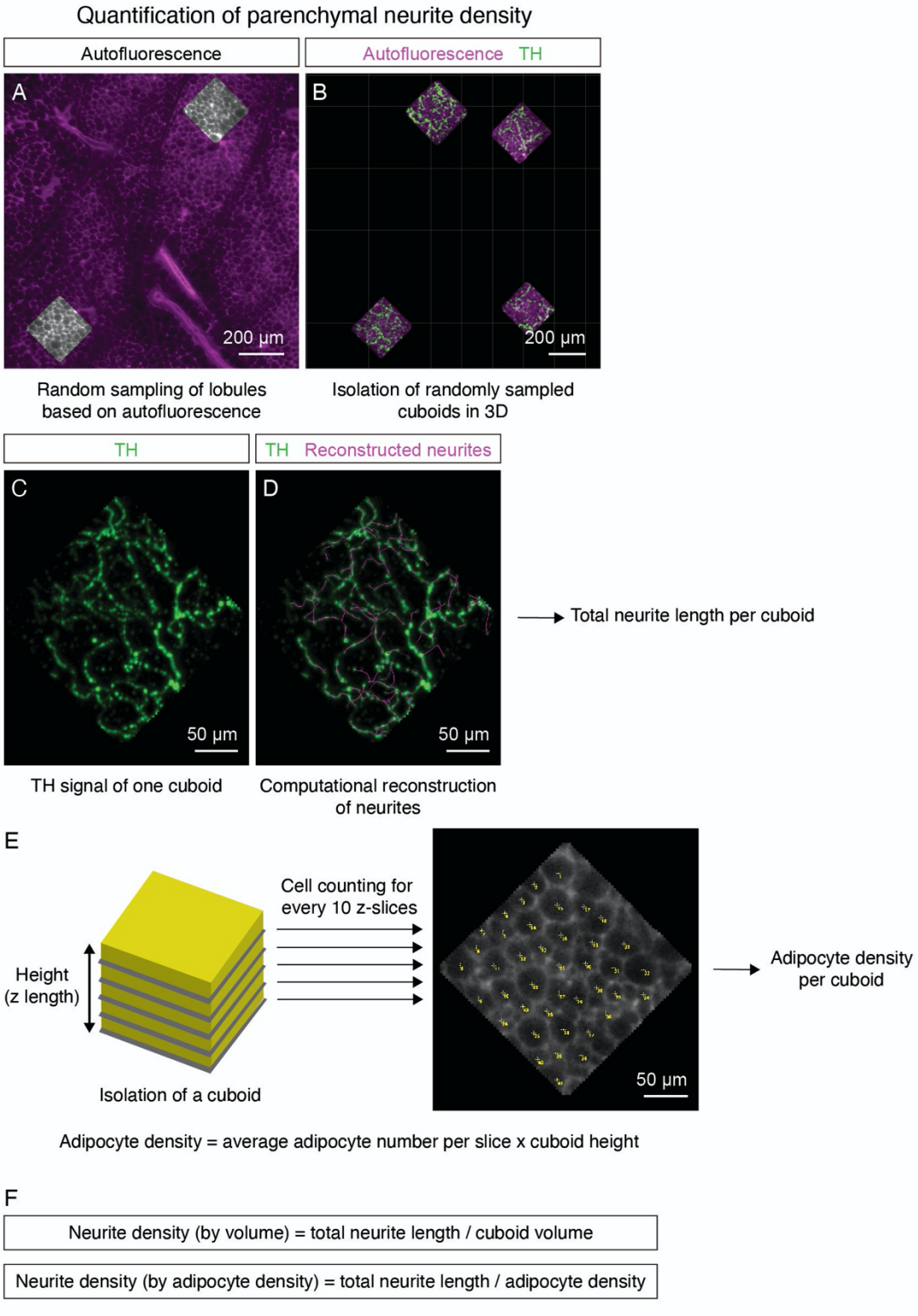
Quantification of parenchymal neurite density
Autofluorescence
Autofluorescence TH
A
B
200 µm
200 µm
Random sampling of lobules based on autofluorescence
Isolation of randomly sampled cuboids in 3D
TH
TH Reconstructed neurites
C
D
50 µm
50 µm
Total neurite length per cuboid
TH signal of one cuboid
Computational reconstruction of neurites
E
Cell counting for every 10 z-slices
Height (z length)
Isolation of a cuboid
50 µm
Adipocyte density per cuboid
Adipocyte density = average adipocyte number per slice x cuboid height
F
Neurite density (by volume) = total neurite length / cuboid volume
Neurite density (by adipocyte density) = total neurite length / adipocyte density

Figure 5.1 Neurite density quantification in 3D images.
Illustration of sympathetic parenchymal neurite density quantification with random sampling and filament tracing. (**A**) In each 3D image, small squares contained within lobules are randomly selected based on tissue autofluorescence using Surfaces in Imaris. (**B**) Randomly selected squares are then reconstructed into cuboids to represent volumes in the specific lobules. Specific channels within cuboids were generated by using Mask option in Imaris. (**C-D**) Computational reconstruction of TH signal to obtain total neurite length in individual cuboids using Filament in Imaris. (**C**) TH signal in one representative cuboid. (**D**) Overlay between reconstructed filaments (magenta) and TH signal (green). The total neurite length of each cuboid can be estimated by measuring the total length of the reconstructed filaments. (**E**) Adipocyte number is manually counted based on the tissue autofluorescence signal. Average count of every 10 slices (in the xy plane) within a cuboid is taken as average adipocyte number per slice. Adipocyte density is estimated by multiplying average adipocyte number per slice and cuboid height (z-length). (**F**) Neurite density normalized by volume is presented as the ratio of total neurite length (mm) by cuboid volume (mm^3). Neurite density normalized by adipocyte density is presented as the ratio of total neurite length (mm) by adipocyte density (arbitrary unit).

5.4 Other methods

Animals

Young wild-type mice of various ages were generated by crossing male and female mice from the C57BL/6J background (C57BL/6J, JAX 000664) obtained from the Jackson Laboratories and maintained in our facilities. The constitutive *Prdm16*^{KO} (c*Prdm16*^{KO}) mice were generated as previously described (Cohen et al., 2014) by crossing *Adipoq-Cre* mice (JAX 028020) with *Prdm16*$^{lox/lox}$ mice. The inducible *Prdm16*^{KO} (i*Prdm16*^{KO}) mice were generated by crossing *Adipoq-rtTA* (provided by Dr. Philipp E. Scherer) (Sun et al., 2012), *TRE-Cre* (JAX 006234), and *Prdm16*$^{lox/lox}$ mice. The *Ucp1*-Chaser mice were generated by crossing *Ucp1-rtTA* (provided by Dr. Philipp E. Scherer) (Sun et al., 2014), TRE-Cre, and ROSA$^{mT/mG}$ (JAX 007676) mice. All animals in this study were male mice on a pure C57BL/6J background.

All mice were maintained on a 12-hour light/dark cycle with free access to food and water. To generate mice born and raised at thermoneutrality, pregnant female mice were housed at 30 °C 14 days after vaginal plug formation until the pups reach the indicated ages. All other mice were housed at 23 °C. For perinatal *Prdm16* deletion, pregnant female mice were fed with a chow diet containing 600 mg/kg doxycycline (Bio-Serv, S4107) 14 days after vaginal plug formation until the pups reach P21. For adult *Prdm16* deletion, the inducible *Prdm16*^{KO} (Cre+ and Cre-) mice were placed on a doxycycline-containing chow diet for the indicated time. In the fate-mapping study, *Ucp1*-Chaser mice were placed on a doxycycline-containing chow diet for the indicated time. All other mice were fed with a standard rodent chow diet. For cold exposure experiments, mice were placed at 8°C for the indicated time with two mice in each cage. Animal care and experimentation were performed according to procedures approved by the Institutional Animal Care and Use Committee at the Rockefeller University.

iWAT regional dissection

Various regions of iWAT were dissected for qPCR or Western blot analyses as illustrated in **Figure 2.7**. After removal of the lymph node, the region between the bottom two dotted lines, guided by the entry of the main blood vessel in the inguinal portion and the upper boundary of the lymph node, was dissected as the inguinal region. The region from the upper boundary of the lymph node to the back was considered as the dorsolumbar region. When indicated, the dorsolumbar region was further divided into dorsomedial and dorsolateral regions by making a cut alongside the blood vessel that travel through the dorsolumbar region.

Primary adipocyte culture

Different regions of iWAT were finely minced and digested with collagenase D (10 mg/mL, Roche) and dispase II (2.4 units/mL; Roche) at 37°C for 40 min. After quenching of the digestion by adding equal volume of ice-cold growth medium (DMEM/F12 Glutamax medium containing 10% FBS and 1% Pen/Strep), the dissociated cells were filtered through a 100 μm sterile cell strainer to remove undigested tissue. The cell mixture was then spun at 500 x *g* at 4°C for 10 min to separate lipid-laden mature adipocytes and the stromal vascular fraction. The supernatant which contains floating mature adipocytes were aspirated and discarded, the stromal vascular cell-containing pellet was resuspended in fresh medium and passed through a 70 μm sterile cell strainer. Finally, cells were collected by centrifugation at 500 x *g* for 10 min and plated onto collagen-coated 12-well plates. When cells reached near confluence, adipogenic differentiation was carried

out in growth medium containing full adipogenic cocktail (1 μM dexamethasone (Sigma-Aldrich, D4902), 0.5 μM isobutylmethylxanthine (Sigma-Aldrich, I7018), 1 μM Rosiglitazone (Sigma-Aldrich, R2408), and 850 nM insulin (Sigma-Aldrich, I2643)). After two days of incubation in full adipogenic cocktail, cells were then incubated in medium containing 1 μM Rosiglitazone and 850 nM insulin. From day 4 of differentiation, cells were maintained in medium containing only 850 nM insulin. Medium was changed every two days. Cells were collected in TRIzol (Invitrogen) at the indicated time points for mRNA analysis.

Gene expression analysis

Total RNA was extracted from tissue or primary cells using TRIzol (Invitrogen) along with RNeasy kits (QIAGEN). An RNeasy mini kit was used for adult tissue samples, while an RNeasy micro kit was used for small tissue samples from young mice and primary cells. For qPCR analysis, RNA was reverse transcribed using the high-capacity cDNA reverse transcription kit (Applied Biosystems). cDNA was used in qPCR reactions containing SYBR-green fluorescent dye (Applied Biosystems). Relative mRNA expression was determined by normalization with *Tbp* (TATA-box binding protein) levels using the ΔΔCt method. The sequences of primers used in this study are listed in **Table 5.2**.

Nuclear extraction and immunoblotting

Frozen iWAT, eWAT, and iBAT were minced and homogenized in a hypotonic buffer (10mM HEPES, 10mM KCl, 1.5mM $MgCl_2$, 0.5mM DTT, and 1x protease inhibitor cocktail (cOmplete Mini, Roche)) by a dounce homogenizer. Homogenate was incubated on ice for 10 minutes and then mixed with 1/20 volume of 10% IGEPAL CA-630 (Sigma-Aldrich, I8896). Samples were then filtered through a 100 μm cell strainer and centrifuged at 1000 x g for 10 minutes. After centrifugation, lipid and cytoplasmic fractions were removed and nuclear pellets were resuspended in lysis buffer (20 mM HEPES, 1.5 mM $MgCl_2$, 0.42 M NaCl, 0.2mM EDTA, 0.5 mM DTT, 1x protease inhibitor cocktail, and 20% Glycerol). Samples were incubated on ice for 30 minutes and vortexed for 15 seconds every 10 minutes during the incubation. After lysis, samples were centrifuged at 20,000 x g for 10 minutes and the supernatant was taken as the nuclear extract. The following antibodies were used in immunoblotting: anti-PRDM16 (1:500, R&D systems, AF6295), anti-Lamin A/C (1:3000, Santa Cruz, sc-376248).

Statistical analysis

All statistical analyses were performed using GraphPad Prism (GraphPad Software, San Diego, CA, USA). For gene expression analysis, neurite density quantification, and body weight measurement, we estimated the approximate effect size based on independent preliminary studies. When indicated, an unpaired two-tailed Student's t test was used to analyze statistical differences. One-way and two-way ANOVA followed by Bonferroni's multiple comparisons test were applied to determine the statistical differences for the rest of the analyses. The statistical details for each experiment can be found in the figure legends. P values below 0.05 were considered significant throughout the studies.

Table 5.2 List of qPCR primers used in this study.

Gene	Forward 5'-3'	Reverse 5'-3'
Ucp1	ACT GCC ACA CCT CCA GTC ATT	CTT TGC CTC ACT CAG GAT TGG
Cox8b	GAA CCA TGA AGC CAA CGA CT	GCG AAG TTC ACA GTG GTT CC
Cidea	TGC TCT TCT GTA TCG CCC AGT	GCC GTG TTA AGG AAT CTG CTG
Dio2	CAG TGT GGT GCA CGT CTC CAA TC	TGA ACC AAA GTT GAC CAC CAG
Elovl3	TCC GCG TTC TCA TGT AGG TCT	GGA CCT GAT GCA ACC CTA TGA
Prdm16	GAC TTG GAC ACT ACC ACG GG	AGA TGC ACC CCC AAA CTC AG
Ppargc1a	CCC TGC CAT TGT TAA GAC C	TGC TGC TGT TCC TGT TTT C
Cebpb	TCG AAC CCG CGG ACT GCA AG	CGA CGA CGA CGT GGA CAG GC
Fabp4	ACA CCG AGA TTT CCT TCA AAC TG	CCA TCT AGG GTT ATG ATG CTC TTC A
Pparg	GTG CCA GTT TCG ATC CGT AGA	GGC CAG CAT CGT GTA GAT GA
Adipoq	GCA CTG GCA AGT TCT ACT GCA A	GTA GGT GAA GAG AAC GGC CTT GT
S100b	CAC CCG AAG AGG TTG CTC AT	GGA AGG GTG TAG GCG ATC AG
Tgfb1	GGA GAG CCC TGG ATA CCA ACT	TGT GTG TCC AGG CTC CAA AT
Tbp	GGGTATCTGCTGGCGGTTT	TGAAATAGTGATGCTGGGCACT

References

Abe, H., Tani, T., Mashiko, H., Kitamura, N., Miyakawa, N., Mimura, K., Sakai, K., Suzuki, W., Kurotani, T., Mizukami, H., et al. (2017). 3D reconstruction of brain section images for creating axonal projection maps in marmosets. J. Neurosci. Methods *286*, 102–113.

Ahima, R.S., Prabakaran, D., and Flier, J.S. (1998). Postnatal leptin surge and regulation of circadian rhythm of leptin by feeding. Implications for energy homeostasis and neuroendocrine function. J. Clin. Invest. *101*, 1020–1027.

Altshuler-Keylin, S., Shinoda, K., Hasegawa, Y., Ikeda, K., Hong, H., Kang, Q., Yang, Y., Perera, R.M., Debnath, J., and Kajimura, S. (2016). Beige Adipocyte Maintenance Is Regulated by Autophagy-Induced Mitochondrial Clearance. Cell Metab. *24*, 402–419.

Bachman, E.S., Dhillon, H., Zhang, C.-Y., Cinti, S., Bianco, A.C., Kobilka, B.K., and Lowell, B.B. (2002). βAR Signaling Required for Diet-Induced Thermogenesis and Obesity Resistance. Science *297*, 843–845.

Barbatelli, G., Murano, I., Madsen, L., Hao, Q., Jimenez, M., Kristiansen, K., Giacobino, J.P., Matteis, R.D., and Cinti, S. (2010). The emergence of cold-induced brown adipocytes in mouse white fat depots is determined predominantly by white to brown adipocyte transdifferentiation. Am. J. Physiol. - Endocrinol. Metab. *298*, E1244–E1253.

Bartness, T.J., Liu, Y., Shrestha, Y.B., and Ryu, V. (2014). Neural innervation of white adipose tissue and the control of lipolysis. Front. Neuroendocrinol. *35*, 473–493.

Becher, T., Palanisamy, S., Kramer, D.J., Eljalby, M., Marx, S.J., Wibmer, A.G., Butler, S.D., Jiang, C.S., Vaughan, R., Schöder, H., et al. (2021). Brown adipose tissue is associated with cardiometabolic health. Nat. Med. *27*, 58–65.

Berry, D.C., Jiang, Y., and Graff, J.M. (2016). Mouse strains to study cold-inducible beige progenitors and beige adipocyte formation and function. Nat. Commun. *7*, 10184.

Brestoff, J.R., Kim, B.S., Saenz, S.A., Stine, R.R., Monticelli, L.A., Sonnenberg, G.F., Thome, J.J., Farber, D.L., Lutfy, K., Seale, P., et al. (2014). Group 2 innate lymphoid cells promote beiging of white adipose tissue and limit obesity. Nature *519*, 242–246.

Burnstock, G. (2008). Non-synaptic transmission at autonomic neuroeffector junctions. Neurochem. Int. *52*, 14–25.

Cannon, B., and Nedergaard, J. (2004). Brown Adipose Tissue: Function and Physiological Significance. Physiol. Rev. *84*, 277–359.

CDC (2020a). Obesity is a Common, Serious, and Costly Disease.

CDC (2020b). Adult Obesity.

Chi, J., and Cohen, P. (2016). The Multifaceted Roles of PRDM16: Adipose Biology and Beyond. Trends Endocrinol. Metab. *27*, 11–23.

Chi, J., Crane, A., Wu, Z., and Cohen, P. (2018b). Adipo-Clear: A Tissue Clearing Method for Three-Dimensional Imaging of Adipose Tissue. JoVE J. Vis. Exp. e58271–e58271.

Chi, J., Wu, Z., Choi, C.H.J., Nguyen, L., Tegegne, S., Ackerman, S.E., Crane, A., Marchildon, F., Tessier-Lavigne, M., and Cohen, P. (2018a). Three-Dimensional Adipose Tissue Imaging Reveals Regional Variation in Beige Fat Biogenesis and PRDM16-Dependent Sympathetic Neurite Density. Cell Metab. *27*, 226-236.e3.

Chi, J., Lin, Z., Barr, W., Crane, A., Zhu, X.G., and Cohen, P. (2021). Early postnatal interactions between beige adipocytes and sympathetic neurites regulate innervation of subcutaneous fat. ELife *10*, e64693. The eLife article is distributed under the terms of Creative Commons Attribution License that permits unrestricted use and redistribution provided that the original author and source are credited.

Cohen, P., Levy, J.D., Zhang, Y., Frontini, A., Kolodin, D.P., Svensson, K.J., Lo, J.C., Zeng, X., Ye, L., Khandekar, M.J., et al. (2014). Ablation of PRDM16 and Beige Adipose Causes Metabolic Dysfunction and a Subcutaneous to Visceral Fat Switch. Cell *156*, 304–316.

Collaborators, T.G. 2015 O. (2017). Health Effects of Overweight and Obesity in 195 Countries over 25 Years. N. Engl. J. Med. *377*, 13–27.

Collins, S., Daniel, K.W., Petro, A.E., and Surwit, R.S. (1997). Strain-Specific Response toβ 3-Adrenergic Receptor Agonist Treatment of Diet-Induced Obesity in Mice1. Endocrinology *138*, 405–413.

Cypess, A.M., Lehman, S., Williams, G., Tal, I., Rodman, D., Goldfine, A.B., Kuo, F.C., Palmer, E.L., Tseng, Y.-H., Doria, A., et al. (2009). Identification and Importance of Brown Adipose Tissue in Adult Humans. N. Engl. J. Med. *360*, 1509–1517.

Dichamp, J., Barreau, C., Guissard, C., Carrière, A., Martinez, Y., Descombes, X., Pénicaud, L., Rouquette, J., Casteilla, L., Plouraboué, F., et al. (2019). 3D analysis of the whole subcutaneous adipose tissue reveals a complex spatial network of interconnected lobules with heterogeneous browning ability. Sci. Rep. *9*, 6684.

Gesta, S., Blüher, M., Yamamoto, Y., Norris, A.W., Berndt, J., Kralisch, S., Boucher, J., Lewis, C., and Kahn, C.R. (2006). Evidence for a role of developmental genes in the origin of obesity and body fat distribution. Proc. Natl. Acad. Sci. *103*, 6676–6681.

Gilsanz, V., Hu, H.H., and Kajimura, S. (2013). Relevance of brown adipose tissue in infancy and adolescence. Pediatr. Res. *73*, 3–9.

Glebova, N.O., and Ginty, D.D. (2005). Growth and Survival Signals Controlling Sympathetic Nervous System Development. Annu. Rev. Neurosci. *28*, 191–222.

Harms, M.J., Ishibashi, J., Wang, W., Lim, H.-W., Goyama, S., Sato, T., Kurokawa, M., Won, K.-J., and Seale, P. (2014). Prdm16 Is Required for the Maintenance of Brown Adipocyte Identity and Function in Adult Mice. Cell Metab. *19*, 593–604.

Harms, M.J., Lim, H.-W., Ho, Y., Shapira, S.N., Ishibashi, J., Rajakumari, S., Steger, D.J., Lazar, M.A., Won, K.-J., and Seale, P. (2015). PRDM16 binds MED1 and controls chromatin architecture to determine a brown fat transcriptional program. Genes Dev. *29*, 298–307.

Hill James O., Wyatt Holly R., and Peters John C. (2012). Energy Balance and Obesity. Circulation *126*, 126–132.

Holtmaat, A., and Svoboda, K. (2009). Experience-dependent structural synaptic plasticity in the mammalian brain. Nat. Rev. Neurosci. *10*, 647–658.

Hsieh, A.C.L., and Carlson, L.D. (1957). Role of Adrenaline and Noradrenaline in Chemical Regulation of Heat Production. Am. J. Physiol.-Leg. Content *190*, 243–246.

Hu, B., Jin, C., Zeng, X., Resch, J.M., Jedrychowski, M.P., Yang, Z., Desai, B.N., Banks, A.S., Lowell, B.B., Mathis, D., et al. (2020). γδ T cells and adipocyte IL-17RC control fat innervation and thermogenesis. Nature *578*, 610–614.

Huesing, C., Qualls-Creekmore, E., Lee, N., François, M., Torres, H., Zhang, R., Burk, D.H., Yu, S., Morrison, C.D., Berthoud, H., et al. (2020). Sympathetic innervation of inguinal white adipose tissue in the mouse. J. Comp. Neurol. cne.25031.

Iida, S., Chen, W., Nakadai, T., Ohkuma, Y., and Roeder, R.G. (2015). PRDM16 enhances nuclear receptor-dependent transcription of the brown fat-specific Ucp1 gene through interactions with Mediator subunit MED1. Genes Dev. *29*, 308–321.

Jespersen, N.Z., Larsen, T.J., Peijs, L., Daugaard, S., Homøe, P., Loft, A., de Jong, J., Mathur, N., Cannon, B., Nedergaard, J., et al. (2013). A Classical Brown Adipose Tissue mRNA Signature Partly Overlaps with Brite in the Supraclavicular Region of Adult Humans. Cell Metab. *17*, 798–805.

Jiang, H., Ding, X., Cao, Y., Wang, H., and Zeng, W. (2017a). Dense Intra-adipose Sympathetic Arborizations Are Essential for Cold-Induced Beiging of Mouse White Adipose Tissue. Cell Metab. *26*, 686-692.e3.

Jiang, Y., Berry, D.C., and Graff, J.M. (2017b). Distinct cellular and molecular mechanisms for β3 adrenergic receptor-induced beige adipocyte formation. ELife *6*, e30329.

Kajimura, S., Seale, P., Tomaru, T., Erdjument-Bromage, H., Cooper, M.P., Ruas, J.L., Chin, S., Tempst, P., Lazar, M.A., and Spiegelman, B.M. (2008). Regulation of the brown and white fat gene programs through a PRDM16/CtBP transcriptional complex. Genes Dev. *22*, 1397–1409.

Karemaker, J.M. (2017). An introduction into autonomic nervous function. Physiol. Meas. *38*, R89–R118.

Kopelman, P.G. (2000). Obesity as a medical problem. Nature *404*, 635–643.

Lee, P., Smith, S., Linderman, J., Courville, A.B., Brychta, R.J., Dieckmann, W., Werner, C.D., Chen, K.Y., and Celi, F.S. (2014). Temperature-Acclimated Brown Adipose Tissue Modulates Insulin Sensitivity in Humans. Diabetes *63*, 3686–3698.

Lee, Y.-H., Petkova, A.P., Konkar, A.A., and Granneman, J.G. (2015). Cellular origins of cold-induced brown adipocytes in adult mice. FASEB J. *29*, 286–299.

Long, J.Z., Svensson, K.J., Tsai, L., Zeng, X., Roh, H.C., Kong, X., Rao, R.R., Lou, J., Lokurkar, I., Baur, W., et al. (2014). A Smooth Muscle-Like Origin for Beige Adipocytes. Cell Metab. *19*, 810–820.

van Marken Lichtenbelt, W.D., Vanhommerig, J.W., Smulders, N.M., Drossaerts, J.M.A.F.L., Kemerink, G.J., Bouvy, N.D., Schrauwen, P., and Teule, G.J.J. (2009). Cold-Activated Brown Adipose Tissue in Healthy Men. N. Engl. J. Med. *360*, 1500–1508.

Molinoff, P.B., and Axelrod, J. (1971). Biochemistry of Catecholamines. Annu. Rev. Biochem. *40*, 465–500.

Morrison, S.F., Madden, C.J., and Tupone, D. (2014). Central Neural Regulation of Brown Adipose Tissue Thermogenesis and Energy Expenditure. Cell Metab. *19*, 741–756.

Murano, I., Barbatelli, G., Giordano, A., and Cinti, S. (2009). Noradrenergic parenchymal nerve fiber branching after cold acclimatisation correlates with brown adipocyte density in mouse adipose organ. J. Anat. *214*, 171–178.

Nam, J., Onitsuka, I., Hatch, J., Uchida, Y., Ray, S., Huang, S., Li, W., Zang, H., Ruiz-Lozano, P., and Mukouyama, Y. (2013). Coronary veins determine the pattern of sympathetic innervation in the developing heart. Development *140*, 1475–1485.

Nguyen, K.D., Qiu, Y., Cui, X., Goh, Y.P.S., Mwangi, J., David, T., Mukundan, L., Brombacher, F., Locksley, R.M., and Chawla, A. (2011). Alternatively activated macrophages produce catecholamines to sustain adaptive thermogenesis. Nature *480*, 104–108.

Ohno, H., Shinoda, K., Ohyama, K., Sharp, L.Z., and Kajimura, S. (2013). EHMT1 controls brown adipose cell fate and thermogenesis through the PRDM16 complex. Nature *504*, 163–167.

Orava, J., Nuutila, P., Lidell, M.E., Oikonen, V., Noponen, T., Viljanen, T., Scheinin, M., Taittonen, M., Niemi, T., Enerbäck, S., et al. (2011). Different metabolic responses of human brown adipose tissue to activation by cold and insulin. Cell Metab. *14*, 272–279.

Podgrabinska, S., Braun, P., Velasco, P., Kloos, B., Pepper, M.S., Jackson, D.G., and Skobe, M. (2002). Molecular characterization of lymphatic endothelial cells. Proc. Natl. Acad. Sci. *99*, 16069–16074.

Potente, M., and Mäkinen, T. (2017). Vascular heterogeneity and specialization in development and disease. Nat. Rev. Mol. Cell Biol. *18*, 477–494.

Qiu, Y., Nguyen, K.D., Odegaard, J.I., Cui, X., Tian, X., Locksley, R.M., Palmiter, R.D., and Chawla, A. (2014). Eosinophils and Type 2 Cytokine Signaling in Macrophages Orchestrate Development of Functional Beige Fat. Cell *157*, 1292–1308.

Renier, N., Wu, Z., Simon, D.J., Yang, J., Ariel, P., and Tessier-Lavigne, M. (2014). iDISCO: A Simple, Rapid Method to Immunolabel Large Tissue Samples for Volume Imaging. Cell *159*, 896–910.

Renier, N., Adams, E.L., Kirst, C., Wu, Z., Azevedo, R., Kohl, J., Autry, A.E., Kadiri, L., Umadevi Venkataraju, K., Zhou, Y., et al. (2016). Mapping of Brain Activity by Automated Volume Analysis of Immediate Early Genes. Cell *165*, 1789–1802.

Richardson, D.S., and Lichtman, J.W. (2015). Clarifying Tissue Clearing. Cell *162*, 246–257.

Roh, H.C., Tsai, L.T.Y., Shao, M., Tenen, D., Shen, Y., Kumari, M., Lyubetskaya, A., Jacobs, C., Dawes, B., Gupta, R.K., et al. (2018). Warming Induces Significant Reprogramming of Beige, but Not Brown, Adipocyte Cellular Identity. Cell Metab.

Rosen, E.D., and Spiegelman, B.M. (2014). What We Talk About When We Talk About Fat. Cell *156*, 20–44.

Rosenwald, M., Perdikari, A., Rülicke, T., and Wolfrum, C. (2013). Bi-directional interconversion of brite and white adipocytes. Nat. Cell Biol. *15*, 659–667.

Scherer, P.E., Williams, S., Fogliano, M., Baldini, G., and Lodish, H.F. (1995). A Novel Serum Protein Similar to C1q, Produced Exclusively in Adipocytes (*). J. Biol. Chem. *270*, 26746–26749.

Seale, P., Kajimura, S., Yang, W., Chin, S., Rohas, L.M., Uldry, M., Tavernier, G., Langin, D., and Spiegelman, B.M. (2007). Transcriptional Control of Brown Fat Determination by PRDM16. Cell Metab. *6*, 38–54.

Seale, P., Bjork, B., Yang, W., Kajimura, S., Chin, S., Kuang, S., Scimè, A., Devarakonda, S., Conroe, H.M., Erdjument-Bromage, H., et al. (2008). PRDM16 controls a brown fat/skeletal muscle switch. Nature *454*, 961–967.

Seale, P., Conroe, H.M., Estall, J., Kajimura, S., Frontini, A., Ishibashi, J., Cohen, P., Cinti, S., and Spiegelman, B.M. (2011). Prdm16 determines the thermogenic program of subcutaneous white adipose tissue in mice. J. Clin. Invest. *121*, 96–105.

Shao, M., Wang, Q.A., Song, A., Vishvanath, L., Busbuso, N.C., Scherer, P.E., and Gupta, R.K. (2019). Cellular Origins of Beige Fat Cells Revisited. Diabetes *68*, 1874–1885.

Sharp, L.Z., Shinoda, K., Ohno, H., Scheel, D.W., Tomoda, E., Ruiz, L., Hu, H., Wang, L., Pavlova, Z., Gilsanz, V., et al. (2012). Human BAT Possesses Molecular Signatures That Resemble Beige/Brite Cells. PLOS ONE *7*, e49452.

Shimizu, I., Aprahamian, T., Kikuchi, R., Shimizu, A., Papanicolaou, K.N., MacLauchlan, S., Maruyama, S., and Walsh, K. (2014). Vascular rarefaction mediates whitening of brown fat in obesity. J. Clin. Invest. *124*, 2099–2112.

Shinoda, K., Luijten, I.H.N., Hasegawa, Y., Hong, H., Sonne, S.B., Kim, M., Xue, R., Chondronikola, M., Cypess, A.M., Tseng, Y.-H., et al. (2015). Genetic and functional characterization of clonally derived adult human brown adipocytes. Nat. Med. *21*, 389–394.

Sun, K., Asterholm, I.W., Kusminski, C.M., Bueno, A.C., Wang, Z.V., Pollard, J.W., Brekken, R.A., and Scherer, P.E. (2012). Dichotomous effects of VEGF-A on adipose tissue dysfunction. Proc. Natl. Acad. Sci. *109*, 5874–5879.

Sun, K., Kusminski, C.M., Luby-Phelps, K., Spurgin, S.B., An, Y.A., Wang, Q.A., Holland, W.L., and Scherer, P.E. (2014). Brown adipose tissue derived VEGF-A modulates cold tolerance and energy expenditure. Mol. Metab. *3*, 474–483.

Virtanen, K.A., Lidell, M.E., Orava, J., Heglind, M., Westergren, R., Niemi, T., Taittonen, M., Laine, J., Savisto, N.-J., Enerbäck, S., et al. (2009). Functional Brown Adipose Tissue in Healthy Adults. N. Engl. J. Med. *360*, 1518–1525.

Wang, W., and Seale, P. (2016). Control of brown and beige fat development. Nat. Rev. Mol. Cell Biol. *17*, 691–702.

Wang, P., Loh, K.H., Wu, M., Morgan, D.A., Schneeberger, M., Yu, X., Chi, J., Kosse, C., Kim, D., Rahmouni, K., et al. (2020). A leptin–BDNF pathway regulating sympathetic innervation of adipose tissue. Nature *583*, 839–844.

Wang, Q.A., Tao, C., Gupta, R.K., and Scherer, P.E. (2013). Tracking adipogenesis during white adipose tissue development, expansion and regeneration. Nat. Med. *19*, 1338–1344.

Wu, J., Boström, P., Sparks, L.M., Ye, L., Choi, J.H., Giang, A.-H., Khandekar, M., Virtanen, K.A., Nuutila, P., Schaart, G., et al. (2012). Beige Adipocytes Are a Distinct Type of Thermogenic Fat Cell in Mouse and Human. Cell *150*, 366–376.

Wu, R., Yu, W., Fu, L., Li, F., Jing, J., Cui, X., Wang, S., Cao, Q., Xue, B., and Shi, H. (2020a). Postnatal leptin surge is critical for the transient induction of the developmental beige adipocytes in mice. Am. J. Physiol.-Endocrinol. Metab. *318*, E453–E461.

Wu, Y., Kinnebrew, M.A., Kutyavin, V.I., and Chawla, A. (2020b). Distinct signaling and transcriptional pathways regulate peri-weaning development and cold-induced recruitment of beige adipocytes. Proc. Natl. Acad. Sci. *117*, 6883–6889.

Xue, Y., Petrovic, N., Cao, R., Larsson, O., Lim, S., Chen, S., Feldmann, H.M., Liang, Z., Zhu, Z., Nedergaard, J., et al. (2009). Hypoxia-Independent Angiogenesis in Adipose Tissues during Cold Acclimation. Cell Metab. *9*, 99–109.

Ye, L., Wu, J., Cohen, P., Kazak, L., Khandekar, M.J., Jedrychowski, M.P., Zeng, X., Gygi, S.P., and Spiegelman, B.M. (2013). Fat cells directly sense temperature to activate thermogenesis. Proc. Natl. Acad. Sci. U. S. A. *110*, 12480–12485.

Yoneshiro, T., Aita, S., Matsushita, M., Kameya, T., Nakada, K., Kawai, Y., and Saito, M. (2011). Brown Adipose Tissue, Whole-Body Energy Expenditure, and Thermogenesis in Healthy Adult Men. Obesity *19*, 13–16.

Zeng, X., Ye, M., Resch, J.M., Jedrychowski, M.P., Hu, B., Lowell, B.B., Ginty, D.D., and Spiegelman, B.M. (2019). Innervation of thermogenic adipose tissue via a calsyntenin 3β–S100b axis. Nature *569*, 229–235.

Zhu, Y., Gao, Y., Tao, C., Shao, M., Zhao, S., Huang, W., Yao, T., Johnson, J.A., Liu, T., Cypess, A.M., et al. (2016). Connexin 43 Mediates White Adipose Tissue Beiging by Facilitating the Propagation of Sympathetic Neuronal Signals. Cell Metab. *24*, 420–433.